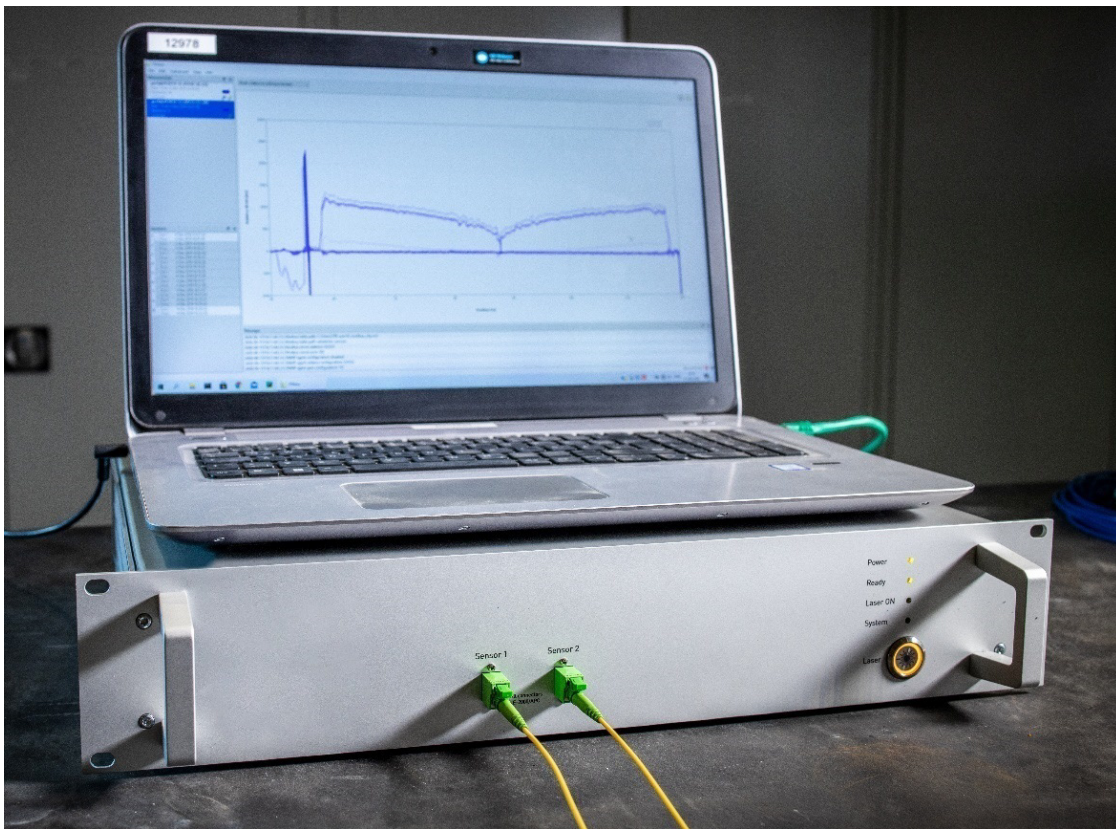




**MONITORING OF STRUCTURES AND ELEMENTS WITH FIBER OPTICS**  
**– HANDBOOK –**



Authors: Gust Van Lysebetten<sup>1</sup>, Petra Van Itterbeeck<sup>1</sup>, Noël Huybrechts<sup>1</sup>, Dimitrios Anastasopoulos<sup>2</sup>, Edwin Reynders<sup>2</sup>, Stijn François<sup>2</sup>

<sup>1</sup> Buildwise, Geotechnical, Structures and Concrete Technology Division

<sup>2</sup> KU Leuven, Faculty of Engineering Science, Structural Mechanics Subdivision

Version 1.0

Date: 22/03/2023

Contact: [gust.van.lysebetten@buildwise.be](mailto:gust.van.lysebetten@buildwise.be)

Check if you are reading the latest version of this handbook: <https://ovmonitoring.be/handbook/>

or scan the QR code:



---

## Table of Contents

Preface .....	6
1 Introduction .....	7
1.1 Optical fiber sensing.....	7
1.2 Terminology .....	11
1.3 Benefits of monitoring .....	14
2 Optical fiber sensing technologies.....	15
2.1 (Multi-)Point sensing.....	15
2.1.1 FBG .....	15
2.1.2 Other point sensing technologies .....	18
2.2 Distributed sensing .....	19
2.2.1 Light scattering (general) .....	19
2.2.2 Brillouin Scattering.....	20
2.2.3 Rayleigh Scattering.....	20
2.2.4 Raman Scattering .....	20
2.3 OFS technologies: summary.....	21
2.4 Temperature and strain compensation .....	26
2.5 Free and restrained deformations.....	26
3 Practical considerations.....	28
3.1 Tools and accessories.....	28
3.1.1 Fiber cleaning .....	28
3.1.2 Splicing .....	30
3.1.3 Fiber connectorisation .....	32
3.1.4 Fiber optic cables: patch cords and pigtailed .....	36
3.1.5 Fiber checkers and testers .....	38
3.2 Types of sensors and sensing cables.....	40
3.2.1 Strain transfer .....	40
3.2.2 (Multi-)point sensors.....	44
3.2.3 Distributed sensing cables .....	49
3.3 Sensor architecture.....	55
3.4 Sensor mounting.....	58
4 (Infra)structure monitoring applications .....	63
4.1 Application areas .....	63

---

4.1.1	Innovative systems.....	63
4.1.2	Proof testing.....	63
4.1.3	Long term monitoring of existing and new infrastructure .....	63
4.1.4	Quality control of invisible structural elements .....	64
4.2	Interpretation methods .....	64
4.3	Validation testing .....	66
4.3.1	Static behaviour of a concrete beam at different cracking degrees.....	66
4.3.2	Dynamic behaviour of a concrete beam at different cracking degrees.....	73
4.3.3	Concrete crack monitoring.....	76
4.3.4	Concrete corrosion monitoring.....	80
5	Monitoring cases.....	85
5.1	Innovative systems.....	85
5.1.1	Innovative grout anchor and piling system (Smet-F&C) .....	85
5.1.2	Reinforce research project.....	87
5.1.3	Innovative basement wall system (Prefaxis).....	91
5.2	Proof testing.....	94
5.2.1	Instrumented static pile load tests .....	94
5.2.2	Composite bridge, Bruges (Vlaamse Waterweg and MOW-EBS, Buildwise and KU Leuven) 95	
5.2.3	Oosterweel test pit, Antwerp (Lantis).....	99
5.3	Long term monitoring .....	100
5.3.1	Geotextile monitoring of a dike, Nieuwpoort (Maritime and Coastal Services, Flemish Government and Com&Sens) .....	100
5.3.2	Steel bowstring bridge KW51, Leuven (Infrabel and KU Leuven) .....	102
5.3.3	Steel railway bridge, Ronse (Infrabel, TUC Rail and KU Leuven).....	104
5.3.4	Vierendeel railway bridge Mechelen (TUC Rail, Infrabel and KU Leuven).....	107
5.3.5	Ground anchor monitoring, Streefkerk, NL (Rijkswaterstaat and Franki Foundations) ...	110
5.3.6	Leakage detection of earth dams, levees, water reservoirs, etc. with DTS.....	113
5.3.7	Monitoring pipelines for leakages and intrusions with DAS (Fluves) .....	114
5.3.8	Furnace insulation monitoring using DTS (Aperam).....	115
5.3.9	Turbine vibration frequency and soil characterization on offshore wind farms using DAS (Marlinks).....	116
5.3.10	Monitoring the burial depth of submarine power cables with DTS (Marlinks) .....	117

---

5.3.11	DTS fire detection system in the Tangent tunnel, Mechelen (Flanders Road and Traffic Agency)	118
5.4	Quality Control.....	119
5.4.1	Post-injections of grout anchors and foundation piles (Smet-F&C) .....	119
5.4.2	Temperature monitoring of diaphragm walls, Merksem (Lantis).....	121
5.4.3	Advanced thermal response tests (shallow geothermal energy) .....	123
6	References .....	125

---

## Preface

This state-of-the-art attempts to provide a guide for those who are new to the world of optical fiber technology. However, even for more experienced users, this document will contain useful information. The document has been prepared with the aim of lowering the threshold to apply or prescribe optical fiber sensing technology by summarizing and widely disseminating the current knowledge.

Besides an overview of the most common optical fiber sensing technologies, a very practical overview of sensors, sensor cables and accessories is given. Furthermore, this document also contains many tips on setting up a monitoring project, designing the sensor architecture and so on.

Finally, an extensive overview is offered of cases in which the technologies have already been deployed. This overview provides a clear picture of the great potential that optical fiber sensing technology has to offer.

This state-of-the-art has been elaborated in the framework of the COOCK project HBC.2019.2505 'Monitoring of structures and elements with fiber optics' funded by the Flemish Agency for Innovation (VLAIO).

# 1 Introduction

## 1.1 Optical fiber sensing

The optical fiber sensing technology has been improving continuously over the last decades. Nowadays, a wide range of optical fiber sensing techniques is available, offering many opportunities for sensing and monitoring of structures and elements. Typically, the optical fiber technique measures a change of strain (deformation) and/or temperature acting on the fiber. Based on this principle, several sensor types have been developed (dedicated strain or temperature sensors, but also sensors to measure pressure, vibration, inclination, chemical agents, moisture, etc.).

An optical fiber consists of a very thin glass (silica) core with a diameter of about  $9\ \mu\text{m}$  (single-mode fiber or SMF) to  $50$  or  $62.5\ \mu\text{m}$  (multimode fiber or MMF), which transmits light. This glass core is surrounded by a cladding with a diameter of about  $125\ \mu\text{m}$ , which confines the light to the core. The core and the cladding are protected by a coating and optionally additional strength members and jackets. These layers may consist of plastics, metallic sheathings, GFRP material, etc. and typically have diameters of less than a millimetre to several centimetres, depending on the application and required robustness.

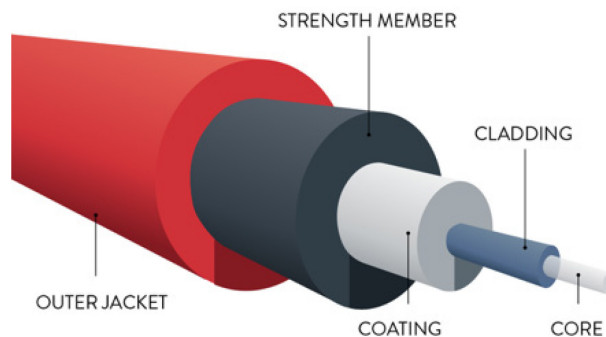


Figure 1. Typical fiber optic cable layout consisting of a glass core with a diameter of  $8$  to  $62.5\ \mu\text{m}$ , a cladding (diameter of  $125\ \mu\text{m}$ ), a coating and optional strength members and outer jackets. Image source: <https://www.ofsoptics.com/optical-fiber-coatings/>.

Fiber optic sensing offers several advantages in comparison to other measurement techniques, such as:

- Reliability: long term sensor stability, lifetime and robustness, in general no offset between disconnection and reconnection (as is often the case with other measuring techniques)
- Performance:
  - o High sensor density with very compact wiring. The fiber acts as sensor and data carrier. With distributed sensing technologies deformation/temperature/... can be monitored along the full length of the cable.
  - o High accuracy and precision possible (highly depends on the applied technology)
- Inert and robust:
  - o Applicable in harsh environments, immune to corrosion
  - o No electromagnetic (EM) or radio frequency (RF) interference
  - o Resistant to high voltage and not subject to short circuit

- Resistant to high temperatures
- Explosion proof
- Light weight and small size
- Geometric versatility, over long distances (depending on the applied technique) and multiplexing capabilities (i.e. the ability of connecting different sensors or sensor cables in series to a single cable/connector allowing for a very compact wiring, see e.g. Figure 2).

The compact wiring of fiber optic sensors is illustrated in Figure 2. On the left a traditional DAQ unit is shown with (a mess of) 96 temperature sensors (thermocouples) connected to it. It is obvious that wiring is much cleaner and compacter in the right picture where 3 sensor arrays with up to 30 FBG sensors each are connected to a FBG interrogator. Moreover, sensor identification is much easier and less prone to errors.



Figure 2. (left) 96 temperature sensors connected to a data acquisition (DAQ) system. (right) 3 sensor arrays connected to a FBG interrogator. Each array or each single cable could contain up to 30 sensors.

According to [1] the initial introduction of fiber optic sensing technologies already started in the last two decades of the past century. However, despite the clear advantages mentioned above, the uptake by the market was very slow. The direct competition with well know conventional sensor technologies and the high cost of suitable components have been identified as the root of the problem. However, this situation has fundamentally changed over the past 2 decades and the projections for the future are very optimistic as illustrated in Figure 3.

Another important factor is the continuously improving performances of optical fiber sensors. According to [2], this was immediately picked up and tapped into by the worldwide scientific community, leading to an increasing number of research articles (e.g. Figure 4a). Additionally, a market survey report conducted by the Photonic Sensor Consortium demonstrates that the increased popularity of optical fiber sensors goes hand in hand with the monitored and predicted growth of the whole optical fiber sensors technological market (Figures 4a and 5).

Monitoring of existing structures in order to extend their service life is also a very topical theme, as can be seen in the evolution of the number of publications on structural health monitoring (see Figure 4b). In this context, fiber optics can also be a very helpful tool to allow for more targeted inspections and prevent



greater damage from occurring, allowing to safely keep critical infrastructure operational for longer should the need arise.

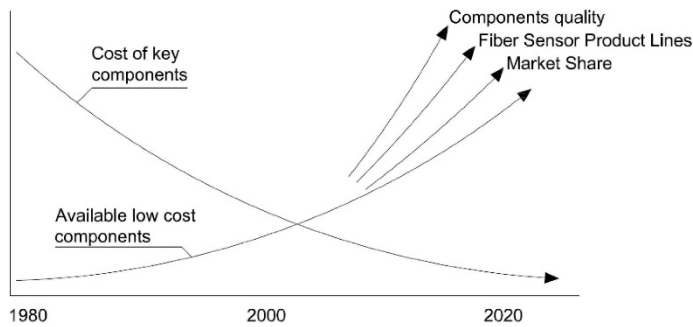


Figure 3. Trends for fiber optic sensors. Source: [1], image adapted from Udd and Spillman (2011).

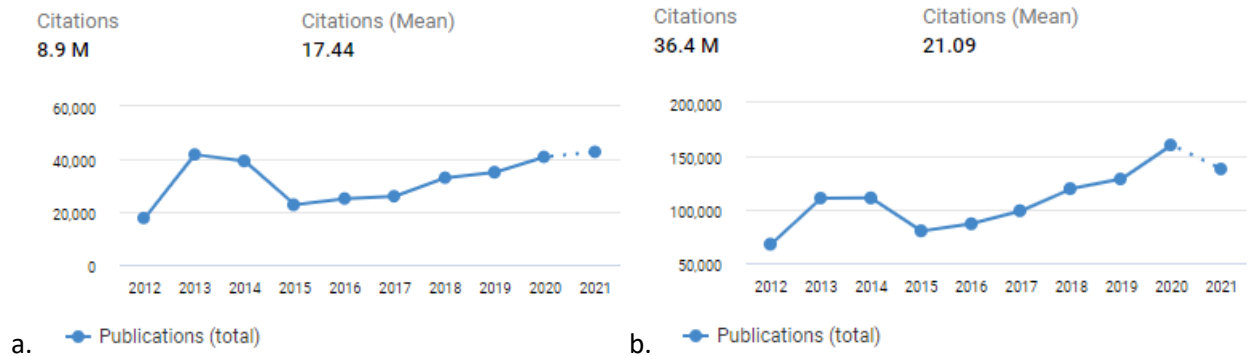


Figure 4. Evolution of the number of publications about (a) optical fiber sensing and (b) structural health monitoring, according to the data from <https://app.dimensions.ai/discover/publication> (accessed on 06/12/2021).

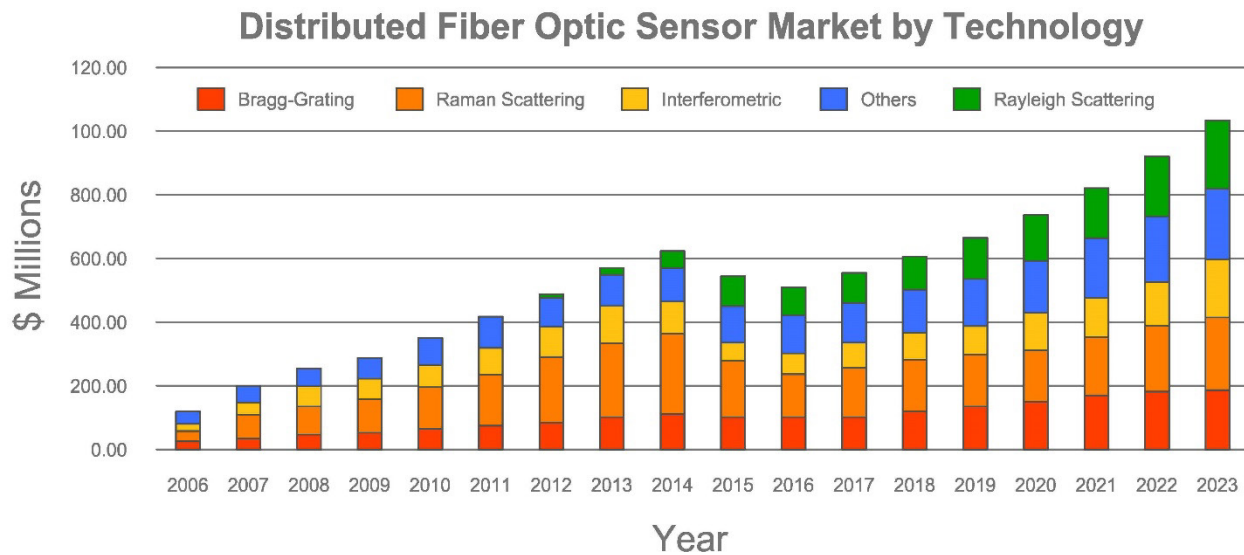


Figure 5. Growth of optical fiber sensors technological market based on a market survey report conducted by the Photonic Sensor Consortium. Source: [4].

A large variety of optical fiber sensing technologies is currently available on the market. One of the aims of this document is to present a concise but clear overview of the currently most commonly used technologies. The selection of the appropriate technique for a specific application is not always straightforward, as each technology has its own pros and cons in terms of cost of the data acquisition system and the sensor cables, accuracy, spatial resolution and sensor density, maximum frequency, etc.

Figure 6 shows a schematic overview of the available fiber optic sensing technologies, classified by the sensor type. Figure 7 presents a similar but simplified schematic overview, classified by point or multipoint sensors and distributed sensors. With point or multipoint sensors a measurement is carried out in (a) discrete point(s) along the length of the fiber, while for distributed sensors the whole cable acts as a sensing element (see Section 2 for more background). The most common multipoint sensor technology is Fiber Bragg Grating (FBG). Other point sensing technologies are based on e.g. micro-bending (Osmos) and low-coherence interferometry (SOFO). The distributed technologies are based on three types of back-scattering of light (Brillouin scattering, Rayleigh scattering and Raman scattering) [5].

Some background about the measurement principles of the different technologies is presented in paragraph 2 “Optical fiber sensing technologies”. The selection of the appropriate (D)FOS technology always involves a trade-off between the sensing type, range, spatial resolution and precision, which must be suitably adjusted depending on the requirements of the actual civil engineering application [6].

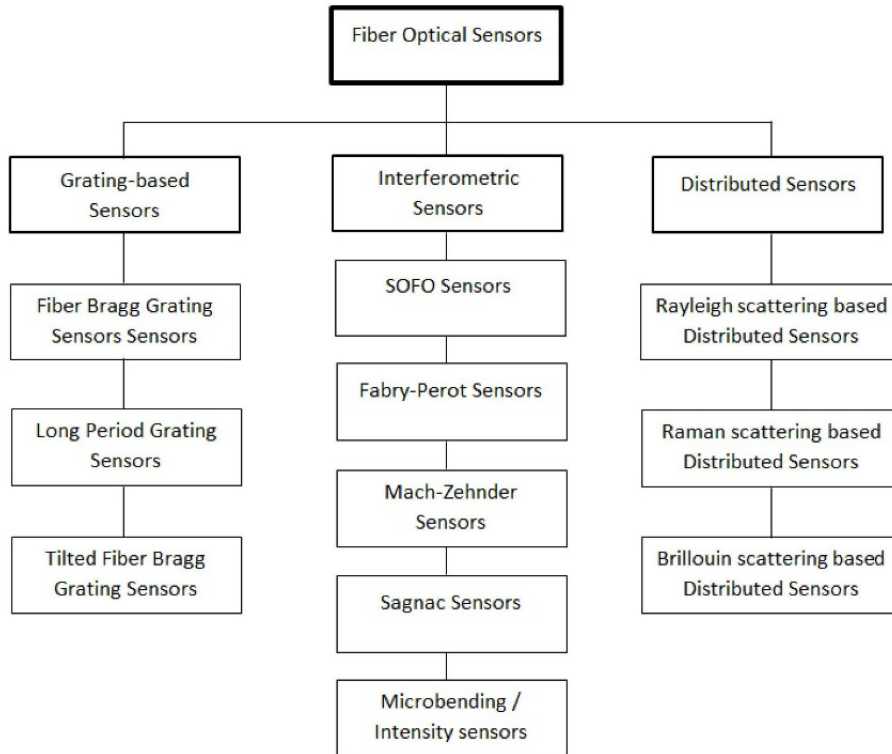


Figure 6. Schematic overview of fiber optic sensing technologies. Source: [1].

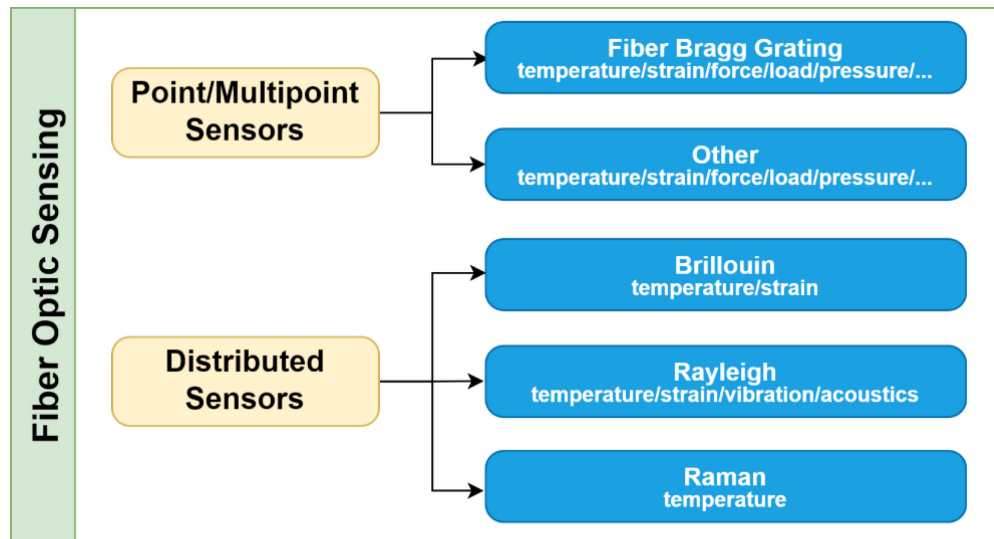


Figure 7. Simplified schematic overview of most commonly used fiber optic sensing technologies.

## 1.2 Terminology

One should keep in mind three key measurement parameters when comparing measurement techniques and their performance [7]:

- 
- *Accuracy*: It qualitatively expresses the closeness of the measured value to the true or ideal ('master') value of the measurand. Accuracy represents the qualitative difference between the measured result and the true value and is affected by both bias (quantitative difference between the average of the measurements and its true value) and precision.
  - *Precision*: It describes how repeatable a measurement result is. Precision is expressed by the estimated standard deviation of a specified series of measurements. (Sometimes precision is expressed as a multiple of the estimated standard deviation, e. g.  $2\sigma$ ). The smaller the dispersion of the measured values, the better the precision; precise measurement results need not to be necessarily accurate (e.g. due to bias). Therefore, a result of a single measurement should be interpreted as drawn from an ensemble with the measured standard deviation.
  - *Resolution*: It represents the smallest change in the measurand, meaningfully detectable by the measurement system. The resolution is limited by either the instrument readout or precision, whichever is bigger.

The difference between these parameters is illustrated in Figure 8.

Note that in sensing applications, the main performance parameters depend on the application and the time scale of the measurement [8]. For static, long term, low frequency applications (e.g. temperature/pressure measurements), the stability and long term drift of the sensor is an important parameter. For dynamic, short term, high frequency applications (e.g. acceleration/vibration measurements), the noise floor of the measurements which is correlated to the repeatability, resolution (precision/standard deviation) is an important parameter.

Furthermore, '*spatial resolution*' and '*spatial accuracy*' are 2 other important parameters, expressing the performance of distributed sensing systems and the ability to reliably detect physical strain and temperature events (illustrated in Figure 9) [7, 9]:

- *Spatial resolution*: the spatial resolution is specified for a fiber by the minimum distance between two step transitions of the fiber strain / temperature condition. It is the minimum distance over which the system is able to indicate the value of the measurand within the specified uncertainty.
- *Spatial accuracy*: the distance between two measurement points in the resulting measurement curve of the strain / temperature profile along the fiber.

A higher spatial accuracy provides more detailed information on the exact position and shape of physical strain or temperature events along the fiber. The spatial accuracy can be increased by changing the sampling rate of the instrument's digitizer, or by post-processing operations like interpolation schemes. A higher number of data points within the length of the optical pulse does not provide independent strain or temperature readings. They do, however, increase the accuracy of the spatial allocation of physical events (like the edge of a strain transition) in the measurement curve (as illustrated in Figure 9).

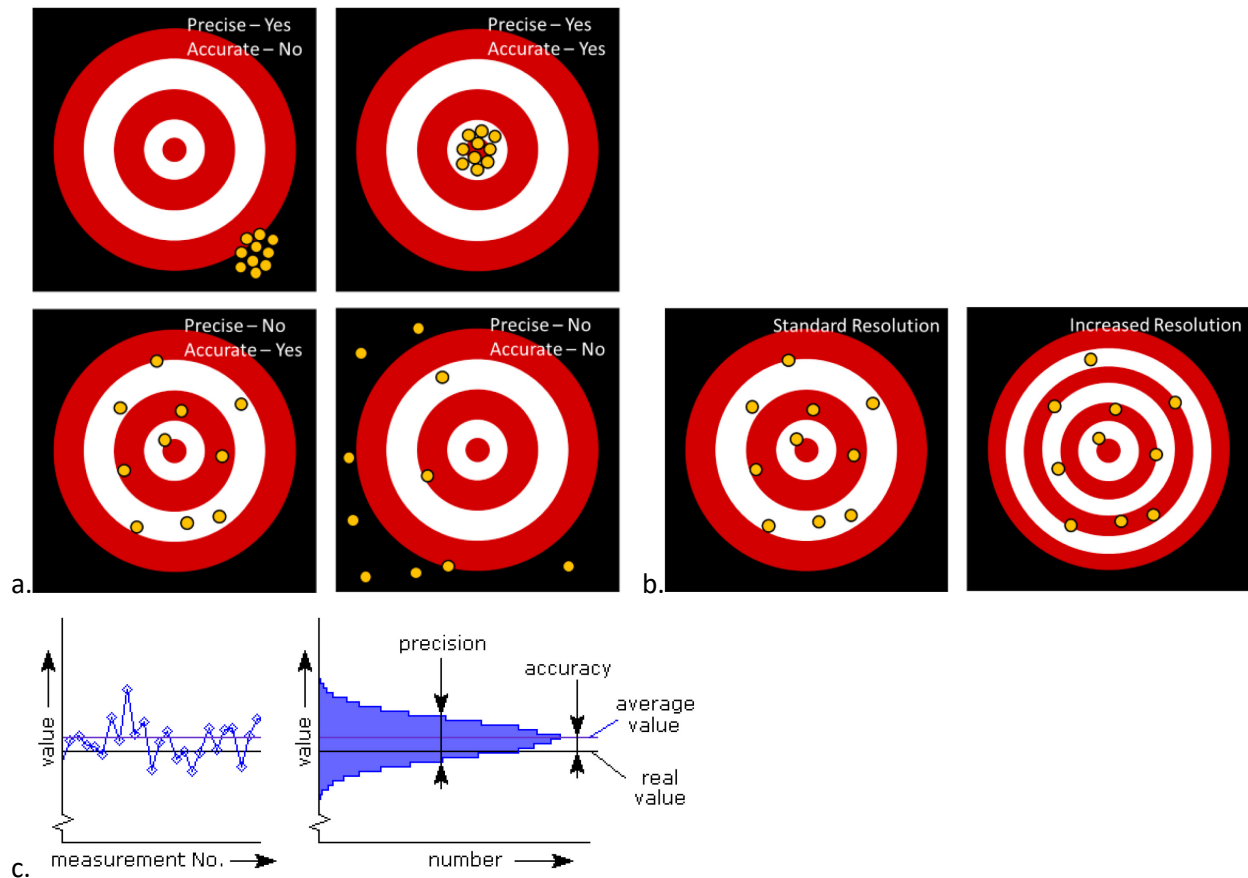


Figure 8. (a) Precision versus accuracy. (b) Lower and higher resolution. Image source : <https://control.com/technical-articles/what-is-the-difference-between-accuracy-precision-and-resolution/>. (c) Alternative visualization of precision versus accuracy. Image source : <https://meettechnik.info/measurement/accuracy.html>.

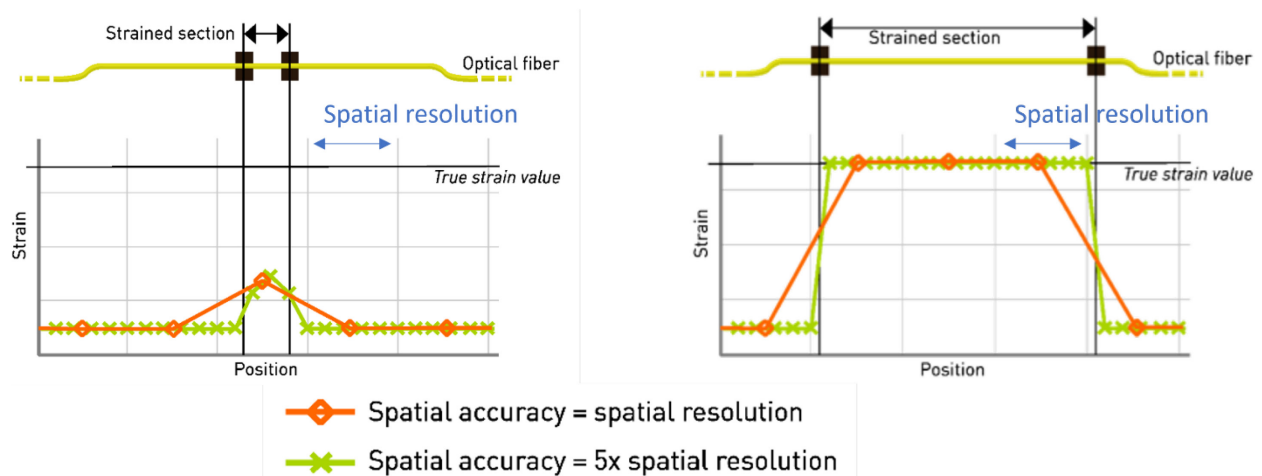


Figure 9. Illustration of the terms 'spatial resolution' and 'spatial accuracy'. In the left example, the length of the strained section is half as long as the spatial resolution. The strain of the fiber is not measured correctly. A higher spatial accuracy does not increase the reliability of measuring short physical events. In the right example, the length of the strained section is three times the spatial resolution. The strain of the fiber is measured correctly. A higher spatial accuracy provides more precise reallocation of the position of the steps. Figures based on [9].

### 1.3 Benefits of monitoring

New and existing structures (amongst others wind turbines, quay walls, dikes, bridges and tunnels) are increasingly being monitored over a short or longer period of time. The objectives might be at least one of the following purposes:

- Assessment of the long-term performance of the structure or element (in terms of stability as well as durability).
- Extension of the lifetime of the structure, by continuous condition monitoring.
- Optimization of the inspection and maintenance strategy, resulting in a reduction of the inspection, maintenance and operational costs.
- Establishment of a risk management or early warning system to reduce/prevent hazards.
- Verification of the structural design and optimization of future design challenges by refining design models. The measurements might take place during the construction phase and/or after the commissioning of the structure (e.g. during excavation and after commissioning of a quay wall).

However, extensive monitoring during preliminary test campaigns is also a valuable and powerful tool (e.g. real scale load tests). In addition to this, monitoring offers many possibilities in the area of quality control of the execution during construction or manufacturing. This includes integrity testing but also evaluating (innovative) implementation techniques.

Most of these topics are discussed and illustrated in more detail in Sections 4 (Infra)structure monitoring applications and 5 (Monitoring cases).

## 2 Optical fiber sensing technologies

### 2.1 (Multi-)Point sensing

#### 2.1.1 FBG

Fiber Bragg Gratings (FBG) are probably the most commonly used multipoint sensing technology. An FBG is a spatially limited periodic modification of the refractive index in the core of the optical fiber [5]. This inscription is done by using a laser source. The typical length of an FBG sensor is about 1 to 10 mm.

When light is incident upon an FBG, a portion of the incident light intensity  $P$  will be reflected at a specific wavelength, corresponding to FBG grating properties and the period  $L$  of the refractive index variation (Figure 10a). If a relative strain or temperature change is applied to the FBG the periodicity of the refractive index changes which results in a change of the reflected wavelength (Figure 10b). As the wavelength change is proportional to the change of strain and temperature acting on the FBG, FBGs can be used as strain and temperature sensors.

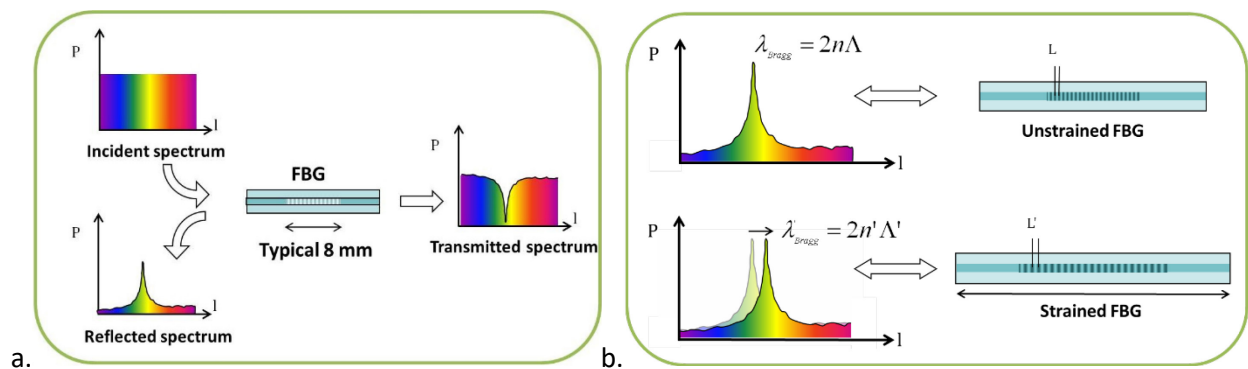


Figure 10. (a) Incident light is reflected at a specific wavelength, depending on the FBG properties. Source: [www.fbgs.com](http://www.fbgs.com). (b) The reflected wavelength depends on strain and temperature acting on the FBG. Source: [www.fbgs.com](http://www.fbgs.com).

Apart from the high accuracy, the high acquisition rates ( $> 1$  kHz) and the fact that only one fiber end is required ('single-ended'), one of the major advantages of the FBG technology are the multiplexing capabilities in the wavelength domain, also called wavelength division multiplexing (WDM). Multiple FBGs can be inscribed on one single fiber at different reflecting wavelengths (i.e. every FBG is identified through its own Bragg wavelength). The spatial spacing between each FBG sensor may vary between several centimetres to meters. The reflecting wavelength of each sensor and the wavelength spacing should be chosen properly in order to avoid overlapping or shifting of 2 adjacent peaks during installation, operation or lifetime of the element or structure. This wavelength spacing and some characteristics of the interrogator (like wavelength range) mainly define the maximum number of FBGs that can be multiplexed (typically about 20 to 30). Figure 11 shows a typical reflected spectrum of an array with 15 multiplexed FBGs. The wavelength range of the interrogator is 1510-1590 nm. The wavelength spacing of the FBGs is about 5 nm.

FBG interrogators are commercially available via a wide range of companies and with a large variety of properties. The number of available channels varies between typically 1 to 16. Every channel can be connected to a multiplexed FBG array.

More recent developments allow a much higher FBG sensor density on the fiber. By using a modified interrogation scheme, laser source and an arrival time-dependent detection approach more than 1000 sensors can be put on one fiber [10]. This evolution is very promising but still under development.

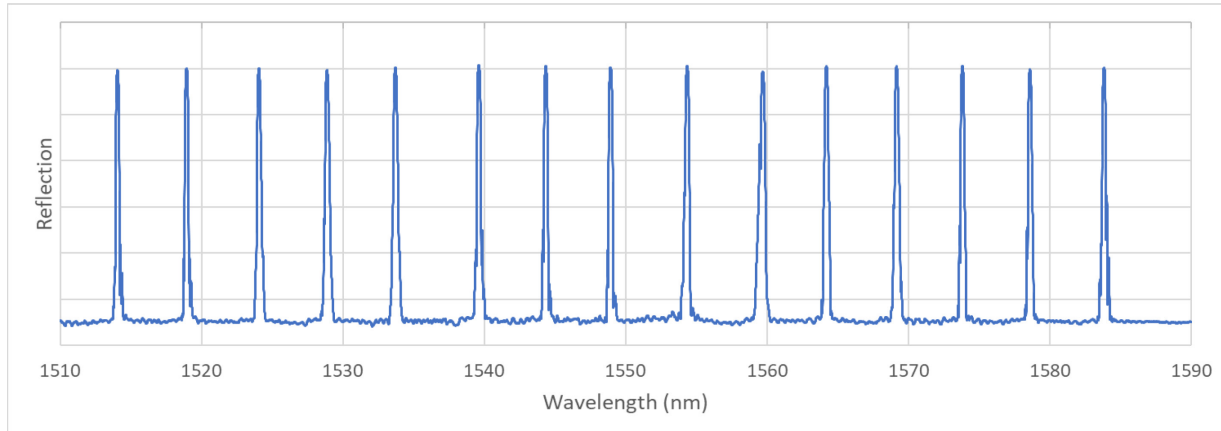


Figure 11. Typical reflected spectrum of an FBG array with 15 multiplexed sensors.

Fiber Bragg Gratings are made by exposing the core of a single-mode fiber to a periodic pattern of laser light. This exposure produces a permanent increase in the refractive index of the fiber core, creating a fixed index modulation according to the exposure pattern. Different grating inscription techniques exist, each with its own strengths and disadvantages [8]:

1. FBG inscribed with a phase mask (Strip-Recoat FBG, by stripping and recoating the fiber)
2. FBG inscribed during fiber drawing process (Draw Tower Grating or DTG)
3. Femto-Second inscribed FBG through the fiber coating (fs-FBG)

The stripping and recoating process (1) often results in damage in the fiber, causing both lifetime and maximum strain limitations. Additionally, the recoating process may result in a different and non-uniform coating at the location of the grating, causing different sensing characteristics.

Many of these limitations are overcome with the DTG technique (2), which enables the inscription of gratings during the fiber drawing process, even before the coating is applied to the fiber. DTG arrays are characterized by a high tensile strength, but also by lower reflectivity levels (because of the limited time of exposure during the draw process). Moreover, their core diameter might deviate from the standard telecom fibers and the attenuation losses (due to absorption and scattering) are typically higher. These properties should be taken into account during the sensor architecture of a specific project and the DAQ unit selection (see also Section 3.3 on 'Sensor architecture').

More recently, the femtosecond inscription technique (3) allowed to inscribe the FBG through the coating. This can be achieved either by using point-by-point, line-by-line or phase mask inscription techniques. One specific advantage of the femtosecond written gratings is the ability to form the FBG in various fiber types and dopant levels, even pure silica fibers, which enable FBGs to operate at high temperature and



chemically harsh conditions such as high hydrogen levels as encountered in downhole situations in oil and energy applications.

The overall system performance of a FBG sensing system does not only depend on the interrogator, but also on the specifications of the Fiber Bragg Gratings [8]. A Fiber Bragg Grating is characterized by amongst others the grating length, the FBG full width at half maximum (FWHM), the side lobe suppression ratio (SLSR), the reflectivity, the coating type, the uniformity, the polarization dependent frequency shift (PDFS) and the FBG shape distortion and asymmetry. Some of these parameters are illustrated in Figure 12 and explained below: [8]

- **Bragg wavelength** (nominal central wavelength,  $\lambda_c$ ), defined as the wavelength of highest reflection.
- **Full width at half maximum (FWHM)**, defined by the FBG width at 50% peak amplitude (-3dB). Especially when performing high resolution sensing applications with tuneable laser interrogators, it is highly desired to have the reflection spectra as sharp as possible with the smallest FWHM.
- **Side lobe suppression ratio (SLSR)**, defined as the ratio between the FBG main lobe peak and the highest secondary neighbour peak. Ideally, the SLSR level should be as high as possible to ensure only a single reflection peak is present.
- **Reflectivity**, defined as the maximum percentage of power reflected by the FBG peak. While it is desirable in most applications to have high reflection peaks, new generation interrogators can handle tracking with very low reflections.
- **Asymmetry ratio** ( $A_s = A_{s,50\%}/A_{s,10\%}$ ), as illustrated in Figure 12. Ideally, the reflection spectra should be fully symmetric and the  $A_s$  factor should be 1.
- **Polarization dependent frequency shift (PDFS)**, defined as the maximum observed peak to peak change in recorded Bragg wavelength due to polarization change which can be emulated by using an external manual or automatic polarization controller placed in the FBG path. Ideally, FBG peak recorded should be independent of the polarization and the PDFS should be minimal to ensure the sensing system is immune to polarization changes in the standard telecommunication fibers due to temperature change and movement of the fiber.

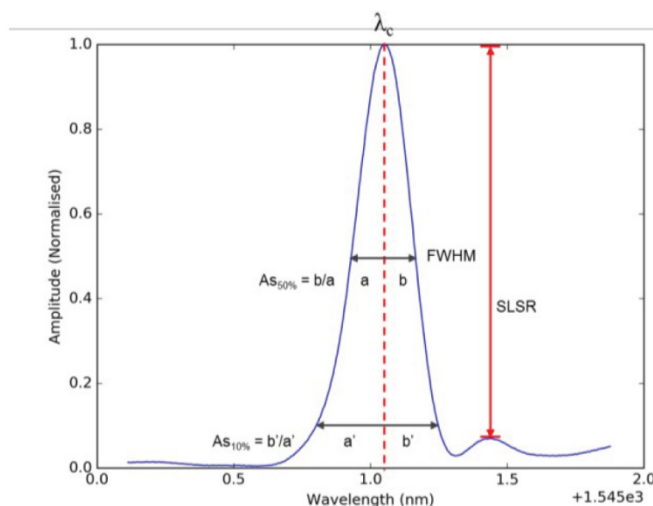


Figure 12. Typical FBG reflected spectrum (linear normalised amplitude) with the main parameters (central wavelength  $\lambda_c$ , asymmetry ratio  $A_s$ , FWHM, SLSR). Source: [8].

### 2.1.2 Other point sensing technologies

Other point sensing technologies are among others Fabry-Perot interferometers, low-coherence interferometry (SOFO system, or the French acronym “Surveillance d'Ouvrages par Fibres Optiques”) and microbending displacement sensors [11]. In the next paragraphs, these technologies are discussed very briefly.

#### 2.1.2.1 Fabry-Perot interferometers

Extrinsic Fabry-Perot Interferometers are constituted by a capillary silica tube containing two cleaved optical fibers facing each other, but leaving an air gap of a few microns or tens of microns between them. When light is launched into one of the fibers, a back reflected interference signal is obtained. This is due to the reflection of the incoming light on the glass-to-air and on air-to-glass interfaces. This interference can be demodulated using coherent or low-coherence techniques to reconstruct the changes in the fiber spacing. Since the two fibers are attached to the capillary tube near its two extremities (with a typical spacing of 10 mm), the gap change will correspond to the average strain variation between the two attachment points.

Worldwide, there are several applications of this system. In Europe, its use has been very limited. However, the Federal Institute for Materials Research and Testing of Germany (BAM) has applied it in several monitoring cases [11].

#### 2.1.2.2 SOFO displacement sensors

The SOFO technology is based on low-coherence interferometry. It was developed at the Swiss Federal Institute of Technology in Lausanne (EPFL) and is sold by Smartec (Switzerland) [11]. The resolution of the system is about 2 micrometre/meter. The deformation measurement base can vary from 0.25 m up to 20 m. The system is characterized by a long term stability (precision of 0.2% of the measured deformation) and has been applied in a wide range of monitoring applications.

#### 2.1.2.3 Microbending displacement sensors

For the microbending principle, an optical fiber is twisted with one or more other fibers or with metallic wires along its sensing length [11]. When this fiber optic twisted pair is elongated, the fibers will induce bending in one-another and cause part of the light to escape from the fiber. By measuring the intensity of the transmitted light, it is possible to reconstruct the deformation undergone by the structure or element on which the sensor is mounted.

OSMOS offers displacement sensors based on this technology and has used them on a wide range of structural health monitoring applications (bridges, tunnels, buildings, quay walls, etc.). An interesting evolution is the wireless solution, for which each sensor module sends its data through a wireless connection to a central gateway. Recently, a weigh-in-motion system has been developed for bridges and roads based on the measurement principle. The accuracy is about 2 micrometre/metre. The typical length of the measurement base is about 1 to 2 m.

## 2.2 Distributed sensing

### 2.2.1 Light scattering (general)

[5] give a very clear and accessible explanation of the light scattering phenomena behind distributed sensing. A large number of scientific papers also present a clear overview of the theoretical phenomena behind distributed sensing (and applications of structural health monitoring) [1, 2, 12, 13].

When an incident light signal transmits through the fiber core, a small disruption in the environment will affect the fiber length, diameter and refractive index and cause a change in the back-scatter of the light signal. The changes in the characteristics of back-scattered light are the key to understand what causes the environmental changes (e.g., temperature, strain, etc.). The changes in intensity, phase and frequency of the back-scattered signal are interpreted to determine the physical parameters' location and amplitude along the length of the fiber. By detecting changes in the amplitude, frequency, and phase of light scattered along the fiber, one can create a distributed fiber sensor for measuring local temperature, strain, vibration and pressure over lengths of 1 m to 100 km and more. Such measurements can be made in the time or frequency domain to resolve location information. The continuous back-scattered trace over time, where each time point corresponds to a particular location along the fiber, is converted into distance based on the speed of light in the fiber and the length of the fiber.

Back-scattered light in a fiber optic cable has three components: Rayleigh, Stokes, and anti-Stokes. The Stokes and anti-Stokes components consist of Brillouin and Raman back-scattered light (Figure 13). Therefore, the back-scattered light spectrum consists of three types of scattering: Rayleigh, Brillouin, and Raman. The Rayleigh band has the highest intensity, followed by the Brillouin groups and then the Raman bands.

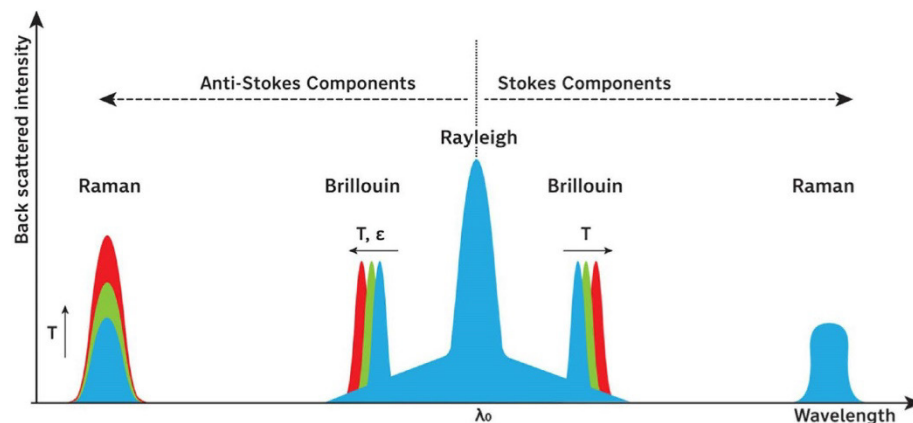


Figure 13. Rayleigh, Raman and Brillouin peaks in the back-scattered light spectrum.  $T$  represents temperature and  $\epsilon$  is strain. Source: [5].

Apart from the component of the backscattered light that is used (Brillouin, Raman, Rayleigh), DFOS systems can also be categorized by the way of finding the location of vibration, strain or temperature [14]:

- Optical Time Domain Reflectometry (OTDR): a pumping pulse light of known width is transmitted and measures the reflected energy and time of flight.

- Optical Time Domain Analysis (OTDA): pump and probe lights are transmitted from both ends of the fiber and analyse the power difference related to time delay.
- Optical Frequency Domain Reflectometry (OFDR): a continuous laser source is swept in frequency domain over a period of time, where the spectrum is spatially related to amplitude and phase of the scattered light.

### 2.2.2 Brillouin Scattering

Brillouin scattering involves interactions among the incident wave, scattered wave and phonons, and a minimum frequency shift of about 11 GHz at 1530 nm [5]. This frequency shift for a specific incident light signal depends only on the fiber acoustic velocity and refractive index. These parameters are determined by the fiber core composition and environmental variables. The Brillouin frequency shift, which is proportional to the medium's acoustic velocity, demonstrates a linear relationship with temperature and strain. Therefore, the frequency shift observed in most Brillouin scattered light-based distributed sensors measures the local Brillouin shift due to the change in environmental conditions. The amplitude and the wavelength of Brillouin scattered light are strain and temperature-dependent. When a constant incident light wavelength source is used, the Brillouin scattering wavelength changes with temperature and strain. The Brillouin signals are approximately 15-20 dB weaker than the Rayleigh signals, but they are an order of magnitude stronger than Raman signals. This enables Brillouin-based sensors to have a higher signal-to-noise ratio (SNR), improving the sensor spatial resolution and range.

### 2.2.3 Rayleigh Scattering

Rayleigh scattering is an elastic process that results from randomly occurring inhomogeneities in the refractive index of the fiber core [5]. Since this scattering is elastic, the frequency of Rayleigh scattering is equivalent to that of the incident light, but has a time delay, which is useful for spatially distributed sensing along the fiber length. By comparing the measurements with the reference state, and via cross-correlation, the frequency shift induced by the strain and/or temperature changes can be calculated [14].

The Distributed Acoustic Sensing (DAS) approach that detects acoustic waves along the fiber length is also based on Rayleigh scattering (OFDR or phase-OTDR).

### 2.2.4 Raman Scattering

Raman back-scattering inside the fiber core occurs due to the back-scattering of an incident photon by a molecule [5]. The back-scattered photon will instantaneously undergo two-state transitions by either producing or absorbing another photon. Raman scattering, with one temperature dependent component (intensity of the anti-Stokes band) and one temperature-independent component (the Stokes band), derives the local temperature from the ratio of the anti-Stokes and Stokes light intensities. It is primarily used in Distributed Temperature Sensing (DTS) systems to determine temperature changes along the fiber.

Theoretical background: conclusion according to Fenta, et al. (2021)

Generally, there are certain advantages using one type of back-scattered-based sensor over another depending on the detected physical parameters (Figure 13).

Raman peaks remain unaffected by strain changes. The anti-Stokes component is temperature-dependent, while the Stokes component is virtually unaffected by temperature changes. Using the Raman peaks, one can determine the temperature by analysing the ratios of the amplitudes of the anti-Stokes and Stokes components utilizing a detector. Raman components are ideal for obtaining information regarding the temperature distribution along the optical fiber.

In the case of Brillouin peaks, temperature causes a change in wavelength of both the Stokes and anti-Stokes components. The Brillouin peaks spread outward from the centre with an increase in temperature, while the Stokes components are unaffected by strain changes. This information allows distinct temperature and strain measurements.

The Rayleigh and Brillouin scatterings have the potential to achieve simultaneous detection of temperature and acoustic parameters. A combination of Rayleigh and Brillouin scattering can be used for simultaneous measurements of vibration and temperature in single-mode fibers with a 1550 nm light source.

### 2.3 OFS technologies: summary

Numerous distributed optical fiber sensor technologies have been developed based on the light scattering phenomena occurring in fibers described in Section 2.2. The most common technologies are listed below and their key properties are summarized in Table 1:

- **Brillouin-scattering-based sensors**
  - o Optical Time-Domain Reflectometry (BOTDR)
  - o Optical Frequency-Domain Reflectometry (BOFDR)
  - o Optical Time-Domain Analysis (BOTDA)
  - o Optical Frequency-Domain Analysis (BOFDA)
- **Raman-scattering-based sensors**
  - o Optical Time-Domain Reflectometry (OTDR)
- **Rayleigh-scattering-based sensors**
  - o Optical Frequency-Domain Reflectometry (OFDR)
  - o Optical Backscattered Reflectometer (OBR)
  - o Tuneable Wavelength Coherent Optical Time Domain Reflectometry (TW-COTDR)
  - o Optical Time-Domain Reflectometry (OTDR) → Distributed Acoustic Sensing (DAS)
  - o Phase Optical Time-Domain Reflectometry ( $\phi$ -OTDR) → Distributed Acoustic Sensing (DAS)

As mentioned before, the selection of the appropriate (Distributed) Fiber Optic Sensing technology always involves a trade-off between the sensing type, range, spatial resolution and strain sensing precision, which must be suitably adjusted depending on the requirements of the actual application. [6] Furthermore, the cost and properties of the DAQ unit and sensors or sensing cables are also important parameters that will be taken into account when deciding on which (D)FOS technology to use.

---

When the number of sensing points is rather limited or the application requires a very high spatial accuracy, a high measurement precision and/or a high measurement rate, the **FBG technology** and single-point sensing techniques are probably the most appropriate solution.

However, for limited sensing ranges (less than 70 m), the **Rayleigh scattering-based OFDR technology** offers very interesting distributed sensing capabilities in terms of resolution, accuracy, spatial resolution/accuracy and high frequency data-acquisition. The principal drawbacks are however the high cost of the data-acquisition (DAQ) unit (> 100 000 EUR) and the limited sensing range (max. 70 m). For longer sensing ranges, the **Rayleigh scattering-based TW-COTDR technology** reaches even better strain sensing resolution, but this has an impact on the spatial resolution and even more important on the cost of the DAQ unit.

For long range (> 100 m) strain or temperature monitoring, **Brillouin scattering-based sensors** offer an interesting more cost-effective alternative. The performance of the **BOTDR** and **BOFDR** techniques is lower than the **BOTDA** and **BOFDA** technologies, especially in terms of measurement precision and spatial resolution. However, the cost of the DAQ unit is generally lower. For a lot of applications where larger deformations are expected or where a measurement accuracy of more than 10 micrometre/metre is acceptable (e.g. dike monitoring, etc.), these technologies are very suited. On the other hand, if the application requires a higher measurement performance, **BOTDA** and **BOFDA** are probably more convenient. Note that **BOTDA** and **BOFDA** techniques require both cable ends to perform a measurement (double-ended), while **BOTDR** and **BOFDR** are single-ended measurement techniques. **Brillouin scattering-based sensor technology** does not allow for dynamic measurements. A measurement typically takes several minutes.

When only interested in temperature measurements, the **Raman technology** might be the best solution. As Raman scattering is not affected by strain changes, it results in the most accurate distributed temperature readings. Other distributed sensing technologies that are susceptible to both strain and temperature, use special 'temperature sensing cables' with a loose fiber in a tube. However, (limited) strain transfer to this fiber is never excluded.

When it comes to vibration, sound or temperature variation monitoring, **distributed fiber acoustic sensing (DAS)** technology is a very powerful tool because of its high temporal and spatial resolution, large sensing distance (> 10 km), dynamic quantitative measurement, etc. [15] The technology shows good performance for long perimeter monitoring aiming to detect potential threats or intruders on the ground or vibration in general [16]. The high sensitivity with sensing ranges in the order of tens of kilometres and spatial resolutions in the meter range, provides the possibility of detecting low energy activities, even such as people walking over a buried fiber. Fields of application can be found in perimeter security, railway transportation, pipeline and cable safety monitoring, nature hazard detection, geophysical prospecting, etc.

#### Basic considerations when selecting a FOS system

Before selecting a FOS system, one should clearly define the purpose of the monitoring campaign and what parameters and phenomena must be monitored. The ‘ultimate’ FOS system and sensor type not only depend on the material characteristics, but also on what phenomena should be captured by the system. E.g., a heterogeneous material like reinforced concrete require other sensor types than homogeneous material like steel, the monitoring of local cracks demand other FOS systems and sensor types than when the global behaviour of a heterogeneous material is monitored. For local event monitoring, the spatial resolution and spatial accuracy of the FOS system should be low enough (definitions see Section 1.2 “Terminology”). The required measurement frequency should also be considered.

For instance, a local FBG will measure very little strain change or even strain relief when it is located next to a wide crack. When this FBG is installed with a larger measurement base (see also Section 3.4 “Sensor mounting” and Figure 48), this crack might be captured by the sensor. DFOS systems offer more potential to capture local cracks, provided that the appropriate strain sensing cable type and DFOS system has been selected (i.e., a cable with the appropriate strain transfer properties and a DFOS system with an appropriate spatial resolution and spatial accuracy). The selection of FOS system(s) and sensor type(s) is further illustrated and discussed in Section 3.2 “Types of sensors and sensing cables”, Section 4.3 “Validation testing” and Section 5 “Monitoring cases”.

Table 1. Overview of the most common optical fiber technologies (based on own experience, completed with data from [1], [2], [6] and [15]). Measurement performance often depends on cable length, measurement time, etc. SMF single mode fiber, MMF = multimode fiber.

	Optical fiber technique	Strain [ $\mu\text{str}$ ]	Temperature [ $^{\circ}\text{C}$ ]	Measurement type	Cost	
		[accuracy]			DAQ	Sensor
Point sensing and/or Multi-point Sensing	FBG	Yes < 1	Yes 0.1 $^{\circ}\text{C}$	Multi-point (SMF) Single ended Spatial res.: >2mm (grating length) Range: several kilometres Max. frequency: >1kHz	-/+	+
	Other (Osmos, SOFO, ...)	Yes 1	?	Single point Single-ended Large number of channels on DAQ Wireless solutions as well (Osmos) Range: several kilometres Up to 100Hz (Osmos)	-	-/+
Distributed Sensing	Brillouin Scattering (BOTDR/BOFDR)	Yes > 20	Yes > 1.0	Single ended (SMF) Spatial res.: >1.0m Range: up to 100km Typ. meas. duration: 3-60min.	+/-+	-
	Brillouin Scattering (BOTDA/BOFDA)	Yes > 2	Yes 0.1-1.0	Double ended (SMF) Spatial res.: 0.2-1.0m Range: up to 80km Typ. meas. duration: 3-60min.	+/-+	-
	Raman Scattering (OTDR)	No /	Yes 0.1	Single and double ended (MMF) Spatial res.: 0.01-1.0m (typical 0.5m) Range: up to 10-15km Typ. meas. duration: about 5 minutes	+-	-
	Rayleigh Scattering (OFDR)	Yes < 1 $\mu\text{str}$	Yes 0.1-0.4	Single ended (SMF) Spatial res.: <10mm up to 1mm Range: up to 70m Typ. meas. duration: < 10 seconds	+	-
	Rayleigh Scattering (TW-COTDR)	Yes < 0.5		Single ended (SMF) Spatial res.: 2-20cm Range: 20km Typ. meas. duration: < 10 minutes	++	-
	Rayleigh Scattering (DAS)		Vibration, sound, temperature variation		Single ended (SMF) Spatial res.: > 0.5-5m Range: 1-200km >1kHz	+

Various manufacturers offer optical fiber sensing DAQ units for all kind of optical fiber sensing technologies. The most common commercial manufacturers are listed in Table 2, based on [6] and completed with own data.

A list of FBG and distributed optical fiber sensing cable manufacturers is presented in Table 3. Note that some monitoring companies build their own sensing cables based on commercially available cables. E.g. Com&Sens has its own STRIP technology, converting a bare FBG fiber into a round or flat robust cable (see



Section 3.2). Another example can be found at Buildwise where bare fibers are embedded in a GFRP rod with a longitudinal notch, turning it into a very robust sensing system (see Section 3.2).

An overview of some commercial available interrogators is given in Table 4 for Brillouin based DTSS systems, Table 5 for Rayleigh based DTSS interrogators and Table 6 for Rayleigh based DAS interrogators [14].

Table 2. Manufacturers of OFS DAQ units (based on [6] and completed with own data).

FBG	BOTDR/BOFDR/ BOTDA/BOFDA	RAMAN	OFDR	TW-COTDR	DAS
B-SENS (BE) FBGS (BE/GE) Optics11 (NL) HBK Fibersensing (GE) Sentea Tech (BE) NBG (AU) ...	Febus Optics (FR) fibrisTerre (GE) Omnisens (CH) OZ Optics Neubrex (CA) ...	AP Sensing (GE) NKT Photonics (GE) Sensornet (UK) Silixa (UK) ...	Luna (US) Sensuron (US) ...	Neubrex (CA) ...	AP Sensing (GE) Febus Optics (FR) Fluves (BE) Neubrex (CA) Omnisens (CH) OptaSense (US) Silixa (UK) ...

Table 3. Manufacturers of FBG and distributed optical fiber sensing cables.

FBG	Distributed sensing cables
B-SENS (BE) FBGS (BE/GE) HBK Fibersensing (GE) NBG (AU) Somni Solutions (NL) Technica (US) ...	AFL (US) Fibrain (PO) Fujikura (JP) Helukabel (GE) NanZee (CN) Nerve-Sensors (PL) Neubrex (CA) NBG (AU) OFS (US) Smartec (CH) Solifos (CH) ...

Table 4. Commercial Brillouin based DTSS interrogator units. Based on [14] completed with own data.

Product Name	VISION Dual		Foresight™		NBX-6026	NBX-8200	fTB 5020	G1-R
Company	Omnisens		Oz Optics		Neubrex		FibrisTerre	febus
System	BOTDA	BOTDR	BOTDA	BOTDR	PPP-BOTDA	PSP-BOTDR	BOFDA	BOTDR
Max. length	60km	45km	160km	70km	5km	10km	50km	100km
Channels	4		2 to 25 (internal: 4)		1	1	2 or more	N/A
Min. data interval	25cm	25cm	5cm	5cm	1cm	5cm	N/A	10cm
Min. spatial resolution	50cm	1.5m	10cm	1m	2cm	20cm	20cm*	25cm*
Repeatability	2 μstr 0.1°C	20 μstr 1.0°C	2 μstr 0.1°C	10 μstr 0.5°C	7.5 μstr 0.35°C	5 μstr 0.25°C	2 μstr 0.1°C	4 μstr 0.2°C

\* with spatial resolution enhancement

Table 5. Commercial Rayleigh based DTSS interrogator units. Source: [14].

Product Name	NBX-7031	ODISI 6100	OSI-S
Company	Neubrex	Luna	Semicon
System	TW-COTDR	OFDR	OFDR
Max. length	27km	50m	100m
Channels	1	~8	N/A
Min. data interval	1cm	1.3mm	1.0mm
Min. spatial resolution	2cm	1.3mm	1.0mm
Repeatability	10 nstr 0.001°C	<±0.15 μstr ±0.01°C	1 μstr 0.1°C
Min. sampling frequency	Several minutes	10~250Hz	4Hz

Table 6. Commercial Rayleigh based DAS interrogator units. Based on [14] completed with own data.

Product Name	ODH-4	IDAS	NBX-S4000	Helios® Theta	hDVS	FiberVSP™	HDAS
Company	Optasense	Silixa	Neubrex	Fotech Solutions	Schlumberger	Halliburton	Fluves
System	φ-OTDR	φ-OTDR	TGD-OFDR	N/A	N/A	N/A	Chirped
Max. length	10km	40m	50km	40km	10km	40km	70km
Channels	1	1	1	N/A	N/A	N/A	1
Min. data interval	-	25cm	20cm	N/A	2m	N/A	5m
Min. spatial resolution/ gauge length	2.0m	1.0m	0.2m	1.0m	5.0m	5.0m	10.0m
Min. sampling frequency	~100kHz	0.01Hz~50kHz	1Hz~2.5kHz	~50kHz	5Hz~10kHz	2.5~100kHz	0.001Hz-
Applicable fiber	SMF/MMF	SMF/MMF	SMF	N/A	SMF is better	SMF/MMF	SMF

## 2.4 Temperature and strain compensation

Most (D)FOS technologies are affected by both strain and temperature changes, except from the Raman technology that is only susceptible to temperature changes. When the aim is absolute strain monitoring, it is therefore mandatory to compensate the readings for the temperature effect on the fiber. The strain and temperature compensation coefficients depend on the technology and the cable type used. As the FBG wavelength shift or DFOS frequency shift is linearly proportional to strain and temperature change, the calculation of this compensation is rather straightforward, provided that there are accurate, independent temperature measurements to perform the temperature compensation.

Temperature measurements can be performed with dedicated optical fiber temperature sensing cables or sensors. These cables or sensors are designed to transmit as little strain as possible to the sensor or sensing fiber (see Section 3.2.1).

## 2.5 Free and restrained deformations

FBG and BOFDA sensors measure the real deformation that the structure to which they are attached or built into undergoes. However, in order to also take into account the thermal stresses in the structure, the restrained thermal deformations might be important. In addition to a correction for the influence of the temperature on the optical fiber itself (see Section 2.4), it is therefore necessary to carry out a compensation for the free thermal deformation. In the following paragraphs this will be clarified by means of an example.

The free thermal deformation  $\varepsilon_{T,free}$  of a material with a thermal expansion coefficient  $\alpha_T$  at a temperature change  $\Delta T$  can be calculated as:

---

$$\varepsilon_{T,free} = \alpha_T \times \Delta T$$

The restrained deformation  $\varepsilon_{restrained}$  of the structure is calculated as the difference between the measured (real) deformation ( $\varepsilon_{measured}$ , corrected for the influence of the temperature on the cable/sensor itself) and the free thermal deformation:

$$\varepsilon_{restrained} = \varepsilon_{measured} - \varepsilon_{T,free}$$

To illustrate, when an increase in temperature allows the structure to expand freely (and no differential deformations occur in the section),  $\varepsilon_{measured}$  will be equal to  $\varepsilon_{T,free}$  and the restrained deformation will be equal to 0. When the structure does not allow any dilation,  $\varepsilon_{measured}$  will be equal to 0. The structure does not undergo any real deformation, however there is a build-up of stresses in the structure due to the restraint. The restrained deformation will be equal to  $-\varepsilon_{T,free}$ . The real response of a structure usually lies somewhere between these two extremes.

Again, this shows the importance of accurate temperature measurements when performing long term absolute strain monitoring.

## 3 Practical considerations

### 3.1 Tools and accessories

#### 3.1.1 Fiber cleaning

In theory, it is possible to order optical fiber sensors or sensing cables fully cabled and connectorized. In that case, only a fiber cleaner (and some adapters) would be necessary to connect the fibers to the DAQ unit. The cleaning of fibers is very important to avoid optical losses and to obtain the best measurement performance. Several cleaning solutions are commercially available on the market (Figure 14). It is important to check that the cleaner is compatible with the type of connector or adapter (for an overview of connector types, see Section 3.1.3). The usage of such tools is illustrated in Figure 15 and the effect of cleaning a dirty connector is shown in Figure 16, as observed with a camera inspection tool (see Section 3.1.5).



Figure 14. (a) One-Click cleaner for FC/SC/ST connectors and adapters (image source: Fujikura). (b) A complete fiber cleaning kit, including from left to right fiber wipes, 2 one-click cleaners, cleaning fluid, and cleaning tape for fiber optic connectors (image source: AFL).

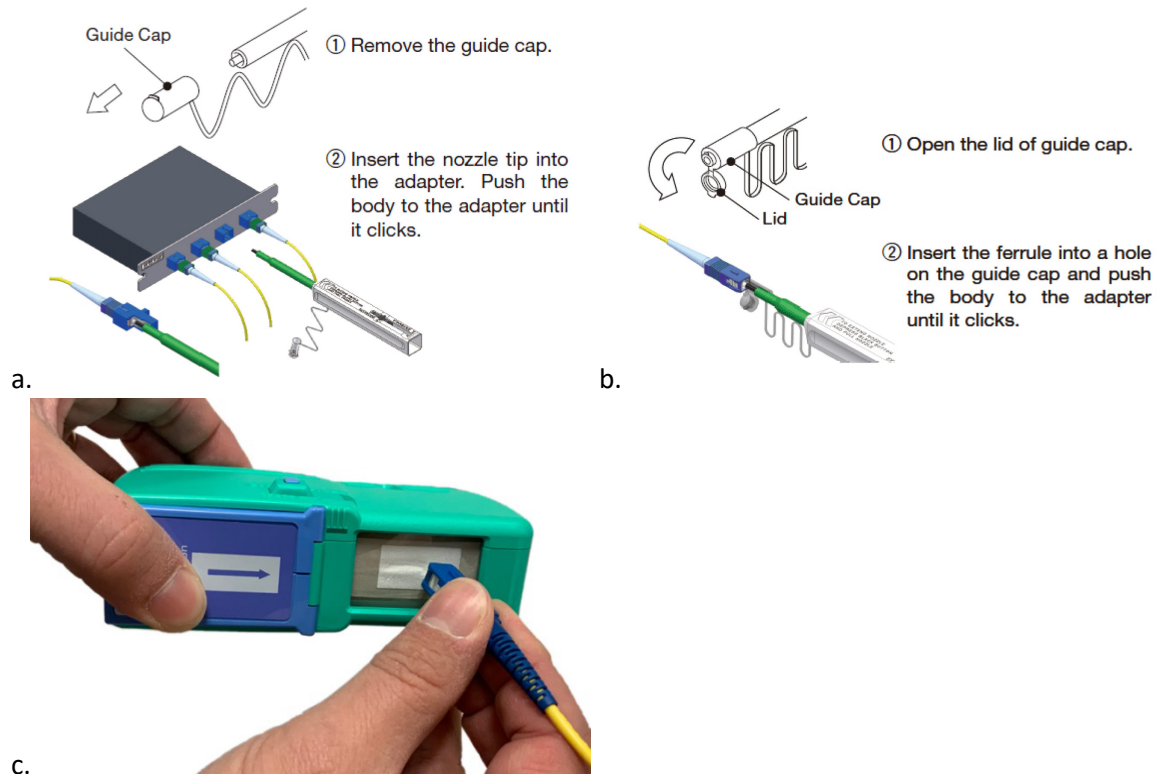


Figure 15. (a) and (b) Functioning of a one-click fiber cleaner (image source: Fujikura). It can be used for both adapter cleaning (a) and ferrule cleaning (b). (c) The use of cleaning tape for fiber optic connectors/ferrules (image source: AFL).

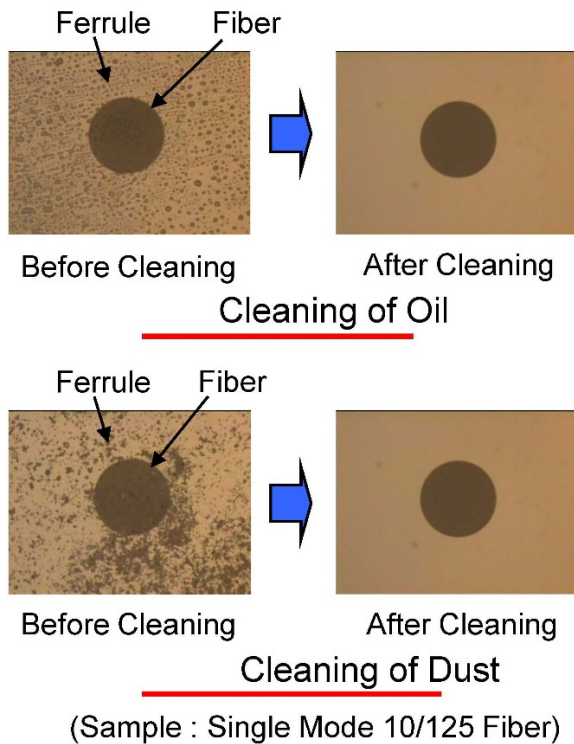


Figure 16. Enlarged image before and after cleaning of the fiber end face or ferrule (source: Fujikura).

### 3.1.2 Splicing

Often, it is not possible to work with completely pre-connectorized fiber cables. The extension of optical fiber cables is possible in various ways. In addition to extending them with adapters (see Section 3.1.3), it is also possible to weld optical fiber cables directly together. This type of connection ('splice') results in the lowest optical losses, if executed properly.

The splicing process consists of several steps:

1. Fiber stripping (removal of the coating) with a dedicated stripping tool (Figure 17). The different coatings are removed one by one up to the fiber cladding (external diameter of 125  $\mu\text{m}$ , see Figure 1 for a typical fiber structure).
2. The stripped fiber end is cleaned with fiber wipes and cleaning agent.
3. The fiber end is cleaved with a dedicated cleaving tool in such a way that the cleavage surface is as flat as possible (fiber cleaver, Figure 17d). The fiber is first fixed in the tool with clamps aligning the fiber to its rotational centre. Then it is cut by an adapted blade at the desired angle.
4. Both fiber ends are placed in the fusion splicer (Figure 18a) and fixed with clamps (Figure 18b). The splicer automatically aligns the fiber cores and fuses or welds them together by an electric arc between 2 electrodes (Figure 18b). Typically, the fusion splicer gives an indication of the quality of the weld and its optical loss after completion.
5. As a final step, the fiber is covered by a protection sleeve (Figure 19). This protection sleeve typically consists of hot-melt glue and a heat shrinkable jacket. An unprotected splice typically resists tensile forces quite well, but breaks easily when subjected to shear (e.g. when it is bended). In some cases, the fiber is recoated over the splice length instead of using protection sleeves. Additionally, special splice protection boxes can be used to protect the splice and avoid stretching or bending.

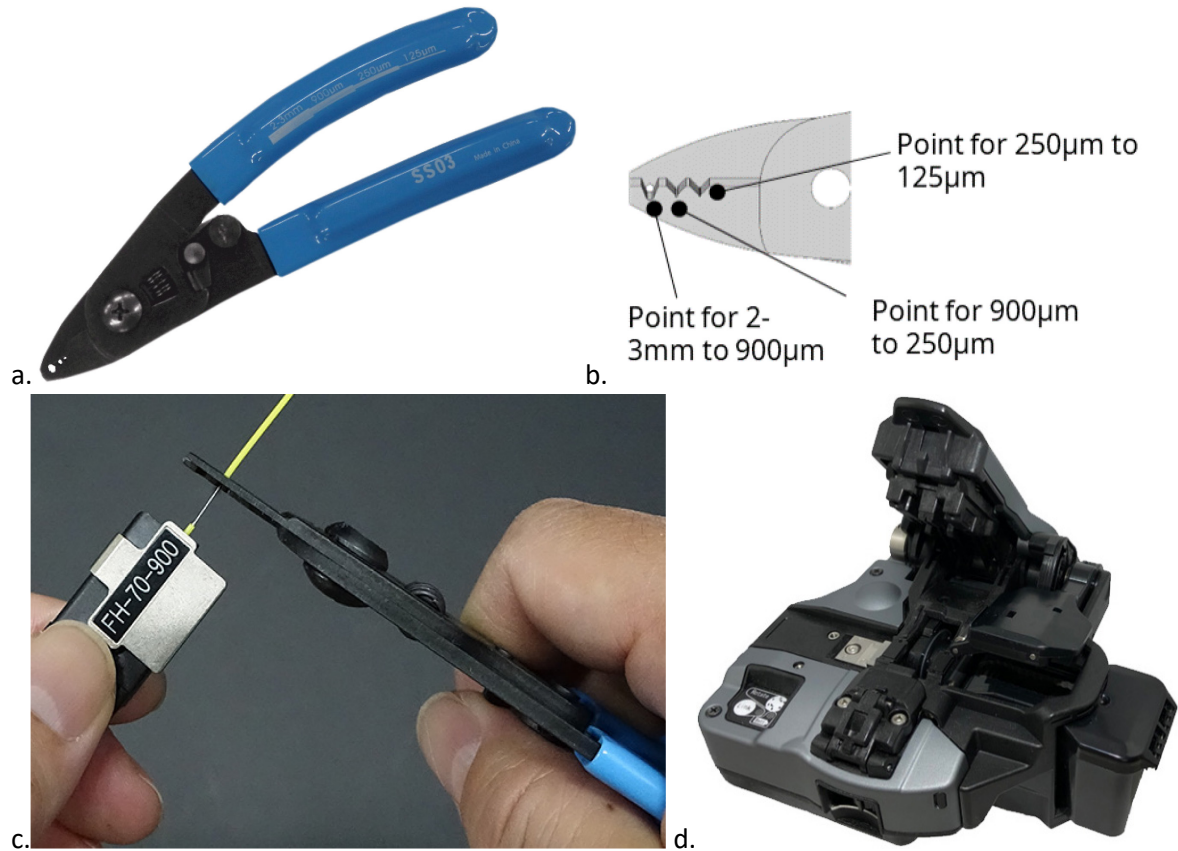


Figure 17. (a) Fiber stripper tool, in this case for 3 different diameters (see image in b). (c) During the stripping of the coating of a fiber. (d) Fiber cleaver. Images source: Fujikura.

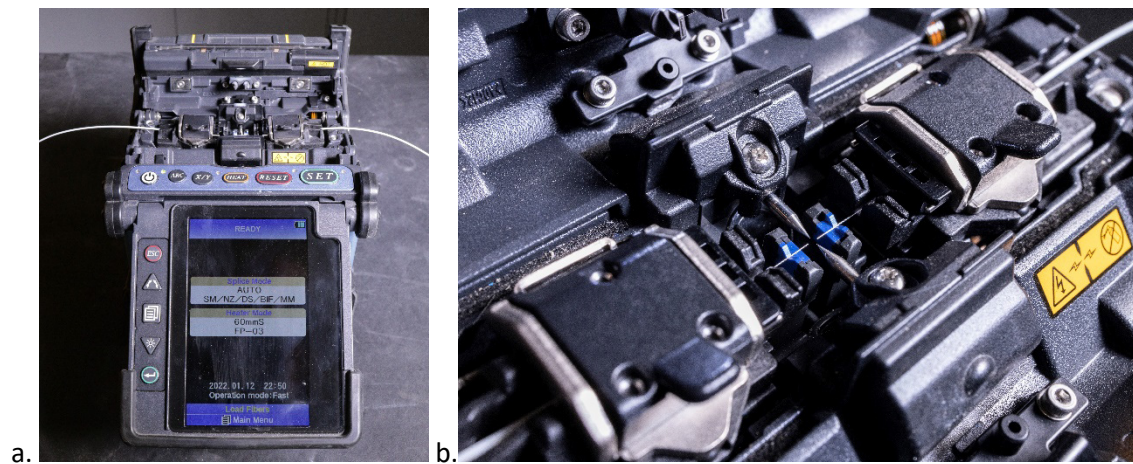


Figure 18. (a) Fusion splicer. (b) Zoom of the fibers fixed in the clamps (white cable left and right) and of the electrodes (in the center of the picture).

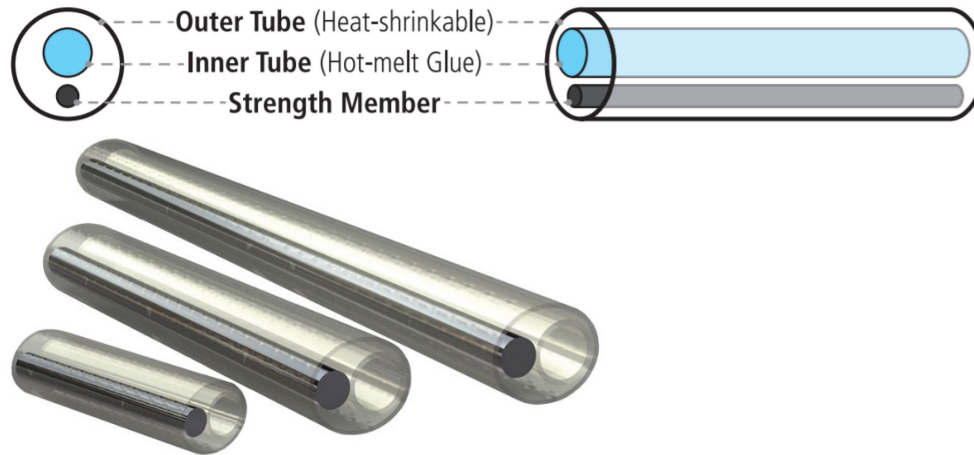


Figure 19. Splice protection sleeves. Image source: AFL.

### 3.1.3 Fiber connectorisation

A faster way to connect fibers than fusion splices is using tools like connectors, adapters, splitters and/or switches. It is important to note that each connection of this type involves optical losses (or attenuation loss). For a connector, a loss of about 0.5 dB is normal, while a fusion splice accounts for a limited loss of only about 0.1 dB. However, in a lot of cases, e.g. when connecting fibers to a DAQ unit, splicing is not feasible. Generally, the use of some connectors on an optical fiber array is not problematic, but it should be avoided as much as possible. Or at least, a well thought connectorisation plan should be prepared at the start of each monitoring setup, minimizing the number of splices and connectors.

The fiber optic industry knows a wide range of fiber optic connectors. Some of the most common connector types are presented in Figure 20a. At present, FC, LC and E2000 connectors are currently the most widely used in optical fiber sensing applications.

Apart from the connector type, the polishing of the connector end is also very important. Several polishing types exist, like FLAT, PC, UPC and APC (see Figure 21a and d). FLAT or plane polishing is used in multimode installations (e.g. Raman sensing technology). PC or Physical Contact polishing has a convex shape and is the most common polishing type in (communication) fiber facilities. UPC or Ultra Physical Contact is similar to PC but the return loss is significantly larger. APC or Angled Physical Contact is polished at an angle of  $8^\circ$ , resulting in the highest return losses. Moreover, light that is reflected back at the connector interface is directed towards the side walls of the fiber where it is absorbed by the fiber jacket, as illustrated in Figure 21c. [17] This avoids that the light is returned back into the source or measurement device, causing additional noise and influencing the overall performance of the system.

Combining different connector types will inevitably result in significant optical losses, as there will be an air gap between both connector surfaces (see for example Figure 21b). Fortunately, an unambiguous colour coding of the connectors is used to avoid erroneous interchange (Figure 20b).



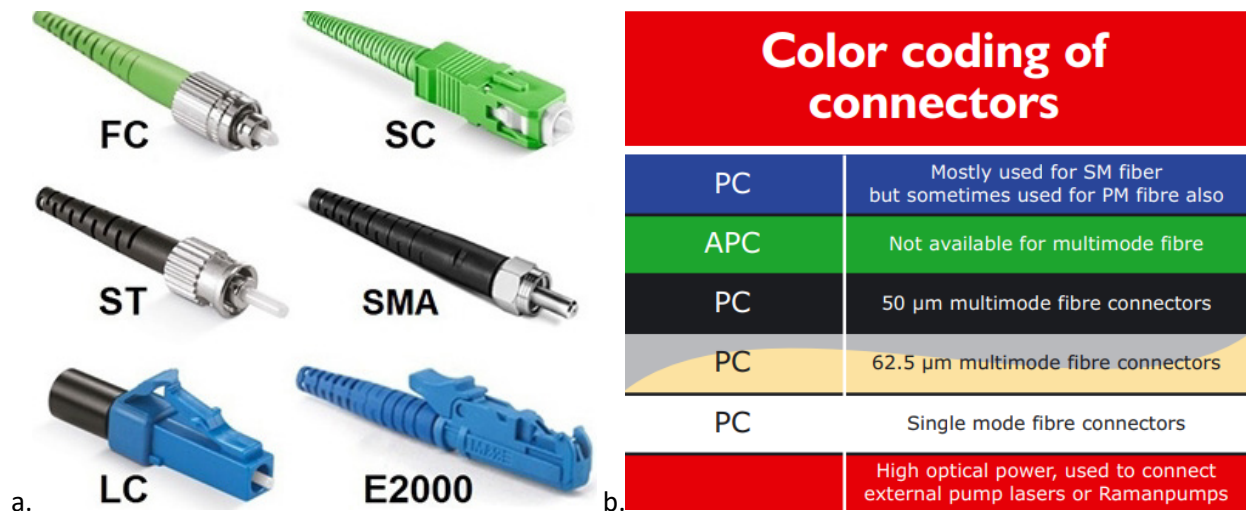


Figure 20. (a) Some of the most common types of optical fiber connectors. Image source: [www.vanteklearning.com](http://www.vanteklearning.com). (b) Colour coding of the polishing, see also Figure 21a and d. Image source: [www.promaxelectronics.com](http://www.promaxelectronics.com).

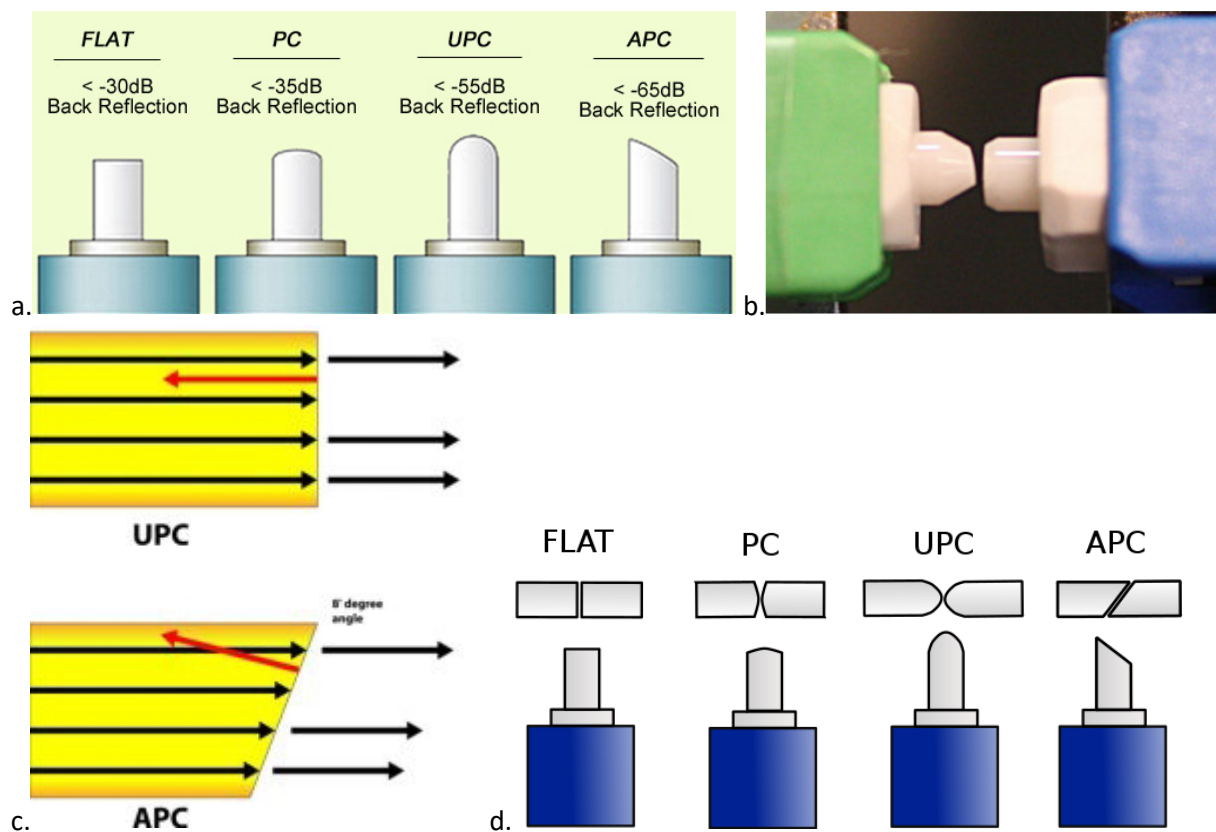


Figure 21. (a) Different types of ferrule end surfaces and polishing. Image source: [www.fiber-optic-solutions.com](http://www.fiber-optic-solutions.com). (b) APC (green) and UPC (blue) connectors are not compatible. Image source: [www.tonercable.com](http://www.tonercable.com). (c) APC connector ends are polished at 8°. Light that is reflected back at the connector interface is directed towards the side walls of the fiber where it is absorbed by the fiber jacket. Image source: [www.vialite.com](http://www.vialite.com). (d) Schematic overview of different types of ferrule and their contact surface. Image source: <https://www.smythsys.es/>.

While the combination of connectors with a different polishing is not a good idea, different connector types can be combined by means of hybrid adapters (Figure 22a). Connectors of the same type can be connected to each other using a coupler (see Figure 22b and c).

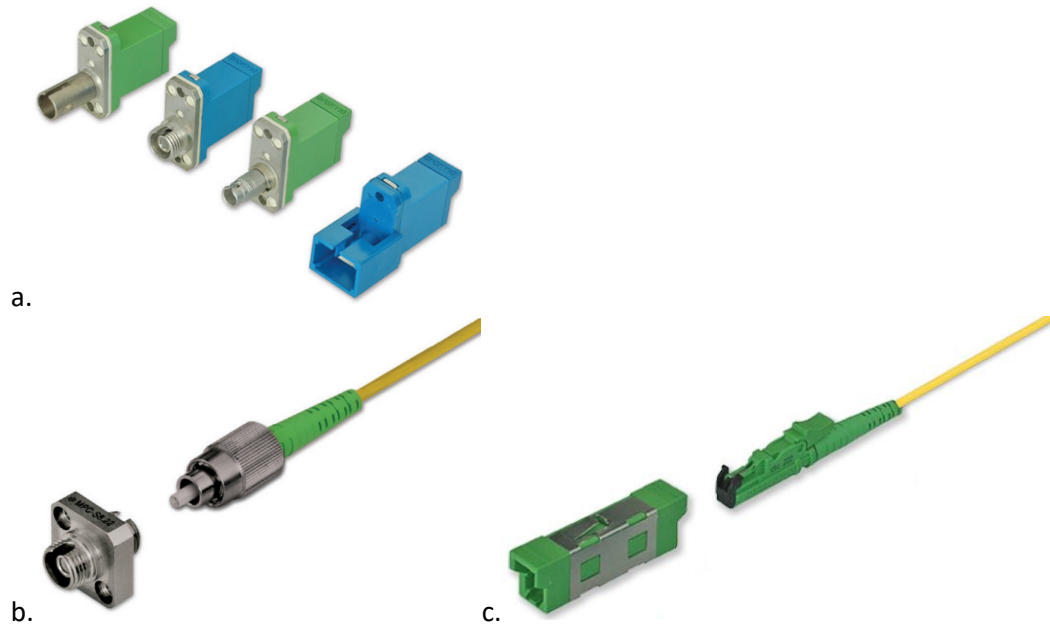


Figure 22. (a) Example of some hybrid adapters. (b) FC coupler. (c) E2000 coupler. Image source: [www.diamond-fo.com](http://www.diamond-fo.com).

Another, more particular way of connecting fibers is via splitters and/or switches. A splitter is able to join two sensor arrays onto one single fiber (Figure 23a). The use of a splitter results inevitably in power losses. There might also be a difference in power between the FBG sensors from both connected arrays, which may result in difficulties for some FBG peak detection algorithms (illustrated in Figure 23b).

Switches or multiplexers actually create additional sensor channels for a DAQ unit, by connecting the sensor channels of the DAQ to these of the switch. The switch runs iteratively over the different switch channels. Of course, there needs to be a continuous communication between both modules, in order to allow a correct identification of the switch channel/sensing fiber that is being interrogated. Typically, adapted switch modules are offered by the interrogator supplier. Figure 24 shows an example of an FBG multiplexer. Similarly, an example of a distributed fiber sensing switch is shown in Figure 25. Note that when using a switch, the maximum frequency of the DAQ device will drop. On the one hand, the maximum frequency of the device has to be divided over a larger number of channels (equal to a factor of the number of channels on the switch divided by the number of channels on the DAQ unit). On the other hand, some delay in response time of the switch has to be taken into consideration as well.

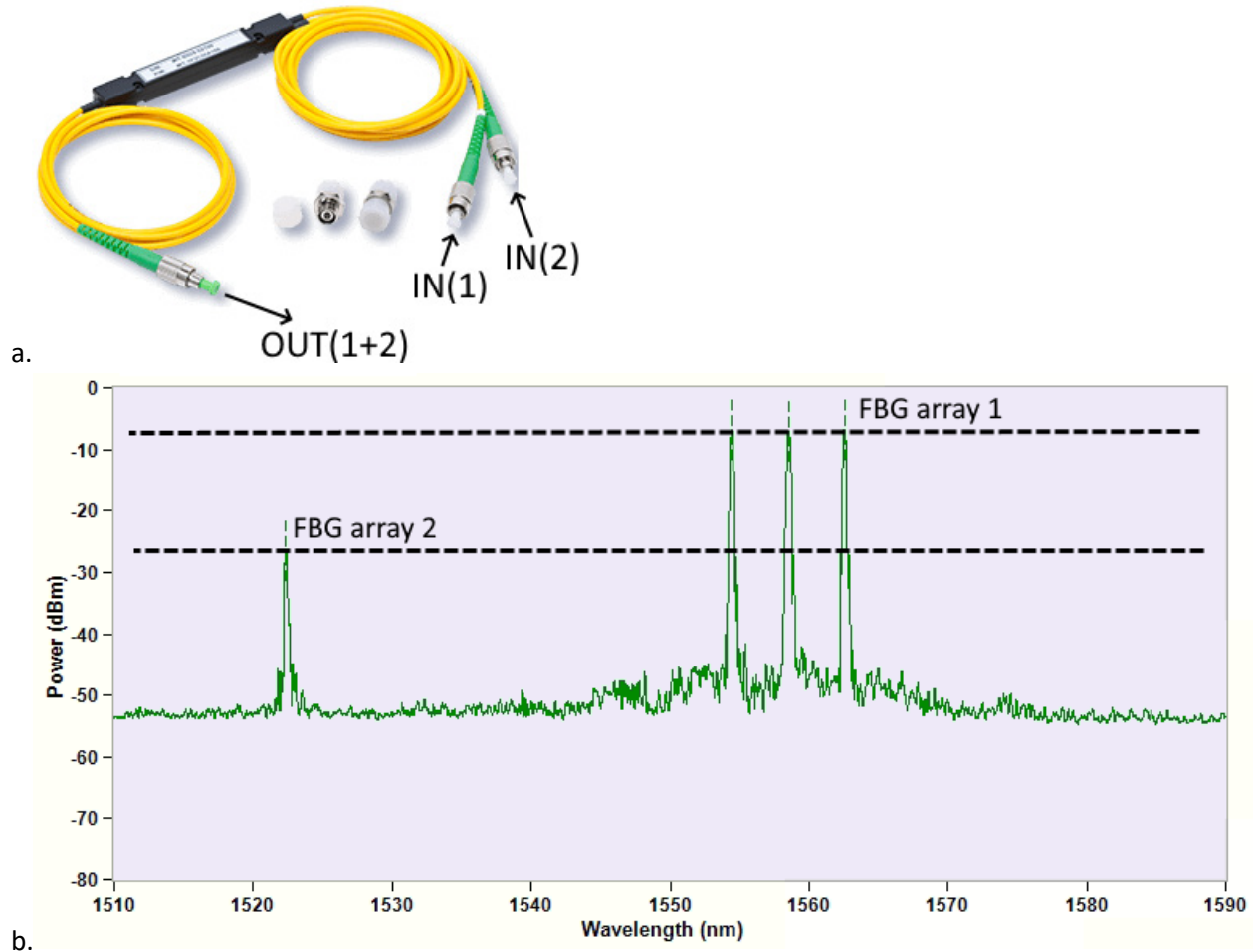


Figure 23. (a) Example of a splitter connecting fibers 1 and 2 onto one single fiber (1+2). Only applicable for FBG sensors. Source: HBM FiberSensing. (b) Illustration of the spectrum of 2 FBG arrays connected to one single fiber with a splitter. The arrays have a different peak power which may lead to peak detection problems in some cases.

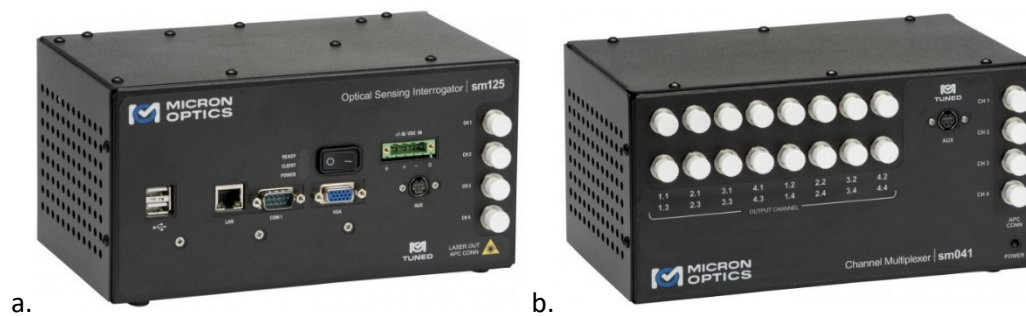


Figure 24. (a) FBG interrogator with 4 sensor channels. (b) Multiplexer module to extend the 4 channels of the FBG interrogator to 16 channels. Source: MicronOptics/Luna.

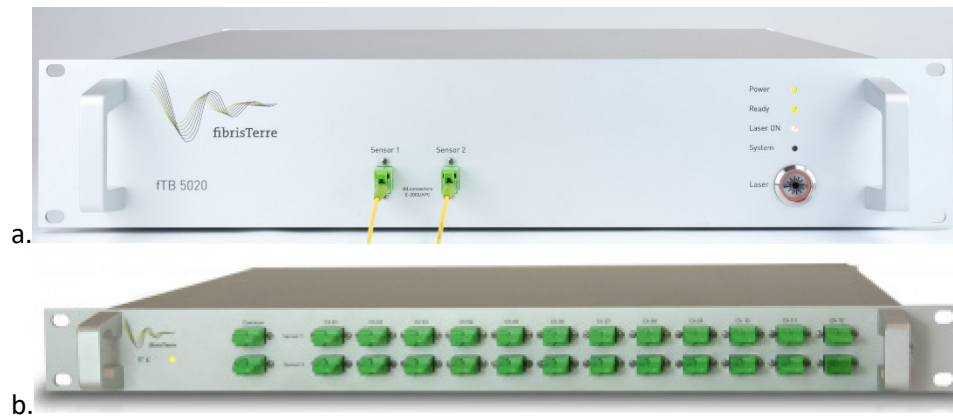


Figure 25. (a) BOFDA interrogator with 2 sensor channels. (b) Switch or multiplexer extending the 2 sensor channels of the BOFDA interrogator to 24 channels. Source: FibrisTerre.

### 3.1.4 Fiber optic cables: patch cords and pigtails

**Patch cords** (or fiber jumpers) are fiber optic cables that are terminated at both ends with a fiber optic connector (Figure 26a). These cables exist in all varieties in terms of connectors, combinations of connector types (e.g. FC at one end and E2000 at the other end), lengths and cable finishing (armoured, ...). **Pigtails** are very similar to patch cords but have only a connector at one end (Figure 26b). Patch cords and pigtails also exist as **multi-strand cables** or **multi-fiber cable assemblies**, i.e. containing multiple fibers terminating each in a separate connector (for example Figure 27).

The standard fiber optic cables are not very robust and only applicable in an indoor, not too harsh environment. Of course, outdoor patch cables with an armoured layout are also commercially available, e.g. protected by additional steel or Kevlar layers or other reinforcement elements.

Similar to the colour coding for connectors (Figure 20b), there is also a universal colour coding for the jacket of optical fiber cables in order to indicate the fiber type (Figure 28). Most optical fiber sensing applications always deal with the yellow (single mode fiber, SMF) or orange (multimode fiber, MMF) jackets. Note that, unfortunately, this colour coding is not always respected when dealing with armoured cables.

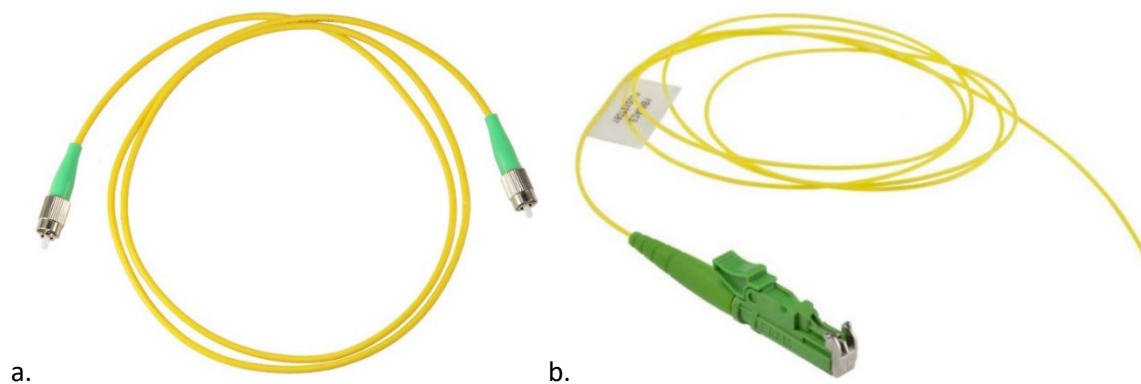


Figure 26. (a) Example of a patch cord with 2 FC/APC connectors. (b) Example of a pigtail with a E2000/APC connector.

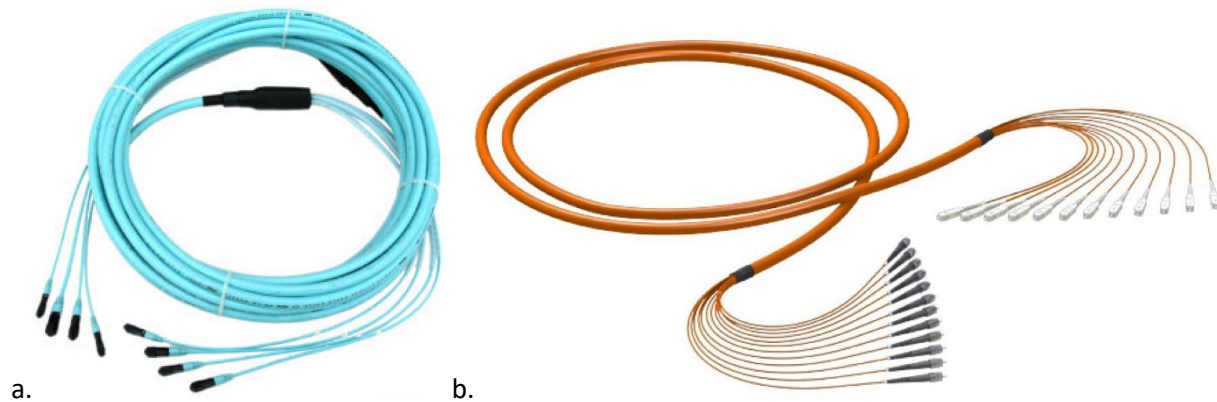


Figure 27. Multi-fiber cable assemblies. (a) From [www.ariatech.com](http://www.ariatech.com). (b) From [www.datatronix.com](http://www.datatronix.com).

Type of optical fibre according to buffer/jacket color
Single-mode optical fiber
Multi-mode optical fiber
10 Gig laser-optimized 50/125 $\mu\text{m}$ MM optical fiber
Outdated color code for MM optical fiber
Sometimes used to designate polarization-maintaining optical fiber

Figure 28. Universal colour coding for optical fiber cable jackets in order to indicate the type of fiber. Image source: [www.promaxelectronics.com](http://www.promaxelectronics.com).

When ordering optical fiber cables, patch cords or pigtails, it is important to check that the fiber type corresponds to the needs of the application (usually clearly mentioned in the user's manual). As mentioned in Section 1.1, optical fibers can be classified into single-mode and multimode fibers, according to the light transmission mode.

Single-mode fibers are divided into 2 categories: OS1 and OS2. Further classification of fibers is often done according to the guidelines of the Standardization Sector of the International Telecommunication Union (ITU-T). In the case of single-mode fibers it is particularly about the ITU-T G.65x series. About 19 ITU-T specifications exist for single-mode fiber, ranging from ITU-T G.652.A over ITU-T G.652.D to ITU-T G.657.D. Each fiber type has its own characteristics and area of application, so choosing the right one is important to assure the best performance of the system.

Multimode fibers are categorized into 4 types: OM1 (62.5/125  $\mu\text{m}$ ), OM2, OM3 and OM4 (all 50/125  $\mu\text{m}$ ), with all varying bandwidth and attenuation properties. The ITU-T specifications collect all multimode fibers under G.651.1.

### 3.1.5 Fiber checkers and testers

Before connecting two optical fibers it is recommended to check the connectors with a **microscope inspection tool** (Figure 29a). This check assures that the connector is clean and avoids potential damage to other parts. An example of the camera view of a microscope inspection tool has been given before in Figure 16. Especially when connecting to a device with fixed connectors like a DAQ unit, a splitter or a switch, this check should not be skipped and can avoid bigger problems like damaging the connector of the device and requiring its return to the production facilities for repair.

Another useful, easy to use tool is a **visual fault locator** (Figure 29b). This tool helps to quickly locate sharp bends and breaks, to conduct end-to-end fiber continuity tests or to perform fiber tracing and identification.

A final testing tool presented here is the **Optical Time Domain Reflectometer (OTDR)** (Figure 30a). This instrument is used to create a footprint of a fiber optic cable route. The analysed data provides information on the condition and performance of the fibers, as well as any passive optical components along the cable path like connectors, splices, splitters and multiplexers (illustrated in Figure 30b). Moreover, the instrument allows to locate the distance to the event/fault. Note that full interpretation of an OTDR trace demands some experience and understanding of the measurement principle. However, even with a basic knowledge a user will be able to detect the location of faults, etc.

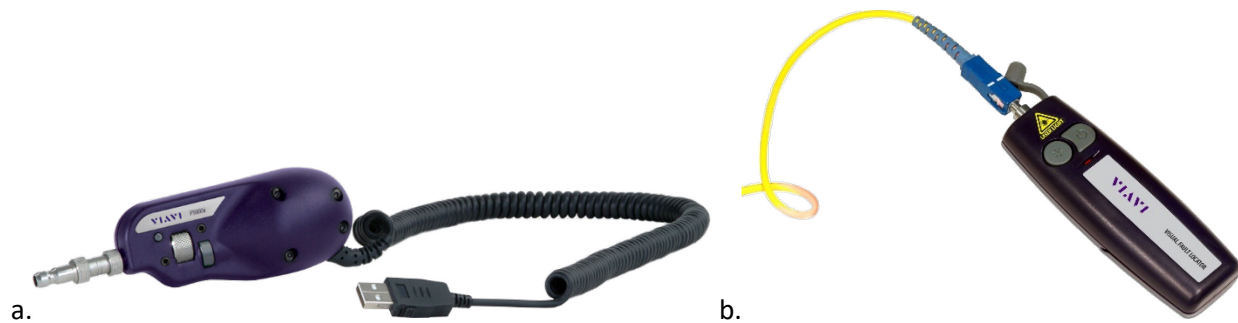


Figure 29. Fiber inspection tools. (a) Fiber microscope. (b) Visual Fault Locator. Image source: [www.viavisolutions.com](http://www.viavisolutions.com).

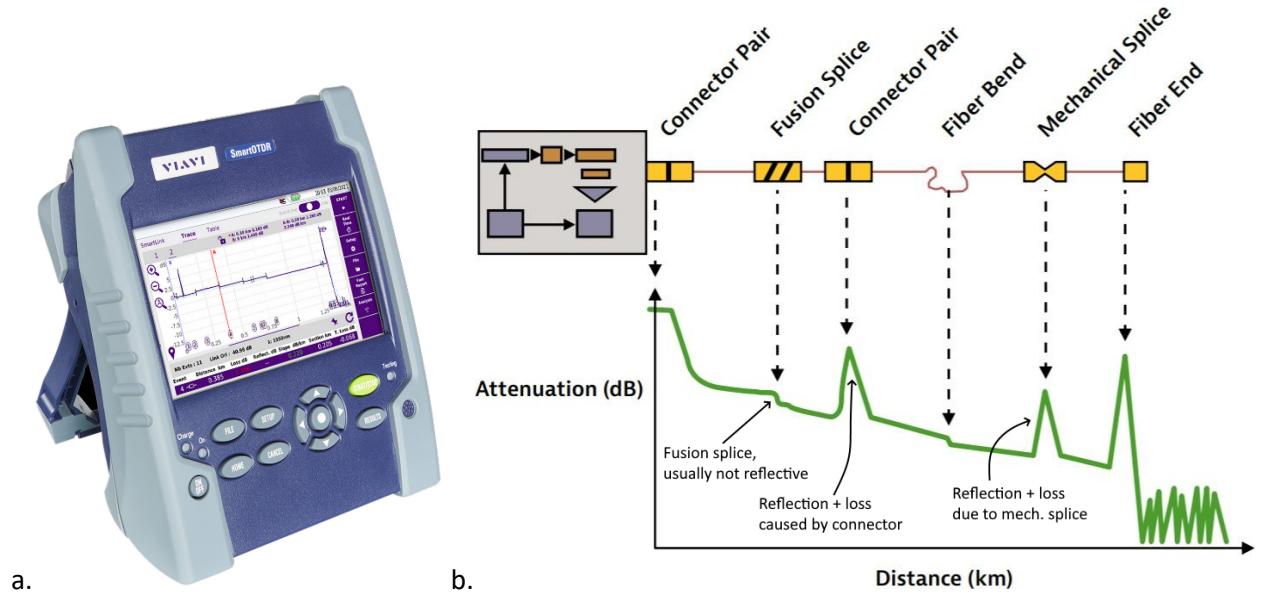


Figure 30. (a) Illustration of an OTDR test device. Image source: [www.viavisolutions.com](http://www.viavisolutions.com). (b) A typical OTDR trace (figure based on [18]).

## 3.2 Types of sensors and sensing cables

### 3.2.1 Strain transfer

#### 3.2.1.1 *Strain sensors and strain sensing cables*

Before continuing with an overview of the large range of optical fiber sensors and sensing cables, it is important to be aware of the strain transfer process between the host material and the optical sensing fiber. After all, there are several interfaces between the element and the optical fiber (i.e. adhesive layers but also protective coatings on the fiber itself). The strain transfer in each interface is achieved through shearing (Figure 31) and depends on the gauge length as well as on the mechanical properties of the coating material [13]. Therefore, it is advisable to perform a proper calibration test or independent control measurements for each (new) application. Note that there is also an upper limit of strain that a fiber cable can accommodate before breaking. Fused-silica fiber has an upper strain limit of approximately 3-5% (i.e. 30 000 to 50 000  $\mu\text{m}/\text{m}$ ).

[2] highlights the fact that the schematic drawing in Figure 31a is only showing one coating layer. In numerous applications, the intermediate layers are many more, i.e. cladding, reinforcement layers, diverse coatings, jackets, etc. They emphasize also the importance of a good insight in the strain transfer mechanism from the substrate material to the fiber core. The ideal (D)OFS cable would be one with the least and thinnest cladding/coating layer possible. In practice, most (D)OFS cables include additional coating layers that protect the core against mechanical and chemical damages. The issue of strain transfer is the most present in the case of strain singularities zones where a high-stress concentration is accumulated over a short length of cable, such as cracks in concrete elements or other discontinuities (Figure 31b). An important note from the authors' side on this topic is that the spatial accuracy and spatial resolution of the applied (D)OFS technique play an important role as well (see Section 1.2 for their definition). When measuring with a (very) high spatial resolution (mm or cm scale), this issue is all the more important. Technologies with a larger spatial resolution will inherently spread (or underestimate) local strain peaks.

[2] refers to the research of 2 groups on this topic. [15] recently developed a state-of-the-art review on the strain transfer theory of optical fiber-based sensors developed for civil structures. [19] reported amongst others some comparative tests for concrete crack monitoring with different DFOS cable types. More recently, an interesting study was published about crack monitoring in concrete with DFOS cables by [20]. This study clearly shows the influence of cable type on measurement results and crack detection capabilities (Figure 32).



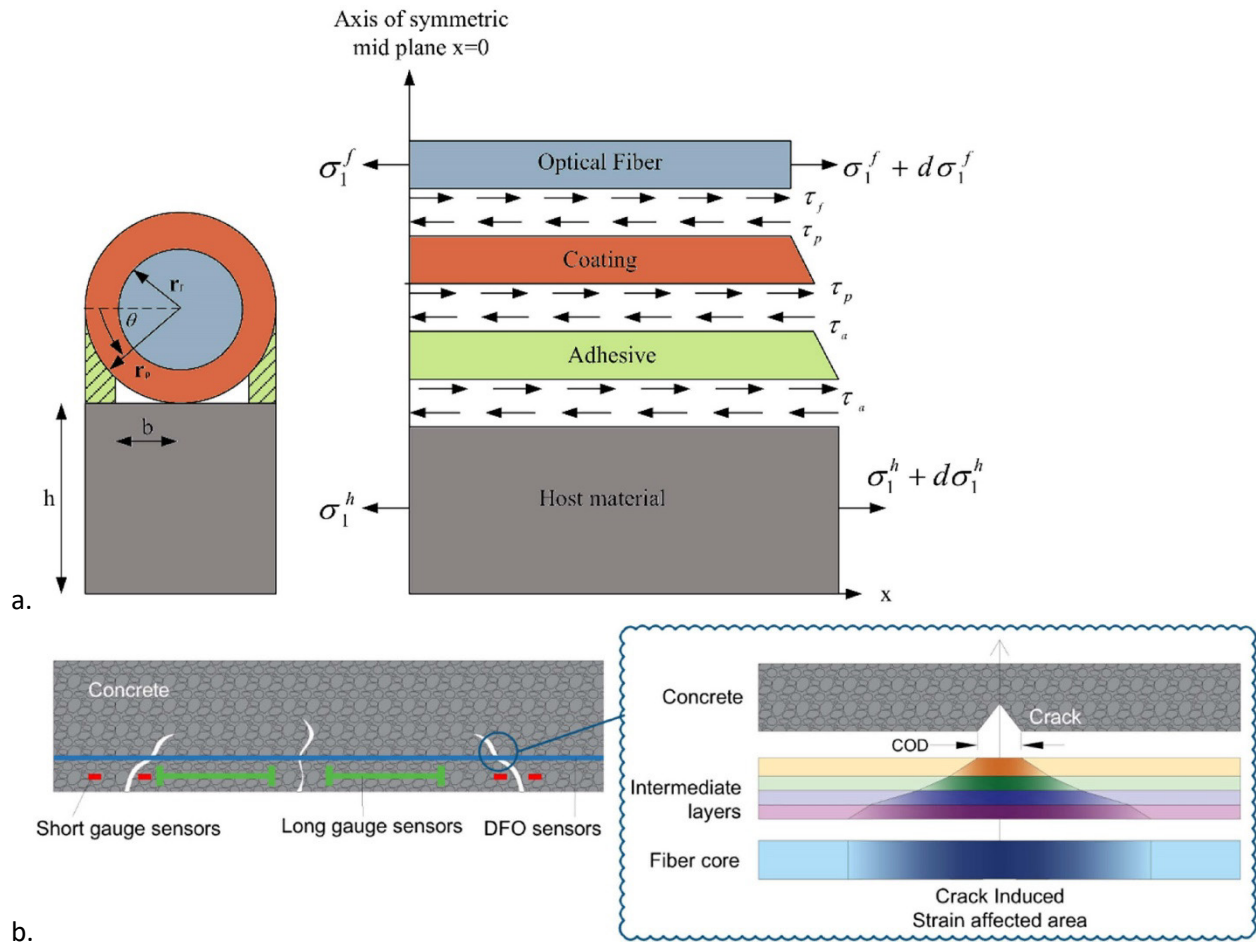


Figure 31. (a) Free body diagram for the symmetrical section of the optical fiber and the substrates together with their relative shear transfer. [2] (b) Illustration of strain transferring between the substrate over the intermediate layers to the fiber core near a crack. Source: [19].

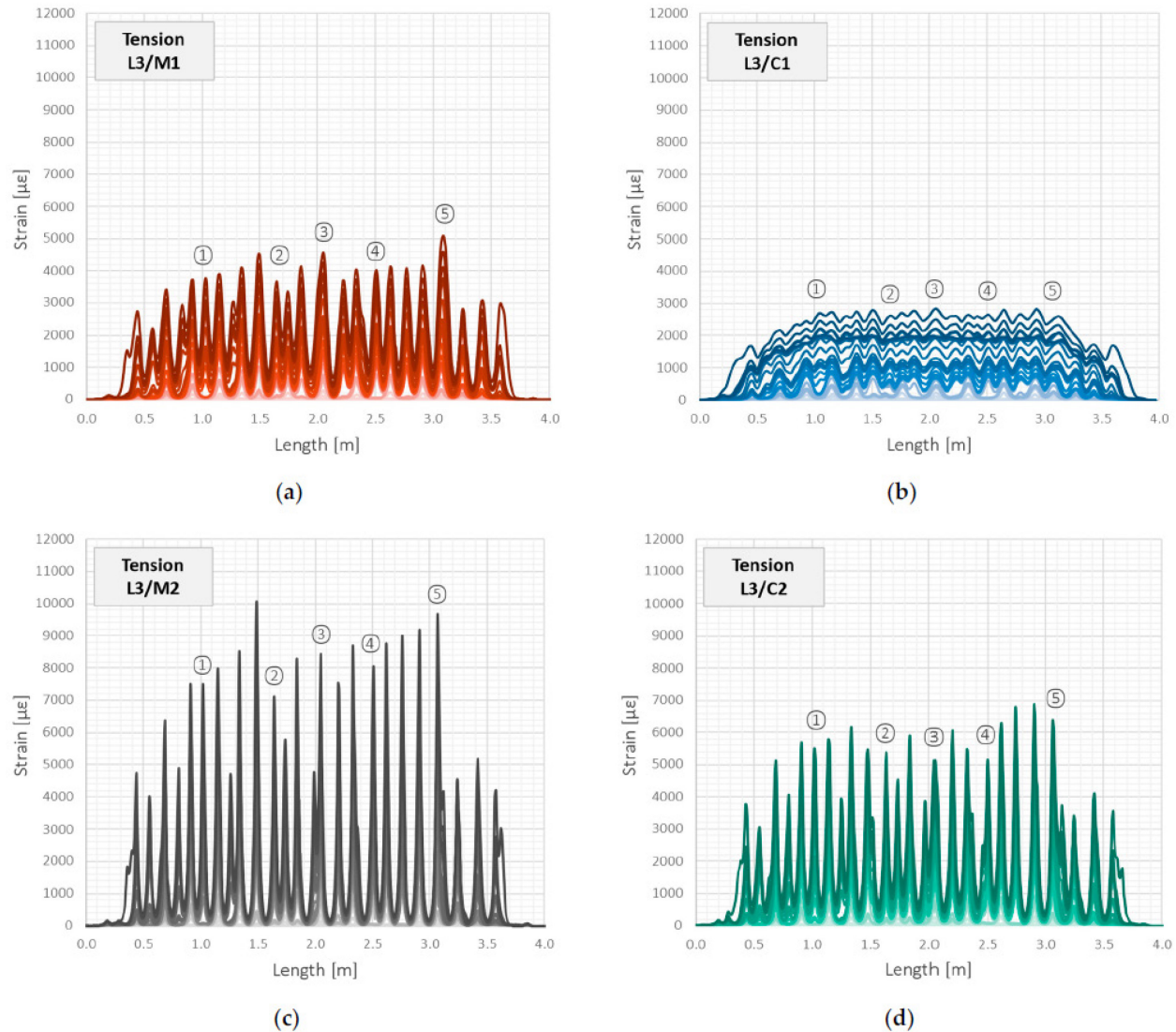


Figure 32. DFOS measurements (Rayleigh-based device) in the tension zone of a reinforced concrete beam (L3) during a bending test. M1 and M2 are monolithic sensor cables, C1 and C2 are layered sensor cables. Source: [20].

At Buildwise, some optical fiber pull-out tests have been conducted based on the Kelly-Bryant method in order to assess the cable adherence to concrete and the time needed to obtain a minimal adherence between both in function of the setting time of the concrete. This is important information when interpreting the optical fiber measurements in early age concrete, e.g. in terms of restrained shrinkage and thermal deformations (see for example the monitoring case described in Section 5.1.3). The optical fiber cables (Solifos V9 and Fibrain VC-DCY, see Table 7 for their characteristics) were installed in 15 cm high moulds (Figure 33a). Comparative tests with smooth steel reference bars (10 mm diameter) have been performed as well (Figure 33b). A concrete composition without and with superplasticizer has been used, which delays the setting time of the concrete. The results of these tests are presented in Figure 34 and show that both optical fiber cable types develop a faster and higher adherence to the concrete than the steel reference bars. This clearly demonstrates that these optical fiber setups will be able to capture

strain changes in early age concrete, making it a very suitable and interesting device to monitor restrained shrinkage and thermal deformation phenomenon. The high adherence between the Solifos V9 cable and the concrete led to failure of the fiber sensing cable interface between the PA coating with irregular surface and the inner steel tube (Figure 33c). The adherence of the Fibrain VC-DCY cable with a smooth surface is clearly smaller than for the Solifos V9 cable. However, it is still higher than for the steel reference bars.

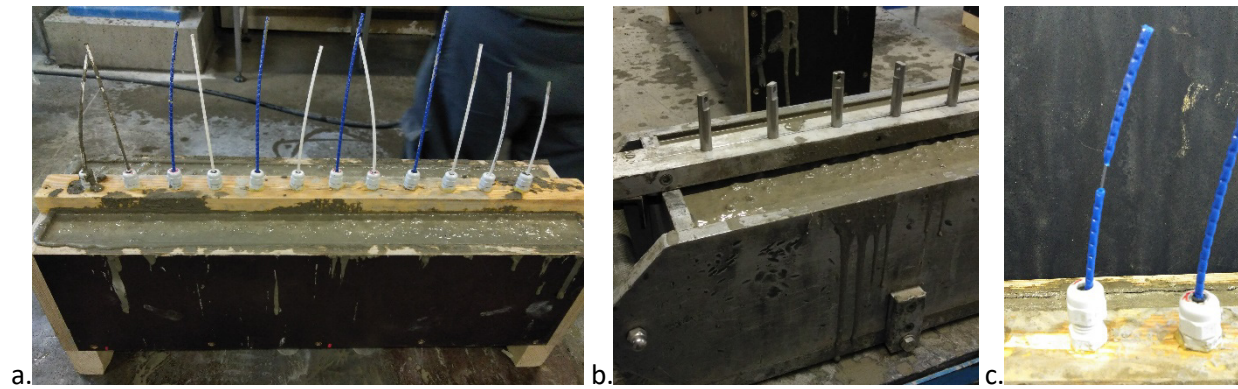


Figure 33. Kelly-Bryant pull-out tests. 15 cm high moulds with (a) the blue Solifos V9 and the white Fibrain VC-DCY cables and (b) the smooth steel reference bars (diameter 10 mm). (c) Tearing off the blue PA coating of the Solifos V9 cable.

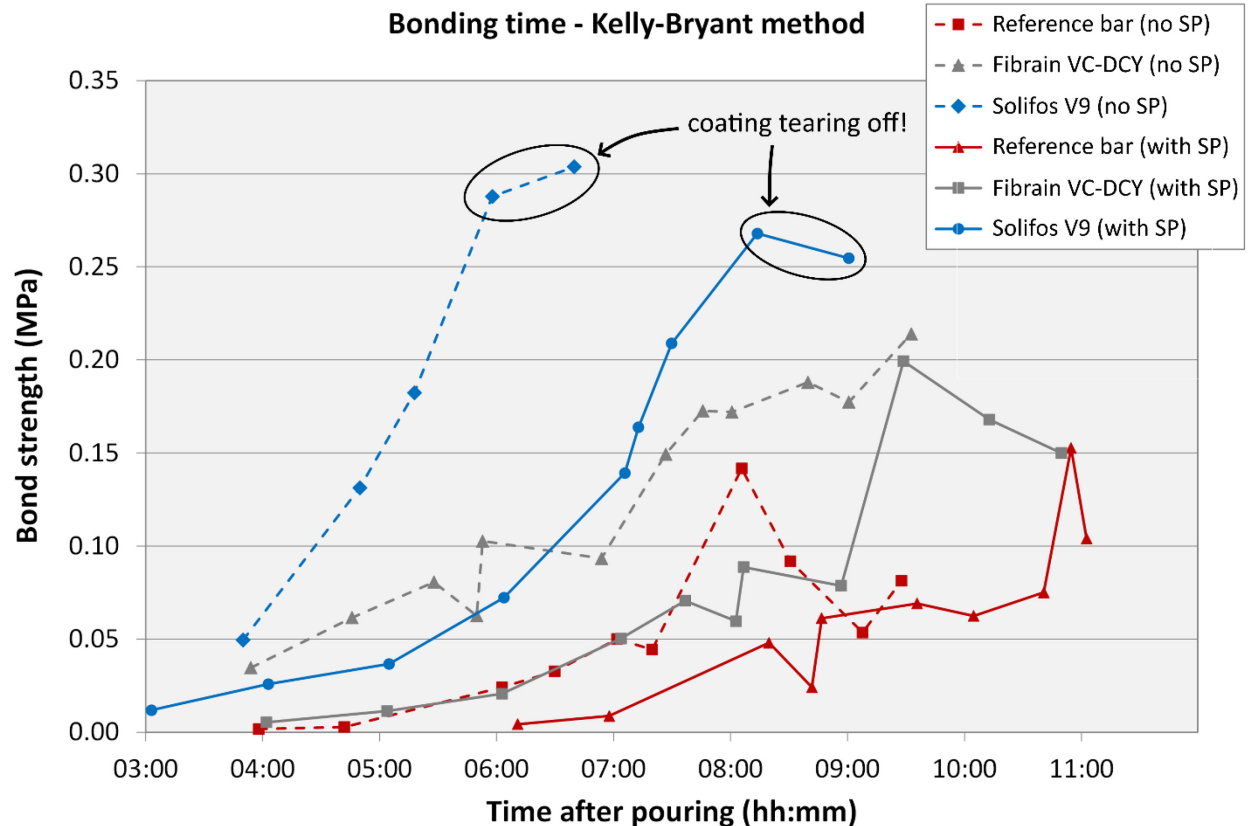


Figure 34. Test results of Kelly-Bryant pull-out tests at Buildwise. 3 types of fibers were tested, in this case on concrete without and with superplasticizer (SP).

### 3.2.1.2 Temperature sensors and temperature sensing cables

For temperature sensors and sensing cables, the reasoning is completely opposite as for strain sensing. Remember that most optical fiber sensing technologies are subject to both strain and temperature variations (apart from the Raman technology, see Section 0). As strain variations disturb the temperature measurement and its accuracy, a temperature sensor or sensing cable should capture as little strain as possible from its surroundings. Obviously, the sensor or sensing cable should also be as sensitive as possible to temperature variations. One of the challenges here is to combine these properties into a robust solution.

### 3.2.2 (Multi-)point sensors

FBG and other fiber optic (multi-)point sensors are commercially available in a wide range of varieties. They can be bought as individual sensors or in the case of FBG sensors on a chain of multiplexed sensors (each FBG with its specific reflecting wavelength). An overview of the wide application range is given below:

- Strain sensors (Figure 35 and Figure 36)
- (High) temperature sensors (Figure 37)
- Acceleration sensors (Figure 38)

- Displacement sensors (Figure 39)
- Pressure sensors (Figure 40)
- Inclination sensors (Figure 41)
- Hydrogen sensors (Figure 42a)
- Infrared sensors (Figure 42b)



Figure 35. FBG strain sensors. (a) Surface mountable (by welding, gluing, ...) and embeddable strain sensors (HBK FiberSensing). (b) 2mm GFRP coated FBG array (FBGS). (c) Polyimide coated FBG sensors (Luna).



Among those sensors, the Optical Strand measures elongation, which corresponds to a deformation of the structure, very accurately.



Figure 36. (a) Illustration of the OSMOS optical strand to measure elongation. Standard measurement base of 1 and 2 m. (b) The strand attached to the bottom of reinforced concrete bridge. Source: [www.osmos-group.com](http://www.osmos-group.com).

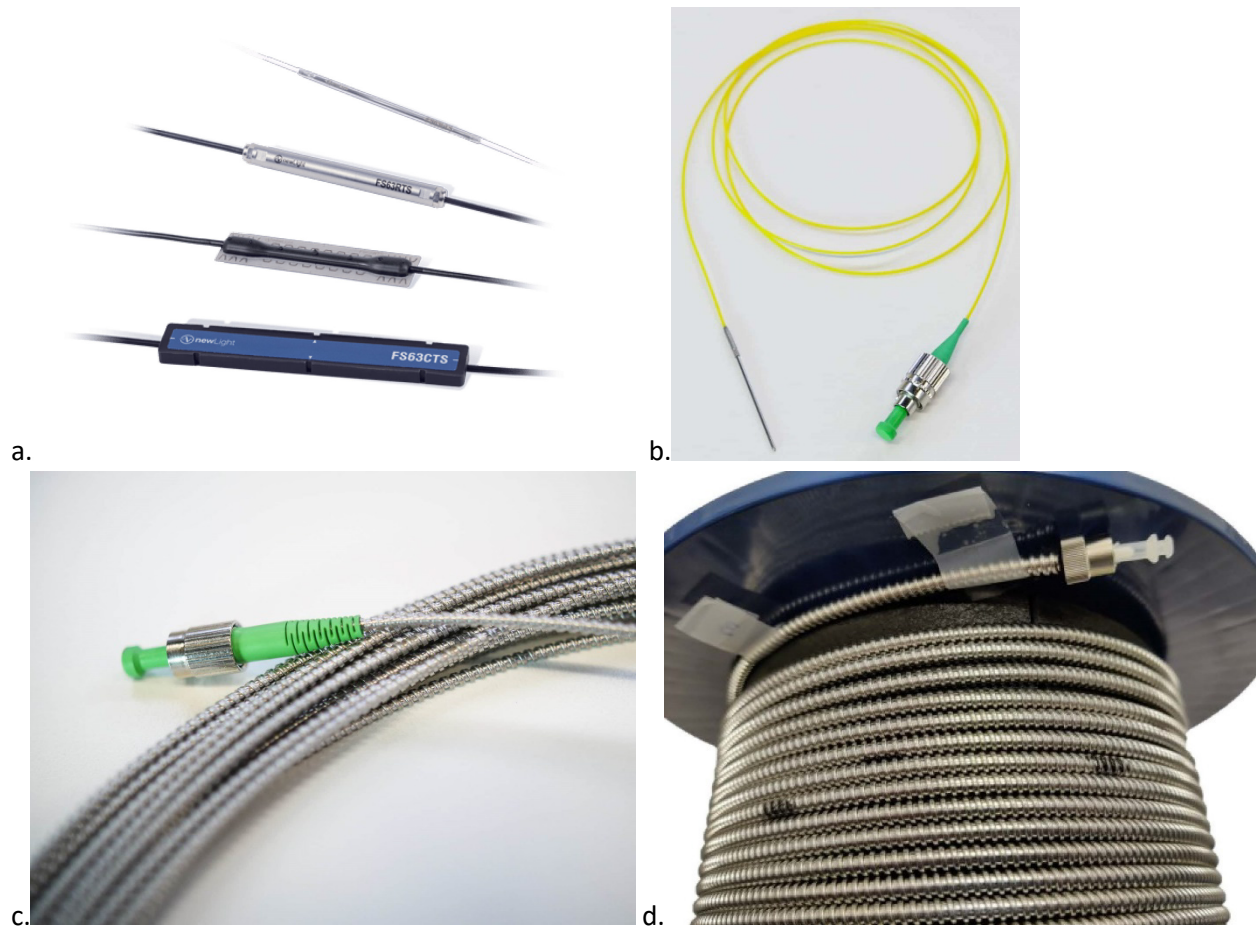


Figure 37. FBG temperature sensors. (a) Surface mountable (by welding, gluing, ...) and embeddable temperature sensors (HBK FiberSensing). (b) Single temperature sensor (FBGS). (c) Spliceless chain of temperature sensors in a 1mm stainless steel tube (FBGS). (d) Chain of high temperature sensors (up to 650°C) in a 2.3 mm stainless steel tube (B-Sens).

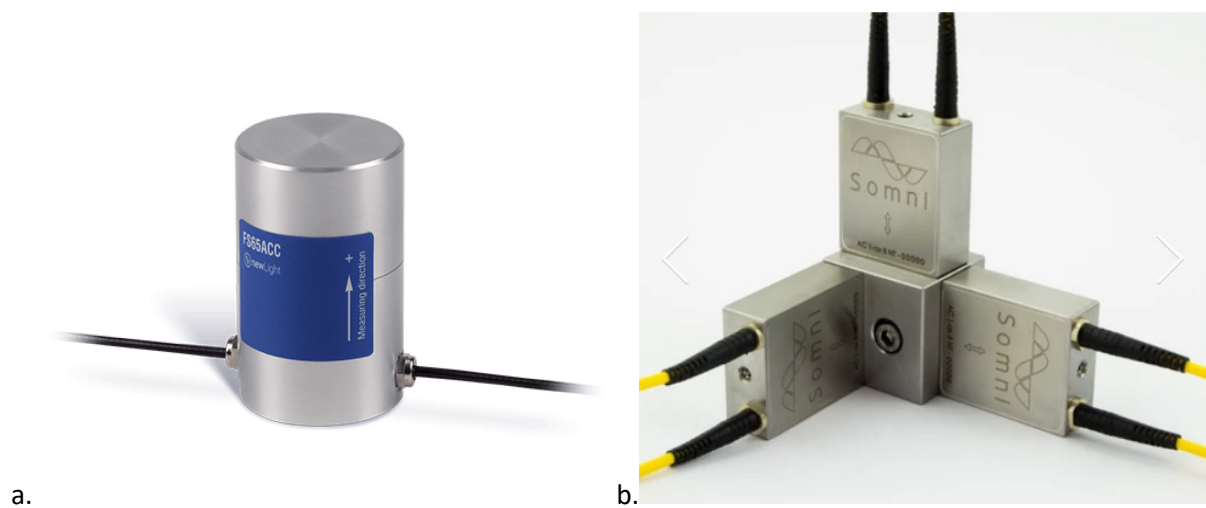


Figure 38. FBG-based accelerometers by (a) HBM and (b) Somni Solutions.



Figure 39. FBG-based displacement sensors by (a) HBM and (b) Technica.



Figure 40. Liquid and gas pressure sensor (Technica).



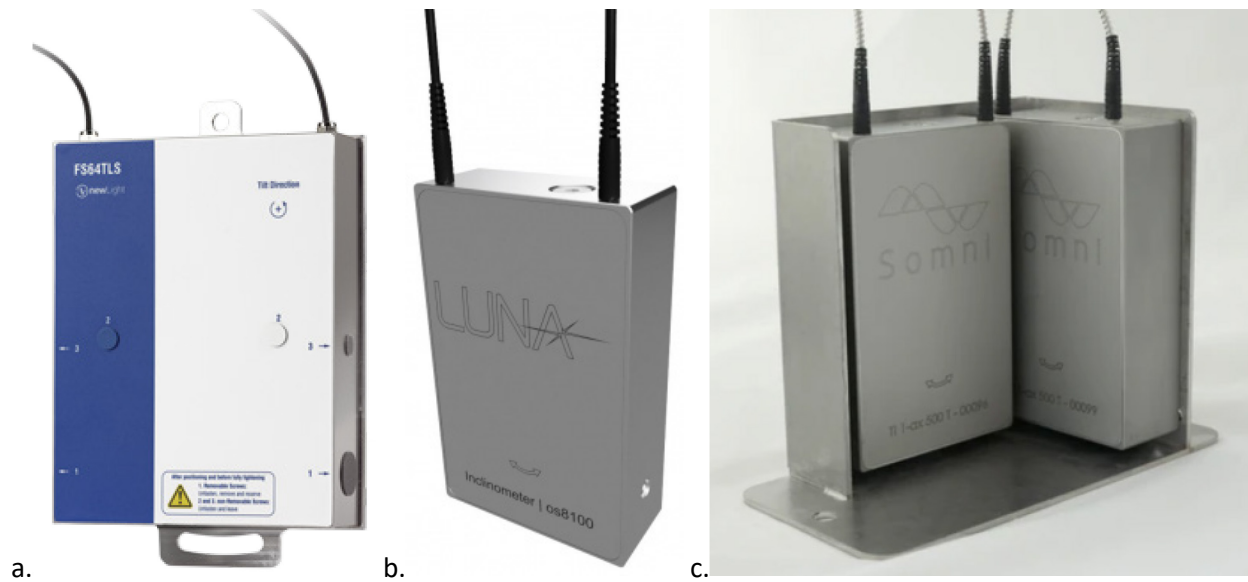


Figure 41. FBG-based tilt sensors by (a) HBM, (b) Luna and (c) Somni Solutions.

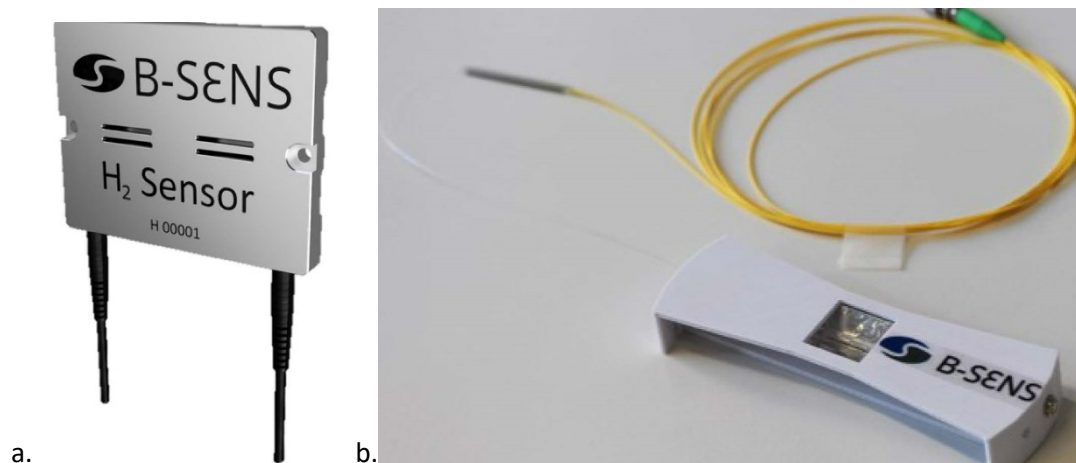
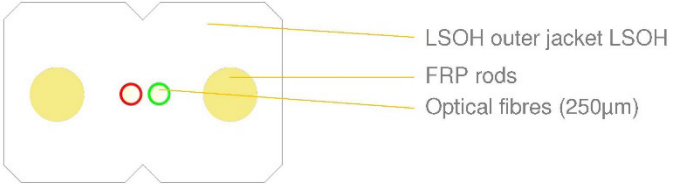
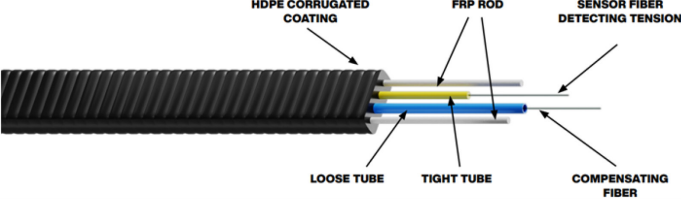


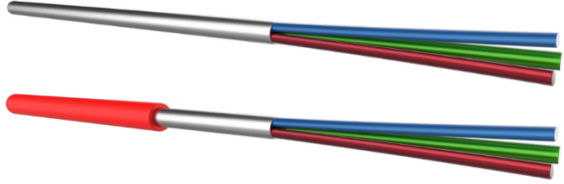
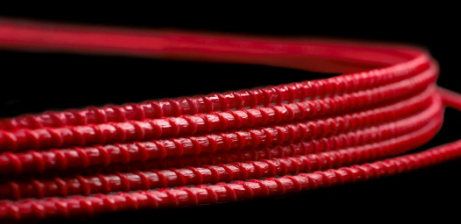




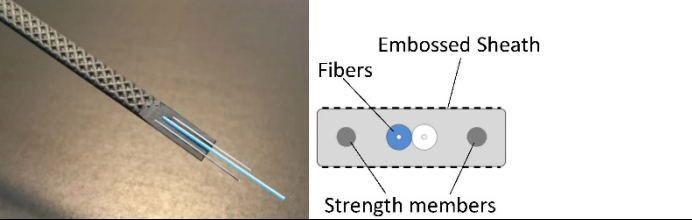
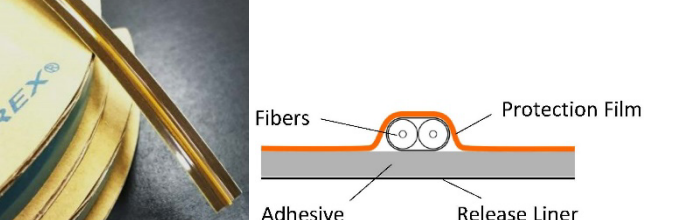
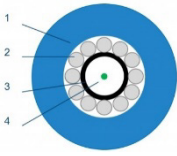

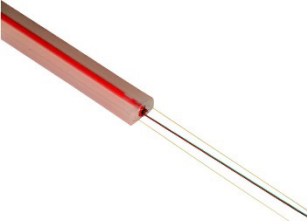
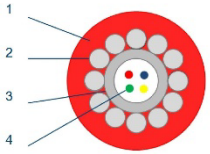
Figure 42. (a) Hydrogen sensor based on a  $H_2$  sensitive coating applied on the fiber (B-Sens). (b) “Early flame detector” based on an infrared sensitive coating applied on the fiber (B-Sens).

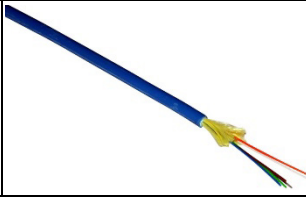
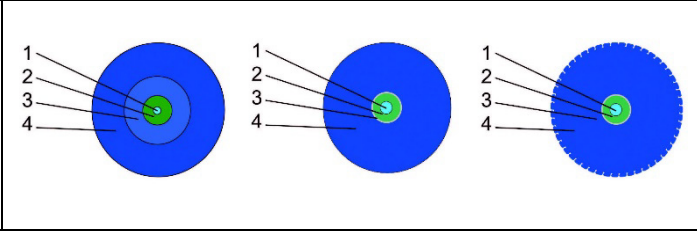
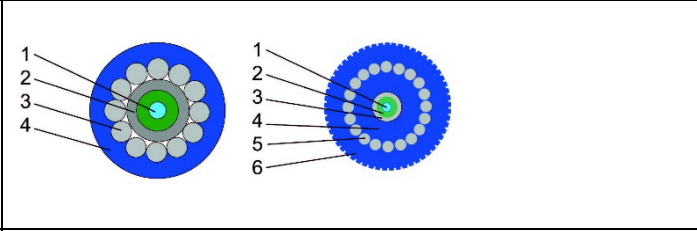
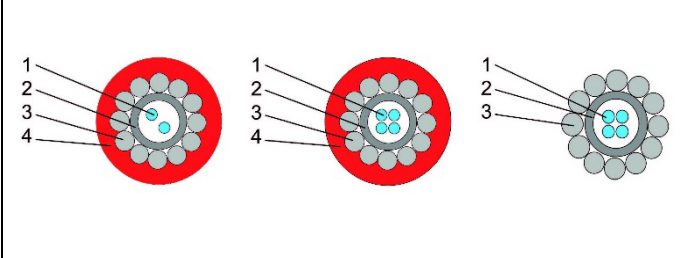
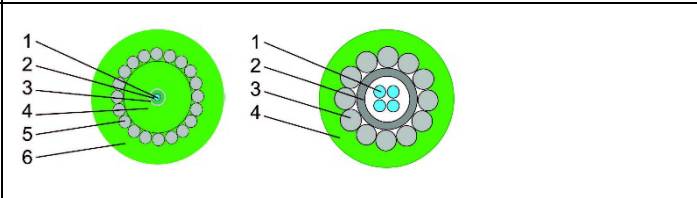
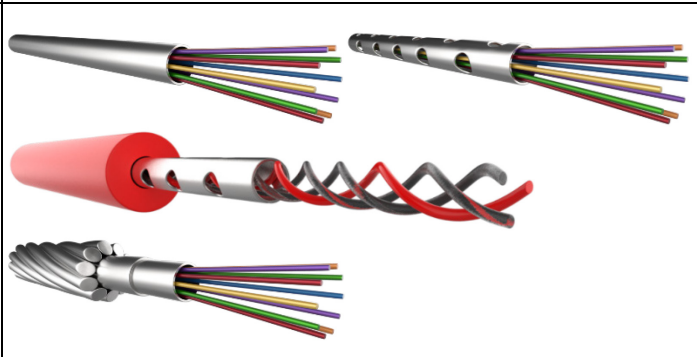
### 3.2.3 Distributed sensing cables

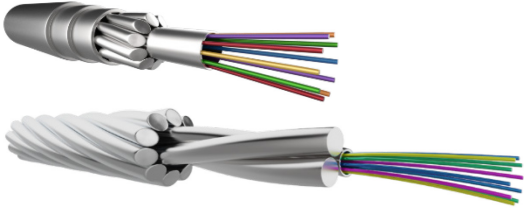
There is a very wide range of distributed sensing cables commercially available on the market for all kind of applications. They vary in diameter, coatings, robustness, cost price, weight, tensile strength, etc. This paragraph does not aim to present all available fiber types and manufacturers. It does try to give an overview of the wide range of possibilities (see Table 7). Remember that strain and temperature sensing cables demand a different cable design. This also applies for acoustic sensing. Most cable designs are applicable for a variety of DOFS technologies by specifying the characteristics of the sensing fiber when ordering. Some cable designs even allow the integration of multiple fiber types.

Table 7. Overview of distributed strain, temperature and/or acoustic sensing cables.

<p><b>Fibraint VC-DCY – FTTH LSOH flat drop cable</b>                  Standard telecommunication fiber, 1 fiber variant shows good strain sensing capabilities                  LSOH outer jacket, 2 FRP reinforcing rods                  Dimensions: 3.1 x 2.0 mm<sup>2</sup>                  Price: -</p>	 <p>LSOH outer jacket LSOH                  FRP rods                  Optical fibres (250µm)</p>
<p><b>Fibraint DSST-01</b>                  Dedicated strain and temperature sensing cable                  Structured HDPE outer jacket                  Dimensions: 10 x 4.3 mm<sup>2</sup>                  Price: +</p>	 <p>HDPE CORRUGATED COATING                  FRP ROD                  SENSOR FIBER DETECTING TENSION                  LOOSE TUBE                  TIGHT TUBE                  COMPENSATING FIBER</p>
<p><b>HELUKABEL Helucom A-DQ(ZN)B2Y</b>                  Temperature sensing cable                  PE outer sheath, armouring through glass yarns, fiber in loose tube                  Diameter: 10.0 mm                  Price: -/+</p>	 <p>HELUCOM® A-DQ(ZN)B2Y</p>
<p><b>HELUKABEL Helucom A-DSQ(ZN)B2Y</b>                  Temperature sensing cable + heating cable by 2 or 4 copper wires = “hybrid cable”                  PE outer sheath, armouring through glass yarns, fiber in loose tube                  Diameter: 12.0-15.0 mm                  Price: +-</p>	 <p>HELUCOM® A-DSQ(ZN)B2Y</p>
<p><b>NBG Trisens core/cable</b>                  Dedicated strain, temperature or acoustic sensing cable                  PA coating (Trisens cable), anti-corrosive high-grade steel tube containing 3 fibers (both Trisens core and cable)                  Diameter: 1.3mm (core), 3.0mm (cable)                  Price: ?</p>	
<p><b>Nerve-Sensors EpsilonRebar</b>                  Dedicated strain (and temperature) sensing cable                  GFRP (glass fiber + epoxide) coating                  Diameter: 5 – 20 mm (standard 5 mm)                  Price: ++</p>	
<p><b>Nerve-Sensors EpsilonSensor</b>                  Dedicated strain (and temperature) sensing cable                  PLFRP (polyester fiber + epoxide) coating                  Diameter: 3 mm                  Price: +</p>	

<p><b>Nerve-Sensors 3DSensor</b>                  Dedicated strain sensing cable, which allows the determination of displacements.                  PLFRP (polyester fiber) + PE coating                  Diameter: 45 x 12 mm<sup>2</sup>                  Price: ++</p>	
<p><b>Neubrex FutureNeuro FN-SILL-3</b>                  Dedicated strain and temperature sensing cable                  Embossed sheath (olefin elastomers) with 2 reinforcing bars                  Dimensions: 4.3 x 1.7 mm<sup>2</sup>                  Price: ?</p>	
<p><b>Neubrex FutureNeuro FN-SSL-3</b>                  Dedicated strain and temperature sensing cable                  Very thin back-sheet (&lt;1.0mm) with a protecting surface film                  Dimensions: 8.0 x 1.0 mm<sup>2</sup>                  Price: ?</p>	
<p><b>Smartec HDPE strain sensor</b>                  Dedicated strain sensing cable                  HDPE outer sheath with interlocking system, steel armoring and metal tube                  Diameter: 3.5mm                  Price: ?</p>	
<p><b>Smartec SMARTape II</b>                  Dedicated strain sensing cable                  Glass Fiber Reinforced Polymer/Epoxy tape                  Dimensions: 9.90 x 0.32 mm<sup>2</sup>                  Price: ?</p>	
<p><b>Smartec SMARTprofile II</b>                  Dedicated strain and temperature sensing cable                  PE thermoplastic body with both free and bonded fibers                  Dimensions: 8.0 x 4.0 mm<sup>2</sup>                  Price: ?</p>	
<p><b>Smartec temperature sensing cable</b>                  Dedicated temperature sensing cable                  PA outer sheath, stainless steel wires and steel loose tube.                  Dimensions: 4.8 mm                  Price: ?</p>	 <p>1 PA outer sheath                  2 Stainless steel wires, 316L                  3 Stainless steel loose tube, 316L                  4 Bend insensitive optical fibers</p>

<p><b>Smartec Hydro and Geo Sensing cable</b>                  Dedicated temperature sensing cable                  PU outer jacket (LSZH-NC), aramid yarn layer, central strength member/filler                  Diameter: 6.0mm                  Price: ?</p>	
<p><b>Solifos BRUsens LLK-BSST V1, V4 and V9</b>                  Dedicated strain sensing cables                  PA outer sheath (structured for V9), without (V1) or with central metal armouring tube (V4 and V9)                  Diameter: 2.8mm (V1) and 3.2mm (V4 and V9)                  Price: +/-</p>	
<p><b>Solifos BRUsens LLK-BSST V0 and V3</b>                  Dedicated strain sensing cables                  HDPE (V0) and structured PA (V3) outer sheath with central metal tube, metallic armouring wires                  Diameter: 3.5mm (V0) and 7.2mm (V3)                  Price: +</p>	
<p><b>Solifos BRUsens LLK-BSTE/BSSA</b>                  Dedicated temperature sensing cable                  TPE or FRNC outer sheath (or without), fiber(s) inside stainless steel loose tube, additional stainless steel strength members                  Several cable designs up to 300°C                  Diameters of 3.4 to 4.8mm (2.8mm without PTE)                  Price: +-</p>	
<p><b>Solifos BRUsens DAS LLK-BSAC AC2/AC3</b>                  Dedicated acoustic sensing cable                  PA outer sheath, galvanized steel armouring and/or stainless steel strength members                  Diameter of 6.6mm (AC2) and 4.5mm (AC3)                  Price: ?</p>	
<p><b>NBG Single Layer (Perforated) FIMT, SonoSens, Stranded Double Layer FIMT</b>                  Dedicated acoustic sensing cable                  Fiber In Metal Tube (FIMT), without and with perforation. Also available with outer polymer layer (SonoSens) or as Stranded Double Layer FIMT for ultimate protection.                  Diameter: 1.1 – 7.0mm (FIMT), 2.3mm (perforated FIMT), 4.0mm (SonoSens), &gt;2.5mm (Stranded Double Layer FIMT)                  Price: ?</p>	

<p><b>NBG Harsh Environment Cable and Self-Supporting Downhole Cable</b>  Dedicated acoustic and temperature sensing cable  Cable designs allowing for very harsh environments, high temperatures and high pressures  Diameter: 6.35mm and 8.50mm  Price: ?</p>	
<p><b>Technica GFRP cable</b>  Dedicated strain sensing cable  GFRP coating on bare fiber  Diameter: 1.0-2.0mm  Price: +-</p>	

In addition to these specialized sensor cables, it is also an option to work with the raw or bare fiber, possibly with a limited, minimally protective coating. Some (D)OFS monitoring companies use their own in-house developed coating or protection techniques. For example, Com&Sens uses its own STRIP technology, converting a bare FBG fiber into a round or flat, robust, seawater resistant Fiber Sensing Rod (FSR, see Figure 43a). The cable is coated with PET or glass fiber reinforced plastic (mono-acrylate resin). The cable diameter can be adapted between 0.8 mm and 2.2 mm. At Buildwise, fibers are embedded in GFRP rods with a longitudinal notch. These rods consist of a polyester resin with E-Glass roving and have a diameter of 6 mm (Figure 43b and c). The longitudinal notch is both 2 mm wide and deep. It allows the integration of an optical fiber (whatever fiber type, as long as its dimensions fit in the notch) and converts the sensing fiber into a very robust sensor that can be prepared in laboratory conditions, transported on rather compact loops (about 1.5m diameter) and applied in harsh environments. Installation can even be done by the contractor without intervention or presence of the monitoring company. This is illustrated in Figure 43d, where the FBG sensors were integrated in a GFRP rod. A distributed sensing cable was attached to the GFRP rod as well. On site, the contractor installed the sensor cables in the 70m deep micropiles immediately after (or even during) the execution [21].



Figure 43. (a) The Fiber Sensing Rod as manufactured by Com&Sens with embedded FBG sensors. The fiber is coated with PET or glass fiber reinforced plastic (mono-acrylate resin). Diameters from 0.8 to 2.2 mm can be created. (b) GFRP rod (6 mm diameter) with a longitudinal notch (2mm deep and wide) as applied at the Buildwise. (c) The GFRP rod (6 mm diameter) with a GFRP coated fiber (1 mm diameter) in the longitudinal notch. (d) In field installation of the GFRP rod with integrated FBG sensors in a 70 m deep micropile.

Figure 44 shows an overview of fibers that have been tested by [19] for their concrete crack monitoring capabilities. This overview gives a good idea of the different cable dimensions. Most of the fibers in this table were also presented in Table 7 (or at least a similar fiber design).

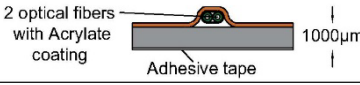
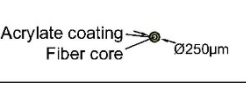
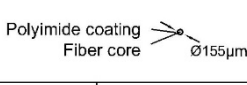
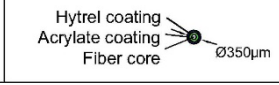
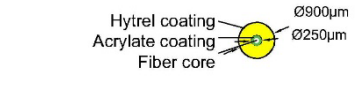
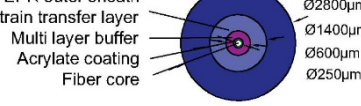
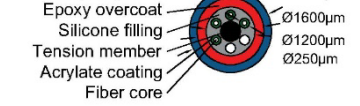
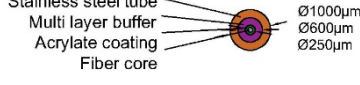
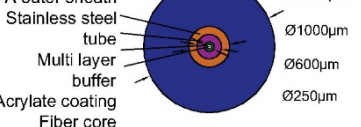
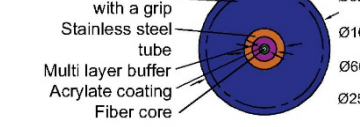
<p><b>FutureNeuro</b></p>  <p>2 optical fibers with Acrylate coating Adhesive tape 1000µm</p>	<p><b>Acrylate A1, A2</b></p>  <p>Acrylate coating Fiber core Ø250µm</p>	<p><b>Polyimide</b></p>  <p>Polyimide coating Fiber core Ø155µm</p>	<p><b>Hytrel</b></p>  <p>Hytrel coating Acrylate coating Fiber core Ø350µm</p>
<p><b>Thorlabs</b></p>  <p>Hytrel coating Acrylate coating Fiber core Ø900µm</p>	<p><b>BRUsens V1</b></p>  <p>EPR outer sheath Strain transfer layer Multi layer buffer Acrylate coating Fiber core Ø2800µm Ø1400µm Ø600µm Ø250µm</p>		<p><b>SensoLux</b></p>  <p>Hytrel jacket Epoxy overcoat Silicone filling Tension member Acrylate coating Fiber core Ø2000µm Ø1600µm Ø1200µm Ø250µm</p>
<p><b>Metal tube</b></p>  <p>Stainless steel tube Multi layer buffer Acrylate coating Fiber core Ø1000µm Ø600µm Ø250µm</p>	<p><b>BRUsens V4</b></p>  <p>PA outer sheath Stainless steel tube Multi layer buffer Acrylate coating Fiber core Ø3200µm Ø1000µm Ø600µm Ø250µm</p>	<p><b>BRUsens V9</b></p>  <p>PA outer sheath with a grip Stainless steel tube Multi layer buffer Acrylate coating Fiber core Ø3200µm Ø1000µm Ø600µm Ø250µm</p>	

Figure 44. Different types of tested fibers by Basil, et al. (2020), giving a good idea of the relative fiber dimensions.

### 3.3 Sensor architecture

An important part of a monitoring concept is the sensor architecture. This not only deals with the location of the sensors and sensor cables, but also how they are connected to each other and to the DAQ unit(s). It is good to keep the sensor architecture in mind from the beginning of the monitoring plan or concept in order to minimize cable lengths, maximize sensor redundancy, etc. Points of attention to bear in mind when defining the sensor architecture are listed below.

- **Redundancy:** if possible provide sufficient redundancy. Ways to achieve this are:
  - In case of FBGs or other multiplexable sensors, use an alternating sensor configuration, in which the sensors are distributed over several fibers (illustrated in Figure 46). In case of loss of 1 fiber, a full image of the structure can still be obtained (with a smaller sensor density). The number of sensor arrays (and required DAQ channels) can be optimized by using splitters or multiplexers.
  - Even if the measurement is single-ended (e.g. FBG, BOTDR, BOFDR, Rayleigh technology), still provide a return cable to the DAQ unit. In case of damage on 1 location of an FBG array, all sensors can be recovered by the return cable by simply switching the fiber connector (Figure 46a) or connecting both fibers to a splitter (Figure 46b).
  - Use 2 (or more) different sensing technologies. Comparison of both readings may resolve doubts about the correctness of sensor readings. Moreover, the cable types used by both technologies may be different and resist better to specific conditions. Of course, this requires an additional investment. In research or test applications it is often applied (e.g. if the success of the entire test campaign depends on the functioning of the sensors).
  - Use 2 (or more) cable types. If there is uncertainty about the best suitable cable or sensor type, one can choose to select 2 different cable types. Again, comparison of both readings may resolve doubts about the correctness of sensor readings.
  - Try to locate splices and connectors in an accessible position as much as possible.

- 
- Control the **optical losses** in the sensor array, as the use of connectors, splitters, multiplexed sensor arrays, etc. inevitably result in losses of the optical signal. Also note that connectors and splitters are more prone to long term degradation than splices, but very easy to use on site.
  - Consider the use of **multi-fiber cables** to cover larger distances and reduce cable cost (see Figure 27).
  - Avoid **sharp cable bends**. Sharp bends in the optical fibers increase the risk of cable damage during installation and execution. Where this is unavoidable, the fiber may be locally reinforced with a protective coating/tubing or e.g. a 3D printed piece. Sharp bends may also interfere with the measurements.
  - In the case of **double-ended measurements**, where both cable ends (and an intact fiber) are required to allow a measurement, there are several options:
    - o Use a cable with at least 2 integrated fibers. A loop at the end of the cable connects both fibers serially (Figure 47a).
    - o Realize the return to the DAQ with the same cable, whether or not by a different route on the structure. If the same route is followed, both measurements serve as a double check and may increase the measurement accuracy by averaging them. A different route may cover another part of the structure or element (Figure 47b).
    - o Realize the return to the DAQ with a temperature or other type of strain sensing cable. Both cables are then connected to each other at the fiber ends (Figure 47c).
  - **Less is more**. A general rule is to keep the monitoring plan as simple as possible. A careful choice has to be made beforehand of the most valuable measurement locations, the most suitable technology(s), the cable and/or sensor type(s), etc., bearing in mind the phenomenon to be measured. In this way the data quantity is reduced and the processing cost optimized.
  - (!) Don't forget **temperature compensation** if required.



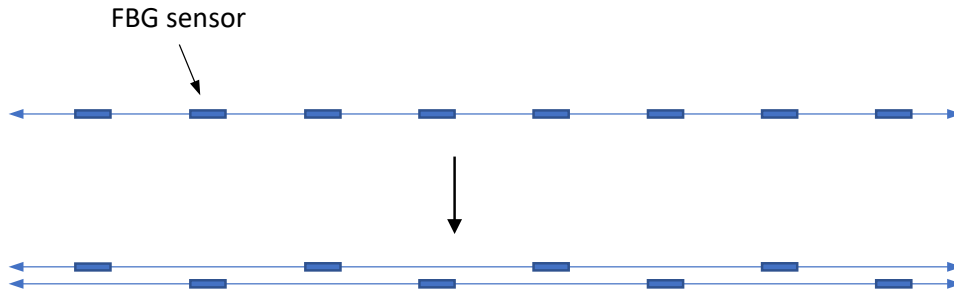


Figure 45. Increasing the redundancy of the sensing system by placing the FBGs on two separate lines with alternating sensors. If one array breaks, the entire structure is still monitored completely,

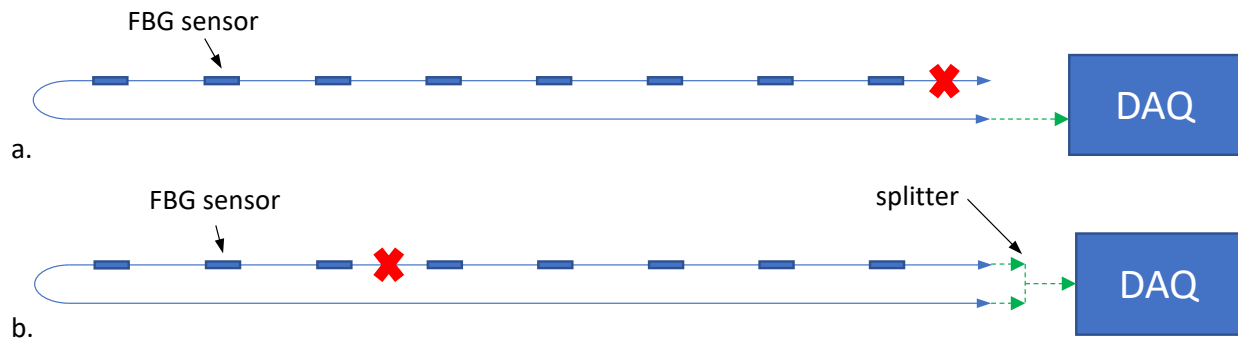


Figure 46. Illustration of how providing of a return cable can help to recover all multiplexed sensor after a cable breakage.

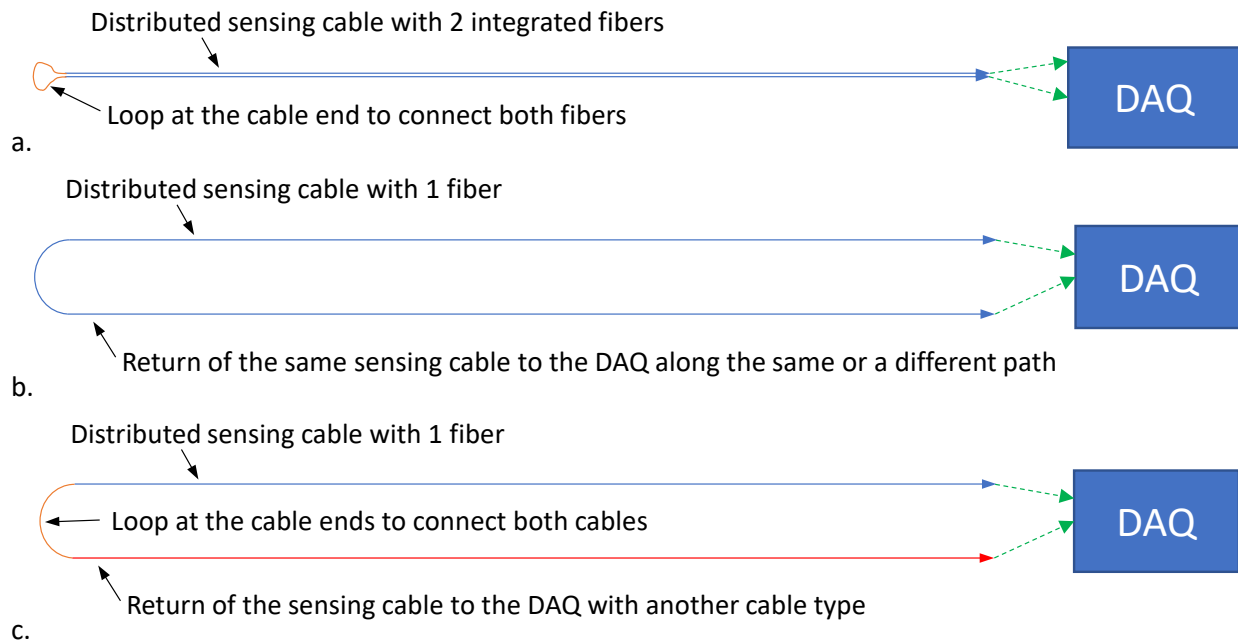


Figure 47. Illustrations of fiber architecture for double-ended distributed sensing. (a) Loop at the end of the cable to connect both integrated fibers. (b) Loop at the end of the structure or element, same or different return path. (c) Return sensing cable with another cable type, both fiber ends are connected by a loop.

### 3.4 Sensor mounting

As explained earlier in the info box at the end of Section 2.3 ‘OFS technologies: summary’, it is important to clearly define the purpose of the monitoring campaign and what parameters and phenomena must be monitored. This will determine the choice of sensor and/or sensor cable and the way they are mounted.

In this context, it is important to understand the difference between a local measurement and a measurement with a larger measurement base (extensometer principle), see Figure 48. When dealing with a homogeneous material or when interested in strain concentrations, local measurements are very useful. In heterogeneous material or when the global behaviour matters, measurements over a larger measurement base will be of more interest, as they are not (or less) influenced by local phenomena. Distributed FOS systems all have their own specifications in terms of spatial resolution and spatial accuracy. These parameters define how local a DFOS measurement is (see also Section 1.2 “Terminology” and Section 3.2.1.1 “Strain sensors and strain sensing cables”). During post-processing, the spatial accuracy can always be lowered to obtain a more averaged, global view. When dealing with (multi-)point sensing techniques, the sensing element often has a limited length (e.g., for FBG sensors typically about 10 mm). To obtain a larger measurement base, the sensor has to be released from its environment over the desired extensometer length and fixed at both ends to the structure or element (anchorage points). This is illustrated in Figure 48.

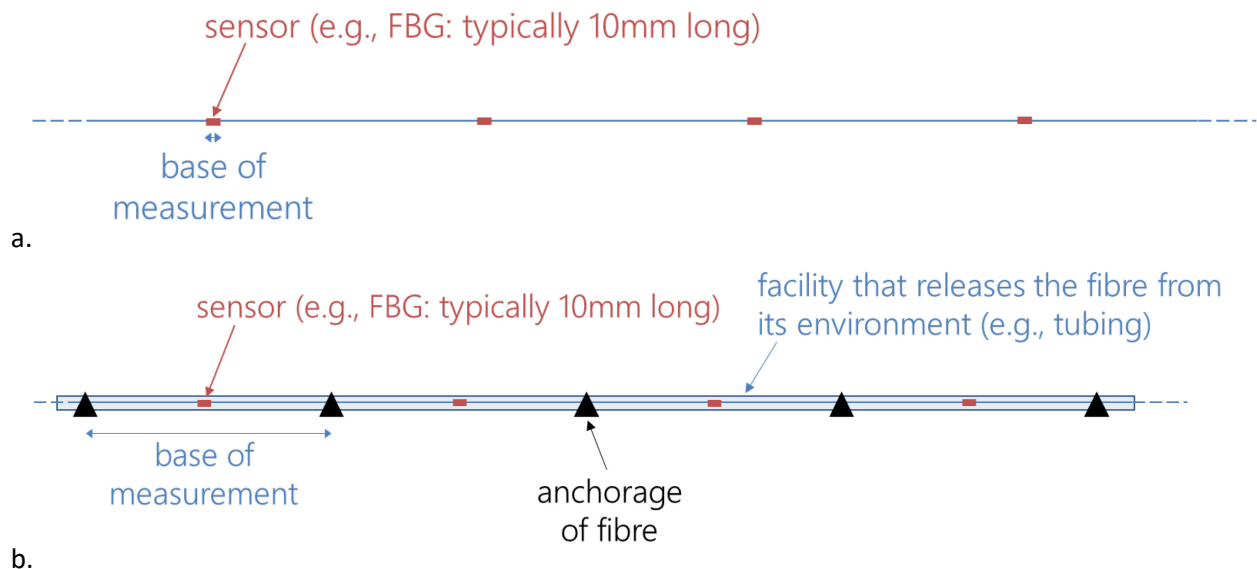


Figure 48. Schematic representation of the difference between a local measurement (a) and an extensometer measurement over a larger base of measurement (b).

When installing sensors or sensor cables, one should also keep in mind the expected monitoring duration and the environmental and operational conditions to which the sensors or sensor cables are subjected. The cable types, sensors and mounting solution should be adapted to these conditions.

Sensors and sensor cables can be integrated in or mounted on the structure or element in a variety of ways, e.g.:

- Mechanically, on the surface of the structure or element (concrete, steel, wood, bricks, FRP, geotextiles, ...). Often installed as extensometer (Figure 49).
- Chemically, e.g., glued on the surface of the material. In the case of multi-point sensing techniques, the sensor might be glued locally or as extensometer (Figure 50). In the case of distributed sensing techniques, the sensing cable is mostly glued over its entire length.
- By welding or spot welding. Weldable sensors are commercially available.
- Integrated in the structure or element:
  - o Attached to e.g. the reinforcement bars and poured directly in concrete, FRP, grout (local measurement or extensometer), see Figure 51 for some examples.
  - o Grouted in a reservation tube, installed via support system/carrier (local or extensometer), see Figure 52 for some examples.



Figure 49. Examples of mechanical fixation of sensing fibers.



Figure 50. Examples of chemical fixation of sensing fibers. In the example of picture (a), the fiber will be glued inside the groove, which offers an additional protection.



Figure 51. Examples of integration of the fiber optic cables directly in the structure. In all these cases, the fibers are attached to the reinforcement cage of the concrete beam (a), of the diaphragm wall (b) and of the foundation pile (c).

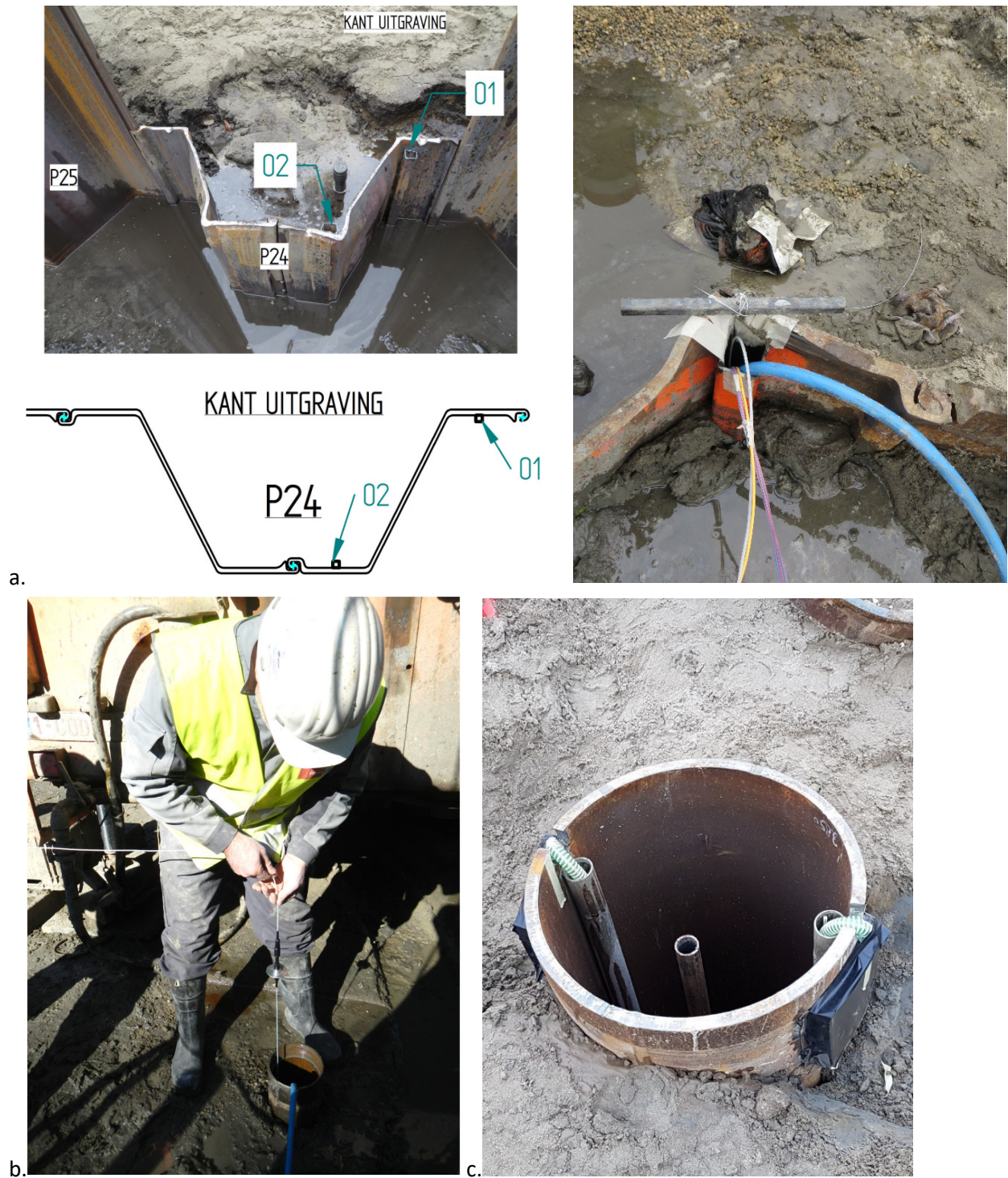


Figure 52. Examples of the integration of the optical fibers in a reservation tube in which the fiber is installed and fixed with a grout. (a) Sheet piles, (b) a borehole and (c) a foundation pile. After installation of the structure, the optical fibers are installed in the reservation tube at the desired position and subsequently fixed by injecting e.g. a grout mixture (i.e., water cement mix).

---

## 4 (Infra)structure monitoring applications

### 4.1 Application areas

As described before, the main advantages of (distributed) optical fiber sensing are its high sensitivity over large distances and the ability to interface with a wide range of measurands by multiple multiplexed sensors or in a distributed manner [13]. The systems provide tens to thousands of “strain gauges”, “thermo-couples” and/or “accelerometers” along a single fiber optic cable connected to or embedded in structures, which can then serve as a nerve system of the structure. It can be applied to flexible geometries, providing the ability to design a whole range of sensors with tremendous information carrying capacity. They can be used under adverse environmental conditions; they are intrinsically immune to electromagnetic interference, high-voltage environments, nuclear radiation, corrosion, and other harsh environmental conditions.

It is obvious that these characteristics offer an enormous potential for monitoring in a wide range of applications with enhanced performance in comparison to traditional sensing technologies. In this document these applications are subdivided in 4 categories. Note that some applications might fit in more than one category.

#### 4.1.1 Innovative systems

An innovative system can be either an innovative execution technique to construct certain structures or innovative structures/elements themselves. Optical fiber sensing can help to characterize the innovative system very accurately. It may lead to a detailed and/or global view on the functioning/performance of the system/interaction with surroundings and to enhanced insights. In turn, this may lead to a further improvement of the performance of the technique, structure, element or detailing. Some illustrative cases are presented in Section 5.1.

#### 4.1.2 Proof testing

Also during traditional proof testing, optical fiber sensing can be a great added value. Again, the optical fiber sensors can deliver very extensive, additional insights in the functioning of the tested system and can for example lead to the determination of more accurate design factors, provide a check of adopted design principles or help to evaluate correct production and/or installation. In Section 5.2, some example cases are presented.

#### 4.1.3 Long term monitoring of existing and new infrastructure

Structural health monitoring (SHM) of infrastructure has become significantly more important within the last decades due to the rapidly growing construction volume worldwide as well as the aging of infrastructure and a trend to safely and cost-effectively extend the service lifetime of structures [6]. This methodology fits in the evolution of a preventive maintenance approach towards predictive maintenance. In the latter case, maintenance costs and/or impact are minimized by performing maintenance only when needed or by realizing smaller interventions in order to drastically reduce downtime. In this context, continuous monitoring of structures provides a better view on the global behaviour. This can help to better localize damaged and/or degraded areas which need more attention, local evaluation or repair. Again, this will lead to less downtime and less extensive periodic inspections (in particular for hidden or less accessible structures, as is the case for instance for tunnels with fire protection shielding). SHM may also apply to monitor the influence of (temporary) neighbouring works on the structure. Apart from SHM,

---

the insights obtained from long term monitoring can also lead to optimized design parameters for certain structures.

Long term monitoring is currently already applied on bridges (steel, concrete, composite, ...), tunnels, embankments, dikes, soil reinforcements and slopes (detection of ground movements and landslides), retaining walls and foundation piles, (submarine) cables and pipelines, reinforced concrete structures (crack detection and corrosion monitoring), railway monitoring, et cetera.

Obviously, the possibilities of optical fiber sensing can be exploited in this application area. Moreover, there is a large demand for sensing solutions and tools in harsh environments, often with limited accessibility (radiation, high temperature, chemical aggression, below water level, ...), with a need for large area coverage or a dense sensor network, et cetera. A range of cases is illustrated in Section 5.3.

Note that for long term applications an autonomous monitoring system should be installed. A real-time (online) dashboard where the measurements can be accessed at any time, has a significant investment cost but allows quick and better insight into the measurements and will save a lot of time in the long term. For specific applications, more enhanced analysis and interpretation might be necessary to fully exploit the monitoring system, e.g., for structural health monitoring (SHM). Based on strain and/or temperature evolution only it is often easy to detect anomalies in an early stage. Moreover, their evolution might be influenced by external factors (e.g., temperature, wind, rain, loading conditions, ...). To automatically interpret this monitoring data, it is appropriate to provide advanced analysis (based on Machine Learning techniques or operational modal analysis, see also section 4.2 about 'Interpretation methods').

#### 4.1.4 Quality control of invisible structural elements

A last application area is about quality control of invisible structural elements or execution techniques. Possible applications are, amongst others:

- Post-injection control (foundation elements, etc.)
- Grout filling
- (Thermal) integrity profiling (e.g., pile foundations, diaphragm walls, basement walls – see also the cases in Sections 5.1.2, 5.4.2 and 5.4.3)
- Concrete cover detection (see also [22])
- Tunnel walls
- Groundwater leakage in retaining walls

## 4.2 Interpretation methods

In the civil, railway, energy, and other industries, the monitoring of the operational behaviour of structures and the timely identification of structural deterioration are prime concerns. Deterioration and damage might appear due to a multitude of possible causes, such as the exceedance of the design life, faults in the design, construction errors, inadequate maintenance, exposure to unforeseen structural and environmental loading, or to extreme events such as earthquakes. Structural Health Monitoring (SHM) systems are therefore deployed on an increasing number of structures such as bridges, dams, tunnels and wind turbines. They enable to detect modifications in the behaviour and response of structures with respect to the baseline condition at the time of installation of the monitoring system. Thus, an early installed SHM system increases the chances of damage identification at any moment of the structure's service life. For this reason, smart structures are being built where SHM systems are deployed also during construction. Bridges where SHM systems are currently deployed are the Infante D. Henrique bridge in



---

Portugal [23], the Rion-Antirion bridge in Greece [24], the KW51 bridge in Belgium [25, 26], the Tsing-Ma bridge in China [27], to name just a few characteristic examples.

Among the multitude of existing methods for SHM, visual inspection is the most widely used method but it is a slow and subjective procedure that can only detect damage that manifests itself at the surface of an accessible part of the structure. For potential damage locations at or near the surface, local non-destructive damage detection techniques such as acoustic or ultrasonic methods, magnetic fields and radiography can be employed. Vibration-Based Monitoring or VBM is a global monitoring method [28]. It is based on the relation between the stiffness, mass and energy dissipation of a structure and its dynamic behaviour, which is entirely determined by the modal characteristics: natural frequencies, damping ratios and mode shapes. The idea behind VBM is to identify changes in modal characteristics of a structure that are directly related to damage. The main challenge for VBM is to identify characteristics that are as sensitive as possible to structural damage and at the same time as insensitive as possible to measurement noise, loading, and environmental factors such as temperature.

In order to extract the modal characteristics of a structure, its vibration response to a dynamic excitation force (known and/or unknown) needs to be measured first. The sensors that are most often used in practice are piezoelectric accelerometers. The introduction of fiber-optic sensors (FOS) that can accurately measure dynamic strains and offer ease of installation, resistance in harsh environment, electromagnetic immunity, long-term stability and relatively low cost when compared with accelerometers, contributed to an increased interest in adopting these sensors for VBM applications [29]. The measured response can be used then for system identification and modal analysis. When both the input force and the output response are known, the modal characteristics identification process is called experimental modal analysis (EMA). If only the output response is known, the modal characteristics identification process is called operational modal analysis (OMA) and is the method that is primarily used in large civil structures [30]. Several methods have been developed and successfully implemented for fully-automated (operational) modal identification [23, 25].

The identified modal characteristics can be subsequently used for structural health monitoring and damage identification purposes. VBM methods can be classified in model-based or response-based methods [28]. In model-based methods, a detailed numerical model of the structure is required for damage identification. With this model, different damage scenarios can be simulated and their influence on modal characteristics can be investigated. Damage can be identified by comparing measured modal characteristics with the ones observed in the numerical model due to the simulated damage. Response-based methods are using exclusively experimental data to train damage identification algorithms and can be further classified into supervised and unsupervised learning methods [28]. Unsupervised methods are using data that are obtained from the undamaged structure and their diagnostic capability is limited in detecting and occasionally in localizing damage. Supervised methods on the other hand require the existence of experimental data measured in the damaged state of a structure but their diagnostic capability can potentially go up to damage quantification.

Natural frequencies can be obtained from only one or a few sensors, e.g. accelerometers, placed at proper locations. As a result, they are very often used for VBM. Natural frequencies are very sensitive to global stiffness modifications but not so much to local ones. Therefore, local damage of small or moderate severity has a rather small influence on natural frequencies, while the global stiffness is often influenced by variations in environmental factors such as temperature. That influence can be high enough to

---

completely mask the presence of even severe local damage, necessitating data normalization to remove it. Displacement mode shapes can also be used for damage identification purposes. They are attractive in the sense that they are more sensitive to local stiffness changes than natural frequencies, and less sensitive to temperature variations. The main disadvantage is that a dense sensor grid is required for good damage localization capabilities, which is generally cumbersome when conventional sensors, such as accelerometers, are employed.

Strain mode shapes are an attractive alternative for the conventional displacement mode shapes, because modal strains and strain-based features are much more sensitive to local damage than modal displacements, and dense sensor grids can be achieved at relatively low cost, thanks also to the multiplexing capacity of some FOS types such as fiber-Bragg gratings (FBG). The main challenge has been that the dynamic strains that occur in large civil structures in operational conditions are very small, typically in the sub-microstrain range. However, recent experiments involving FBG sensors have demonstrated that with improved sensor interrogation [25] or signal processing techniques [31], the required sensing accuracy can be attained. Laboratory experiments on concrete beams, steel beams and steel pipes have illustrated that modal strains are highly sensitive to local damage of low or moderate severity, while they can be insensitive to global temperature changes [32]. Recent work has also confirmed this temperature insensitivity for the case of a 120 m steel bridge (see Figure 98 in Section 5.3.2) whose modal strains were continuously monitored for one year [25], while also confirmed the high sensitivity of strain mode shapes to small-scale and local damage [33]. More examples of successful implementation of the strain mode shape-VBM method are briefly discussed in the following sections.

### 4.3 Validation testing

In order to evaluate the performance of optical fibers for the monitoring of concrete structures, several validation tests have been performed by Buildwise at different levels. Different optical fiber setups and types were hereby evaluated in a real reinforced concrete environment (see Section 4.3.1 for static behaviour and Section 4.3.2 for dynamic behaviour). In addition, special attention was paid to concrete-specific damage phenomena, in particular, the ability of optical fibers to detect crack formation and corrosion (see Section 4.3.3 and Section 4.3.4 respectively).

#### 4.3.1 Static behaviour of a concrete beam at different cracking degrees

A concrete beam was equipped with a wide range of fiber optics. The optical fibers were both installed on the reinforcements in the concrete as well as mounted on the concrete surface. A schematic overview of the embedded optical fibers and their setup is shown in Figure 53.

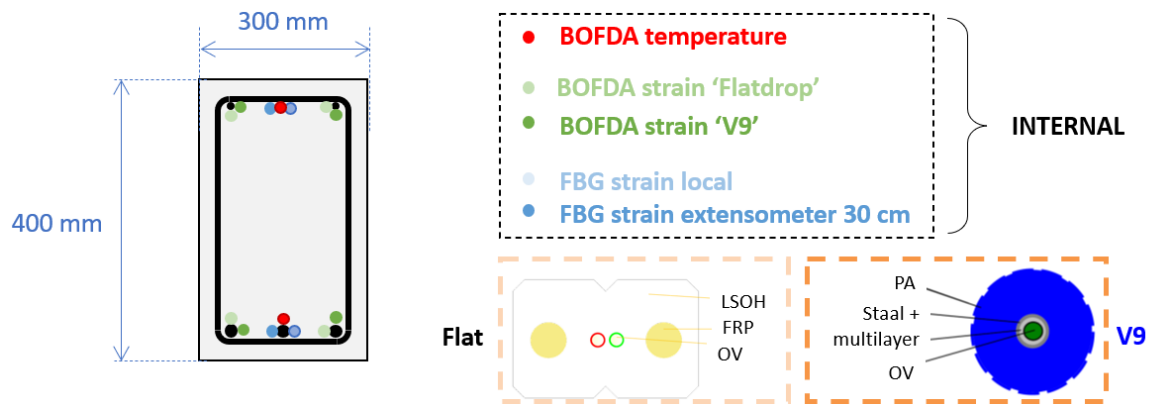


Figure 53. Schematic representation of the built-in optical fiber sensor cables.

In the 4 corners of the beam section, 2 types of BOFDA optical fibers were installed: a Fibrain flat drop cable and a Solifos V9 cable (see Table 7). Centrally, at the top and bottom of the section of the concrete beam, two FBG arrays were installed as well as a BOFDA temperature sensing cable (see Figure 54). For the FBG arrays, the optical fibers were glued onto a GFRP rod in order to achieve a more robust arrangement that withstands pouring of the concrete (see Figure 43b-d). For one of these two FBG arrays, tubes of about 300 mm length were fitted around the GFRP rod, specifically at the locations of the FBG sensors (which are spaced 500 mm apart on the optical fiber). This construction was selected for testing, in order to evaluate whether the GFRP rod could be locally decoupled from the concrete, to achieve a semi-extensometer setup (see bottom right picture in Figure 54).

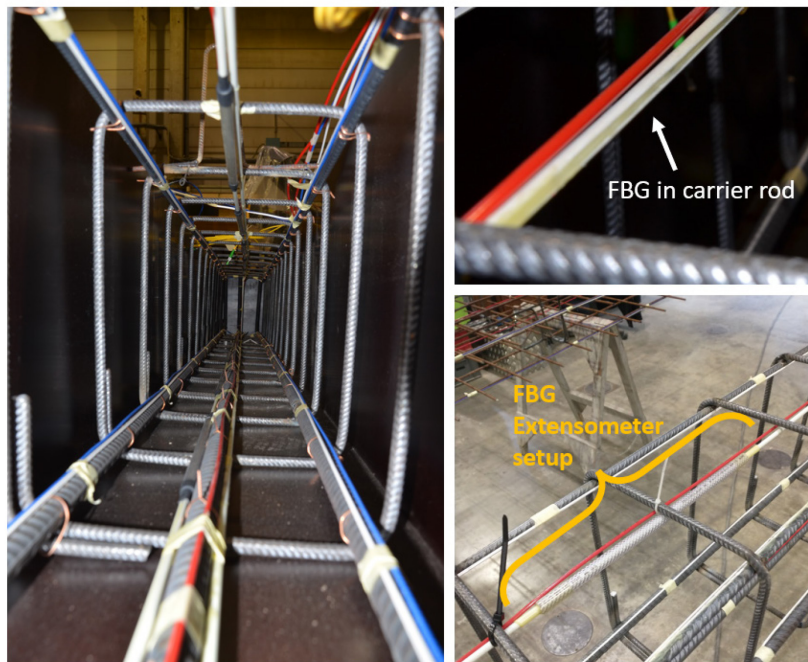
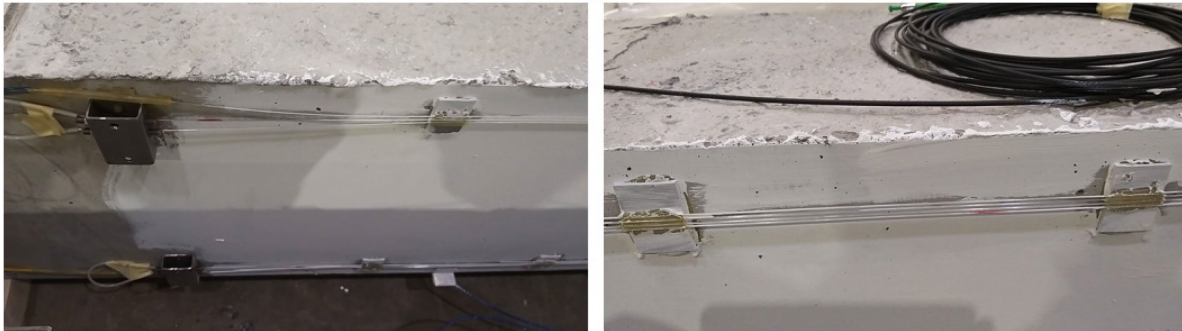


Figure 54. Pictures of the embedded optical fiber sensing cables, with a detail of the FBG array embedded in a GFRP rod at the top right and a detail of the FBG extensometer setup at the bottom right.

At the outer surface of the concrete beam, 4 FBG arrays were attached to the concrete surface, at the top and the bottom of the surface (at the level of the longitudinal reinforcement bars), and this at the front and at the rear of the beam. These FBG arrays are glued to the concrete surface by means of mounting blocks (see Figure 55 (right)). Devices are positioned at one end of the beam in order to provide a certain degree of pre-stressing to the sensing arrays (see Figure 55 (left)). The mounting blocks are located centrally between the FBG sensor locations. At the front and rear of the beam, the FBG sensors are positioned at an interval of 250 and 500 mm, respectively.



*Figure 55. Photographs of the optical fiber measurement lines mounted on the concrete surface, (left) prestressing device at the end of the beam, (right) extensometer attachment using glued mounting blocks.*

The beam was subjected to a 4-point bending test. It was gradually loaded with load steps of 50 kN, progressively introducing damage in the beam. Upon reaching each load level, the displacement of the hydraulic jack (or the deflection of the beam) was kept constant (so the applied load decreased during each load step). Each load step was maintained at least a few minutes in order to collect at least 2 BOFDA measurements. After each load step, the beam was fully unloaded to perform a dynamic measurement (see next Section 4.3.2). Subsequently, the beam was loaded again to the next load level. In Figure 56, the load and deflection curve can be found as a function of time.

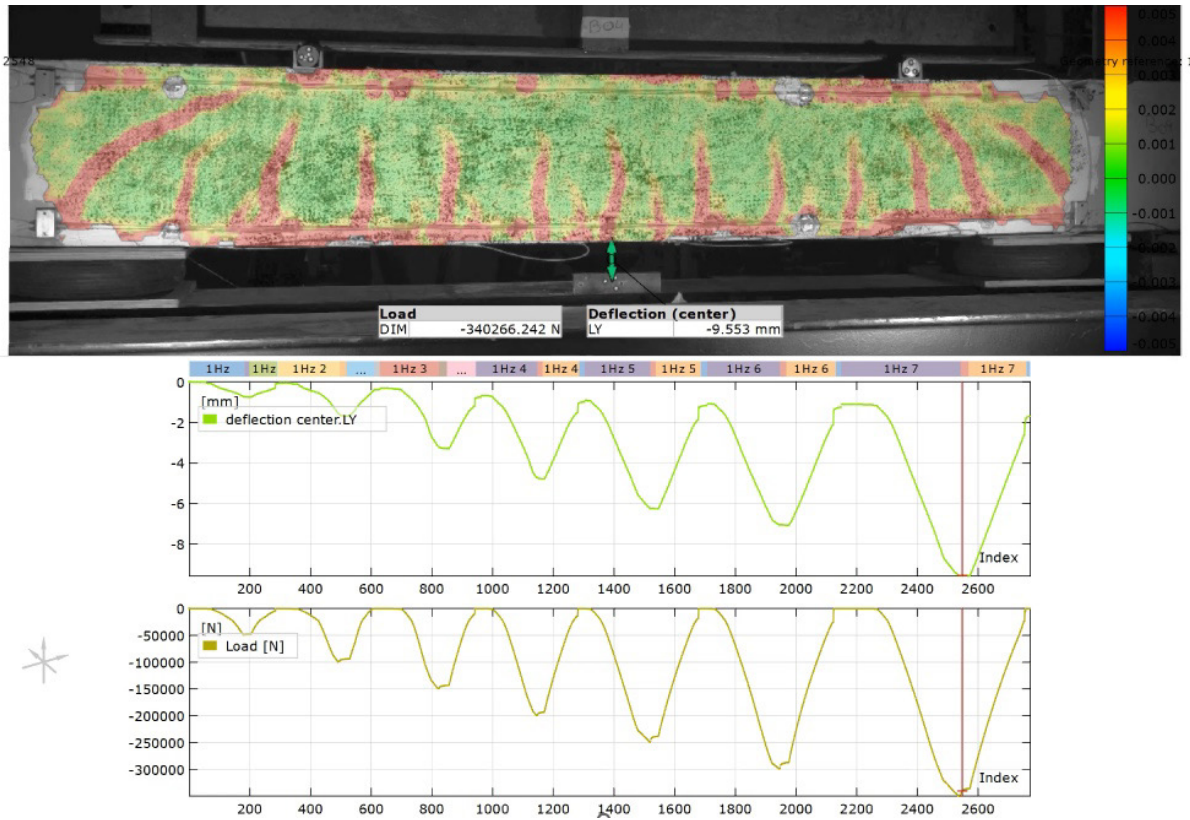


Figure 56. (Below) Load and deflection registered during the experiment in function of time. (Above) The strain profile obtained with the Digital Image Correlation (DIC) during the last load step (at 350 kN).

The static optical fiber measurements were compared with Digital Image Correlation (DIC) measurements conducted on the front surface of the beam. For this purpose, the concrete surface between the 2 point loads was coated with a black and white speckle pattern. Two high-definition cameras take pictures of the speckle pattern at a selected time interval. Movements and deformations of the unique pattern of black speckles are monitored and post-processed with the supplied software package into full-field 3D strains. The strain profile obtained with the DIC during the last load step (at 350 kN) is illustrated in Figure 56 (above). The red areas indicate the locations of the various bending cracks.

A very good agreement is observed between the results of the external FBGs with a measurement base of 250 and 500 mm (see Figure 57). Moreover, both FBG arrays show the same overall trend as those obtained with the DIC. At higher loading levels, the FBG measurements sometimes locally deviate at the lower (tensile) side of the beam. However, upon further analysis, it was seen that these deviating values correspond to areas where smaller bending cracks are present which are more difficult to identify with the DIC due to visual interferences created by the external FBG lines.

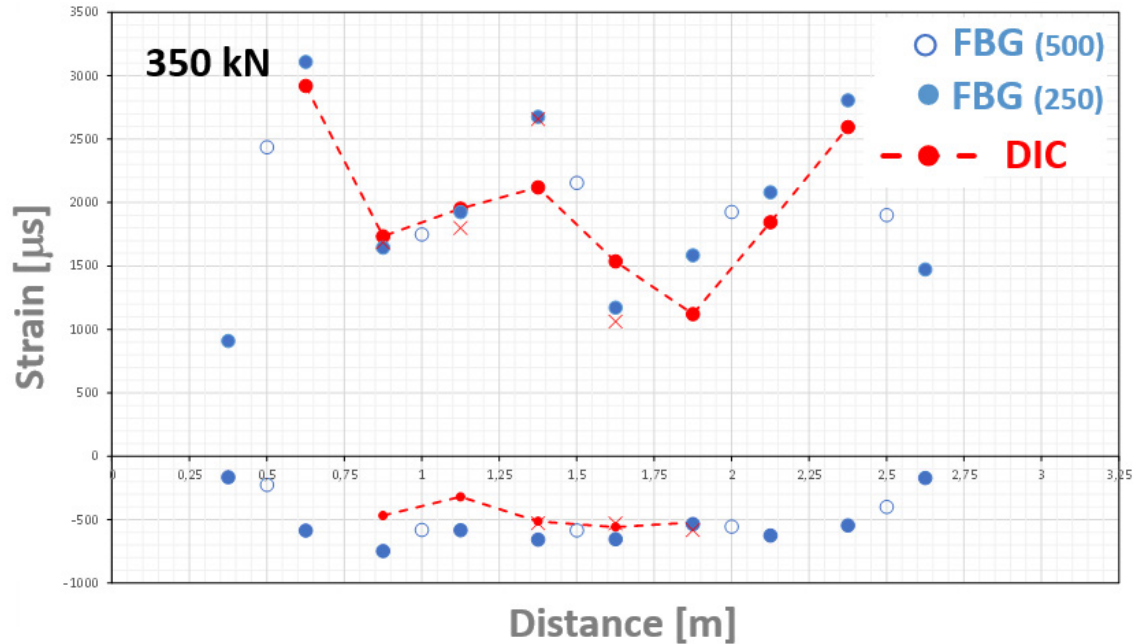


Figure 57. Results of FBGs mounted on the surface with extensometer length of 250 and 500 mm compared with equivalent DIC measurements (load step = 350 kN). Positive sign = tension.

The FBGs installed in the centre of the beam in semi-extensometer setup (inside the concrete) also present a good agreement with the DIC measurements and the external FBG sensors (see Figure 58). The setup with the tubing (see bottom right picture in Figure 54) was proven to act as an extensometer and is a very promising and cost-effective technique for internal monitoring of concrete structures.

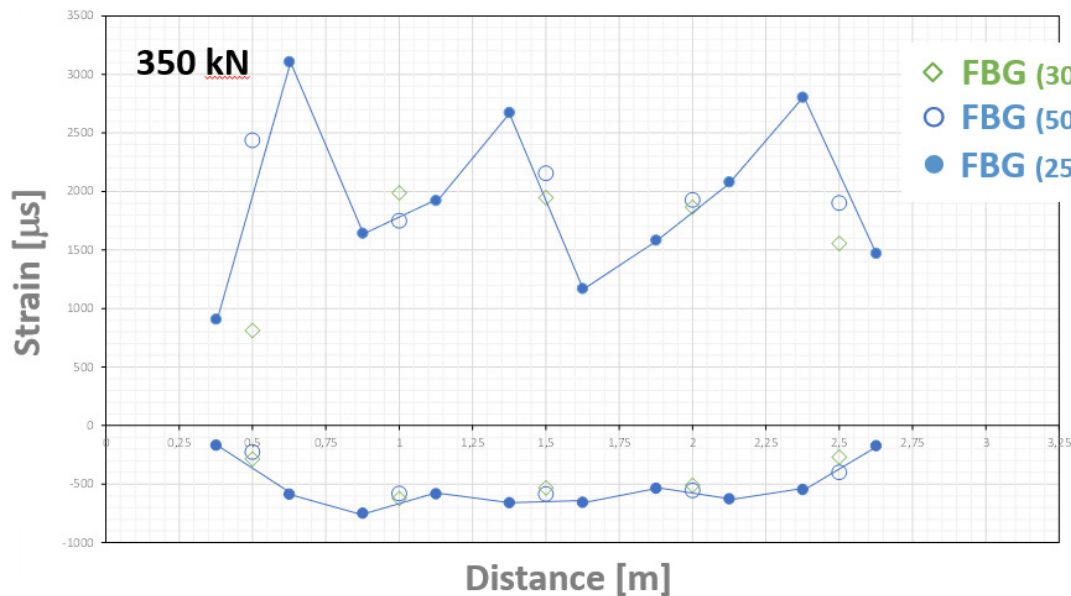


Figure 58. Results of surface mounted FBGs with an extensometer length of 250 and 500 mm, compared the FBG sensors installed as a semi-extensometer (300 mm length) inside the concrete beam (load step = 350 kN). Positive sign = tension.

The FBG array which was solely glued into the carrier rod (without tubing) resulted in very local strain measurements. Despite of its smooth surface, the carrier rod adhered well to the concrete and consequently did not cause excessive smearing of the measuring zone of the FBG. This setup is thus less appropriate for internal monitoring of concrete structures, as the measurement is strongly influenced by local phenomena.

Early on in the analysis of the BOFDA measurements, it was clear that these results are much more complex to interpret. The utilised BOFDA measuring equipment provides measurement values every 50 mm along the optical fiber sensing cable. Initially, these values were compared with the DIC measurements. In Figure 59a, it can be seen that the raw BOFDA measurements differ significantly. The BOFDA sensing system is clearly not able to detect the individual cracks, probably due to the dense crack pattern with a limited spacing between the cracks. In a subsequent processing step, the BOFDA data was assumed to provide a more smeared strain measurement. To that extend, the DIC measurement values obtained at an interval of 50 mm were averaged over various distances ranging from 200 mm to 500 mm (see Figure 59b to d). The BOFDA measurements seem to show a better agreement with these averaged DIC strains. It is however difficult to state what the averaging of the BOFDA system is, and this might also differ from system to system, from cable type to cable type, ...

Note that similar tests have been performed at several research institutes worldwide, e.g., [6] and [20].

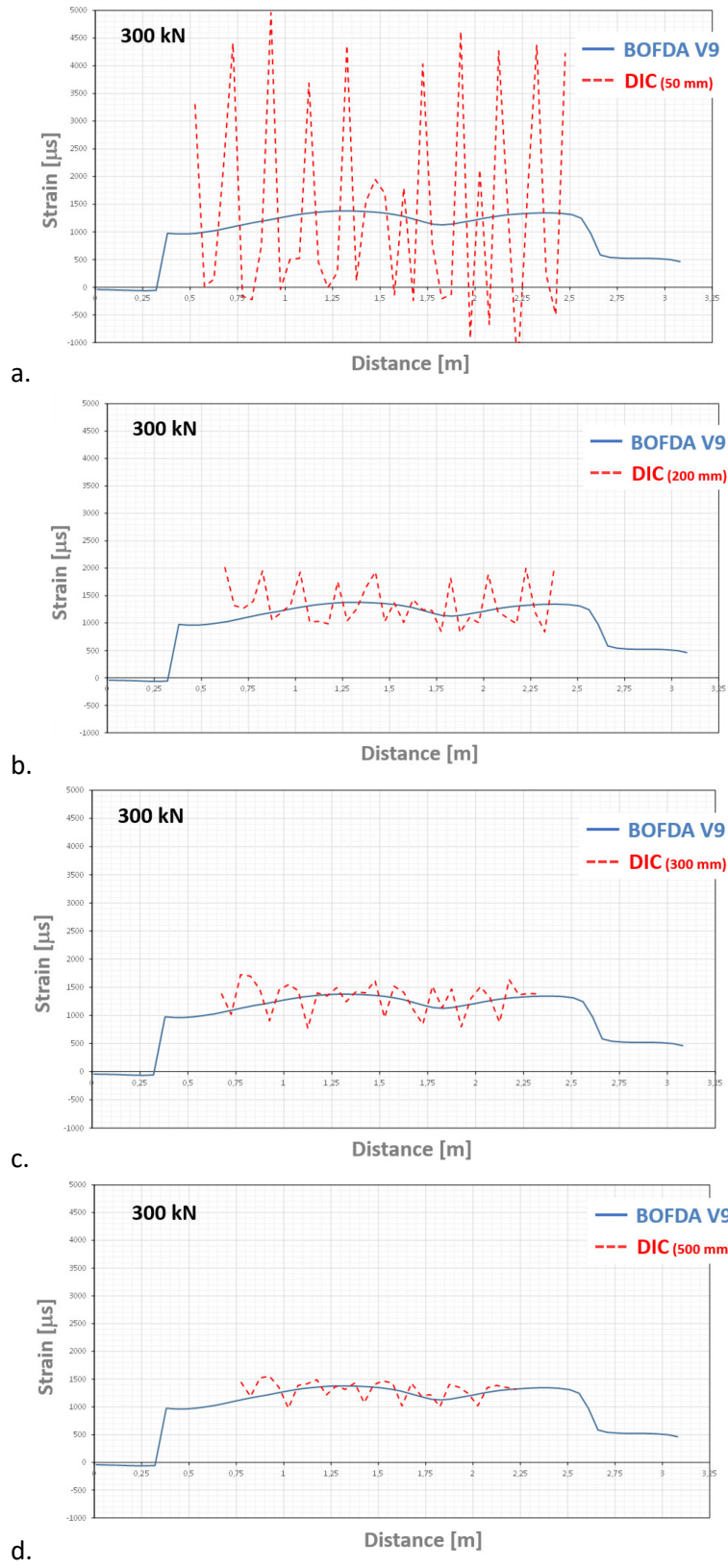


Figure 59. Results of BOFDA V9 installed in the concrete at the bottom on the front side compared with DIC measurements with a measurement base of 50 mm averaged over 0, 200, 300 and 500 mm.



#### 4.3.2 Dynamic behaviour of a concrete beam at different cracking degrees

In addition to the study of the static behaviour of the concrete beam as described in Section 4.3.1, the dynamic behaviour of the beam was studied as well. Before starting the progressive damage test and after each unloading phase, the beam was subjected to dynamic tests so as to identify its modal characteristics, i.e., natural frequencies and strain mode shapes, which represent the state of the beam after each loading step. For the dynamic tests, the beam was placed on flexible supports, i.e., two inflated tires (Figure 60). They act as vibration isolators, such that uncertainty in the boundary conditions due to interaction with the supporting laboratory structure is avoided as much as possible. The dynamic free-free boundary conditions that are introduced in this way after each loading cycle, ensure that all changes in modal characteristics will only be damage-related.

The dynamic excitation of the beam was performed with the use of impulse hammer impacts. The developed dynamic strains were measured only with the external FBG chains that were attached to two sides of the beam.

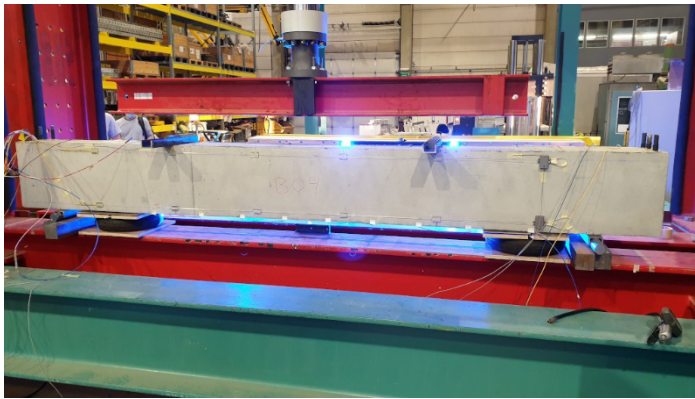


Figure 60. The experimental setup of the B04 beam during the dynamic tests: the beam is put on 2 inflated tires.

The dynamic strain data that are obtained from the FBG sensors are used for identifying the modal characteristics of the beam. Four beam modes are identified for the undamaged beam and after each loading cycle: the first and the second vertical bending mode and the first and the second lateral bending mode (Figure 61). The influence of damage on the modal characteristics is investigated next.

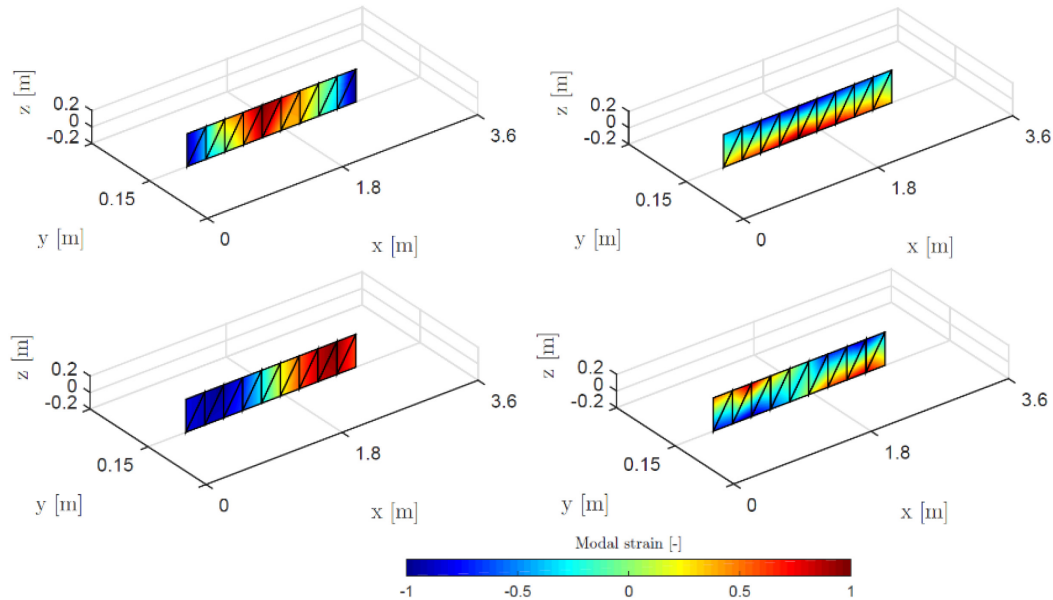


Figure 61. Strain mode shapes of the first four modes of the B04 beam (undamaged beam). Top left: first lateral bending mode (L1),  $f=88.3$  Hz. Top right: first vertical bending mode (B1),  $f=117.1$  Hz. Bottom left: second lateral bending mode (L2),  $f=236.2$  Hz. Bottom right: second vertical bending mode (B2),  $f=301.8$  Hz.

The evolution of the natural frequencies of the first four bending modes throughout the progressive damage test is displayed in Figure 62. The natural frequencies gradually decrease with increasing level of damage. The maximum relative reduction of the natural frequency values is about 12% for all modes, at the end of the final loading cycle (loading amplitude of 350 kN), showing a clear influence of damage on natural frequencies. It is interesting to notice that even after the first loading cycle, when the cracking load for macro-cracks of the concrete was not exceeded, a relative reduction of about 1% was already observed on the natural frequencies due to the formation of the first micro-cracks in the concrete matrix.

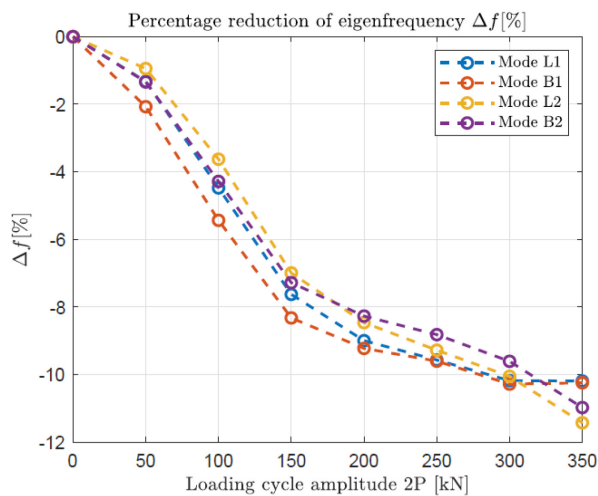


Figure 62. Relative eigenfrequency difference of the four identified modes of the B04 beam for the different steps of the progressive damage test.

A clear influence of the damage on the strain mode shapes of the identified modes can be observed, already after the first loading cycle. As a representative example, the strain mode shape of mode B1 is given in Figure 63, as obtained from the side of the beam that is equipped with 10 FBG sensors (5 at the top and 5 at the bottom). A clear reduction of the modal strain amplitude at the top and an increase at the bottom is observed as the PDT progresses. This behaviour can be explained by the type of damage (bending cracks) that is introduced in the beam, which results in a redistribution of the strains in the beam and a corresponding shift of its neutral axis towards the undamaged zone [32]. This shift of the neutral axis can be also quantified (Figure 64), based on the identified strain mode shapes [32].

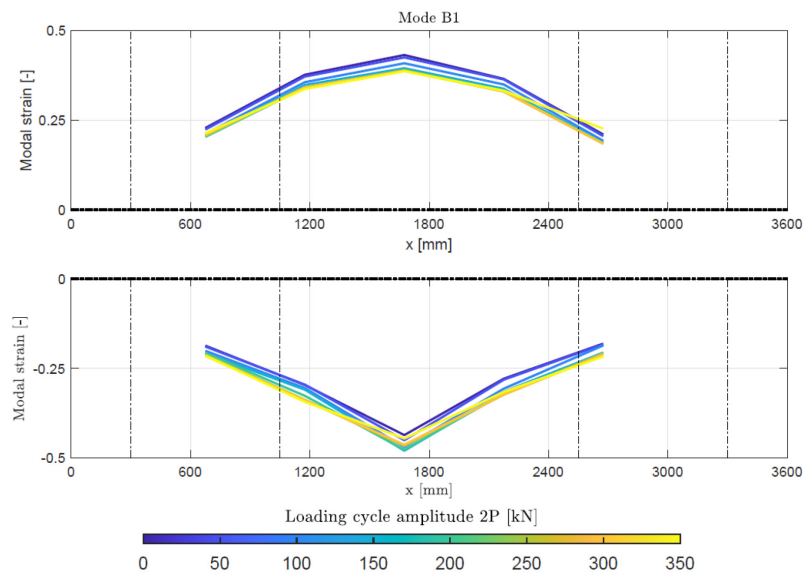


Figure 63. Strain mode shapes that have been identified after each loading-unloading cycle of the progressive damage test for mode B1. The top and bottom subplots contain the strains at the top and bottom of the beam respectively.

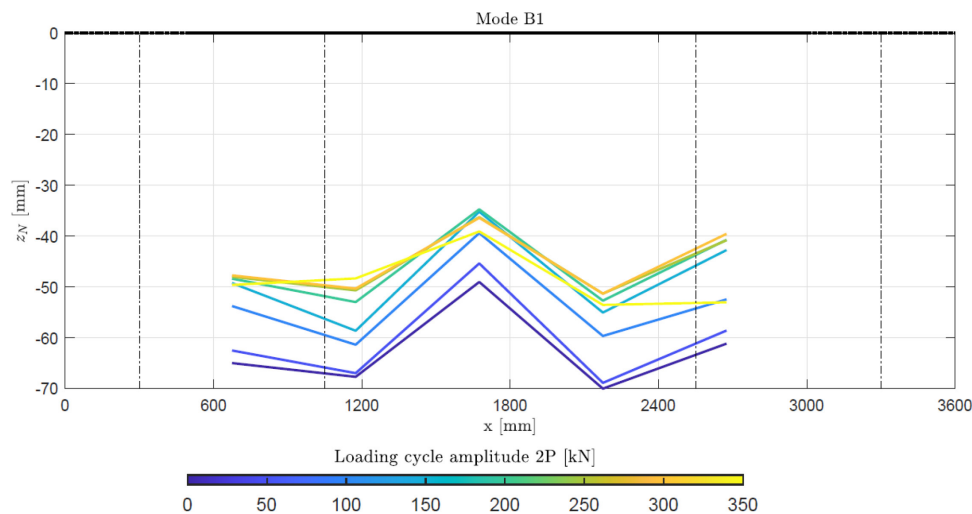


Figure 64. Neutral axis positions ( $z_N$ ) that have been identified after each loading-unloading cycle of the progressive damage test from mode B1, with respect to the centre of gravity of the beam ( $z_N=0$  mm).

### 4.3.3 Concrete crack monitoring

An additional set of validation experiments was performed by Buildwise to evaluate the potential of the BOFDA sensing system (FibrisTerre fTB5020 DAQ unit) for crack formation detection. For this purpose, steel fiber reinforced concrete (FRC) beams were made (dimensions: 150 x 150 x 900 mm<sup>3</sup>). A notch of 25 mm was sawn in their mid-span (see Figures 65 and 66). Two types of BOFDA sensing fibers were poured in these beams (Fibrain Flatdrop and Solifos V9, see Table 7), positioned at two heights above the saw cut (see Figure 65).

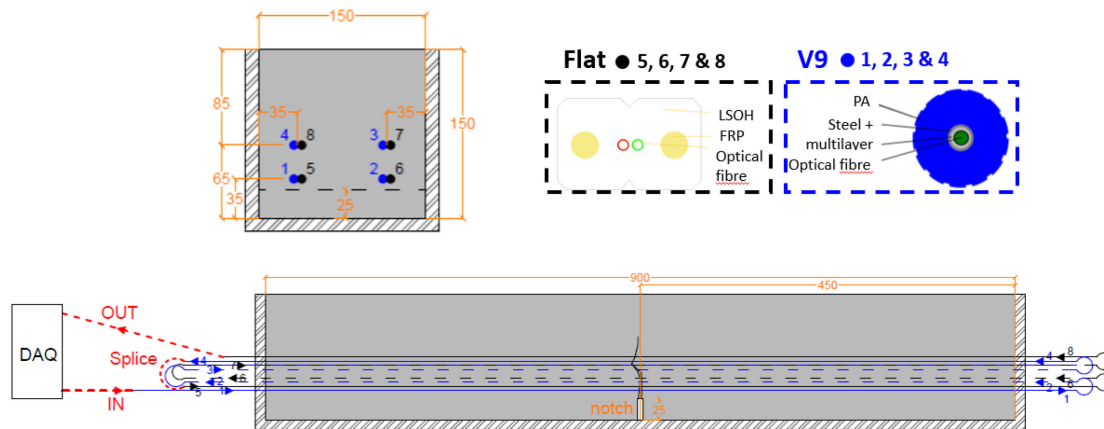


Figure 65. Optical fiber setup in the FRC beams.

These FRC beams were subjected to a 4-point bending test. Due to the presence of a local weakened section, one crack develops above the notch during the test. During the experiment the displacement of the jack was stopped at different time intervals to enable a BOFDA measurement. On one side of the specimen, crack development and, in particular, crack width evolution at the level of the BOFDA sensing cables were also monitored using Digital Image Correlation (DIC).



Figure 66. The experimental setup for the crack formation detection.

In Figure 67, the results of the Solifos V9 sensing cables are presented. Up to load step 7, a smooth evolution of the strains along the length of the beam can be observed (i.e., up to a crack width of 1 mm). A wave-like reading is obtained with a peak strain at more or less mid span, where the crack occurs. From step 8 onwards, sudden jumps are observed in the measurements, possibly indicating that the optical fiber is damaged in some way. Up to a crack width of about 1 mm (step 7), a fairly good linear regression ( $R^2$  of 0.97) was observed between the peak strains of the Solifos V9 sensing cable and the crack width registered with the DIC (illustrated in

Figure 68). When the data of the 2 sensing cables (the one at the bottom of the beam (s1) and the one at mid height (s2)) are combined, a regression coefficient of 0.0036 is obtained (see Figure 69 (right)). The intercept with the horizontal axis is situated around  $\pm 80 \mu\text{strain}$ , which also corresponds with the expected maximal tensile strain of the concrete (for C30/37  $\approx 80 \mu\text{strain}$  ( $= f_{ctm}/E_{cm} = 2.9 \text{ MPa}/33 \text{ GPa}$ )). The latter additionally confirms the good correlation between the strain peak of the Solifos V9 sensing cable measured with a BOFDA DAQ unit and the crack width of the DIC.

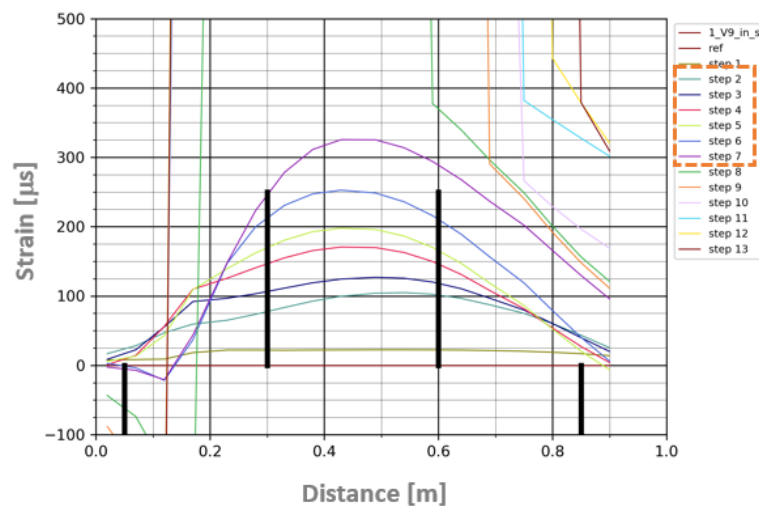


Figure 67. Detail of the results of the Solifos V9 sensing cable measured with a BOFDA DAQ unit.

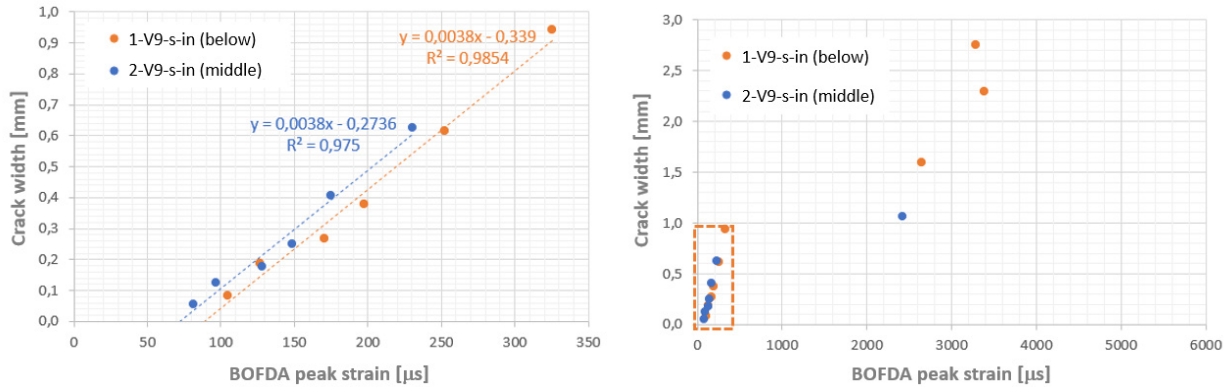


Figure 68. Linear regression of the peak strains of the Solifos V9 sensing cable measured with a BOFDA DAQ unit.

A much weaker correlation was observed between the strain peak of the Fibrain Flatdrop cable and the crack width. The linear regression results in a much steeper slope than the one observed for the Solifos V9 sensing cable. It can thus be stated that the Solifos V9 cable in combination with the BOFDA DAQ unit (FibrisTerre fTB5020) is suitable for crack detection and approximate crack width determination. However, in practice, the occurring cracks need to be sufficiently spaced. A spacing of more than 0.5 m is needed. When mounted internally, the Fibrain Flatdrop cable is in no case suitable for crack detection. This illustrates the importance of an appropriate cable selection for each individual project.

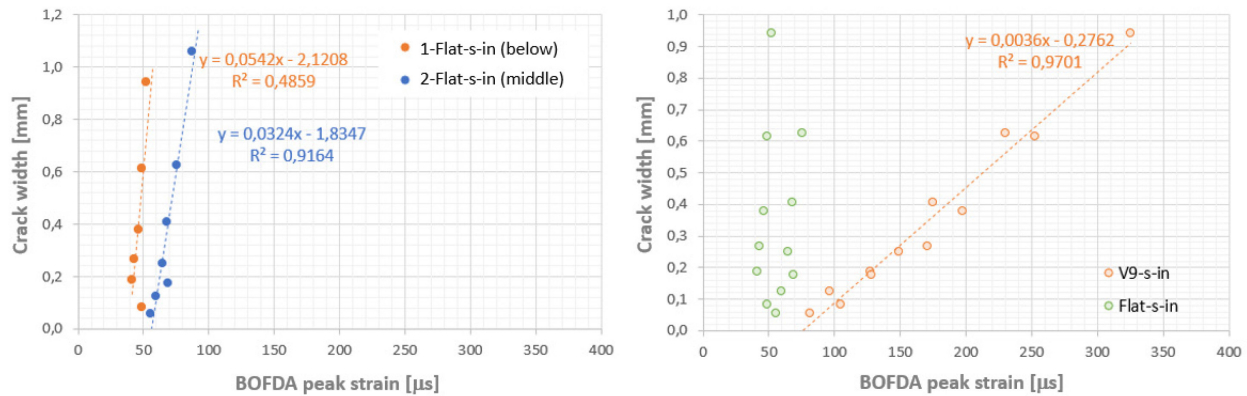


Figure 69. (left) Linear regression of the results of the Fibrain Flatdrop sensing cables in combination with the BOFDA DAQ unit and (right) comparison with the linear regression based on the readings of the Solifos V9 sensing cable.

This knowledge is highly useful for a practical case where cracking in concrete basement walls due to restraint deformations was studied. More details about this practical case can be found in Section 5.1.2. One of the basement walls monitored in the framework of the REINFORCE research project exhibited several restraint deformation cracks (see Figure 70). Typically, these cracks are visually measured, which is a punctual and a highly approximate measurement. Based on the validation tests presented above, an

estimate of the crack width was also performed by means of the monitoring data of the Solifos V9 sensing cable and compared with the visual crack measurements executed on the concrete surface.

To allow for such a conversion, the linear regression obtained through the validation experiments was converted to account for long term effects, specifically relaxation of the concrete. To this extend the tensile strength of the concrete was increased taking into account an estimated relaxation coefficient of 1.1 determined on a similar concrete. The intercept with the horizontal axis of  $80 \mu\text{strain}$  was increased to  $170 \mu\text{strain}$ . The regression coefficient is taken equal to the one found in the validation experiments as this parameter is only function of the crack width. By adopting this approach, a good approximation of the in-situ real time crack width could be obtained based on the Solifos V9 monitoring data, as illustrated in Figure 71.

This monitoring data also demonstrates the relative nature of a punctual visual measurement. The monitoring data clearly shows that the actual crack width highly fluctuates throughout the day, in function of a complex mix of boundary and environmental conditions.

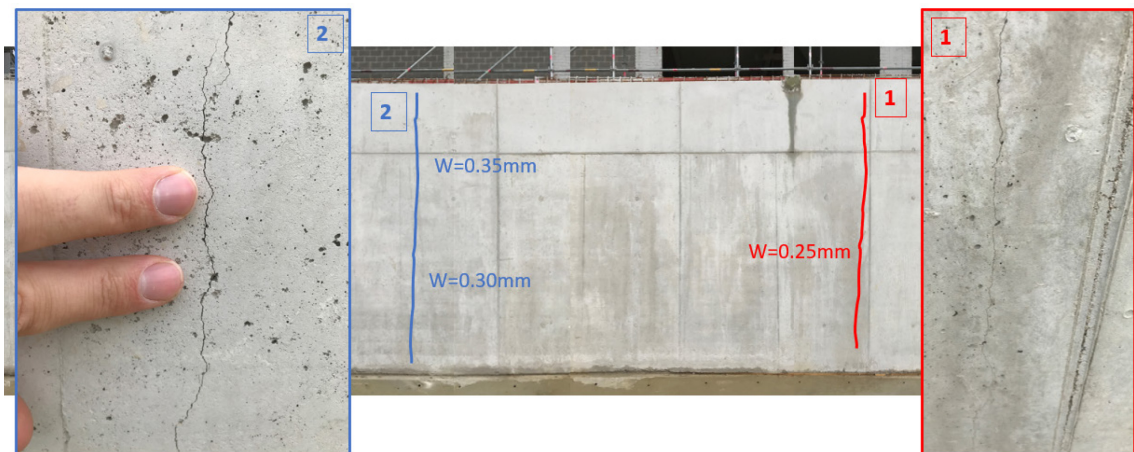


Figure 70. Visual crack width determination on a basement wall as part of a monitoring campaign within the REINFORCE research project.



Figure 71. Estimation of the crack width of crack 2 by means of the Solifos V9 monitoring data (BOFDA DAQ unit), based on the validation experiments executed on notched beams.

#### 4.3.4 Concrete corrosion monitoring

Three identical beams to the one tested in Section 4.3.1, equipped with the same FBG and BOFDA sensing cables, were subjected to accelerated corrosion caused by an electrical corrosion process. For this purpose, the bottom of the beams was put in a salt water bath (5% NaCl). At the bottom of this bath, a stainless steel plate was placed which is connected to the negative pole of a DC power source. The positive pole of this power source is in turn connected to the longitudinal reinforcement bars of the beam. The reinforcements act as a result as an anode, while the stainless steel plate will become a cathode. The electrolyte (salt water) will transport  $\text{OH}^-$  ions to the  $\text{Fe}^{++}$  charged rebars, which will lead to the development of corrosion products. Some pictures of the accelerated corrosion setup are shown in Figure 72.

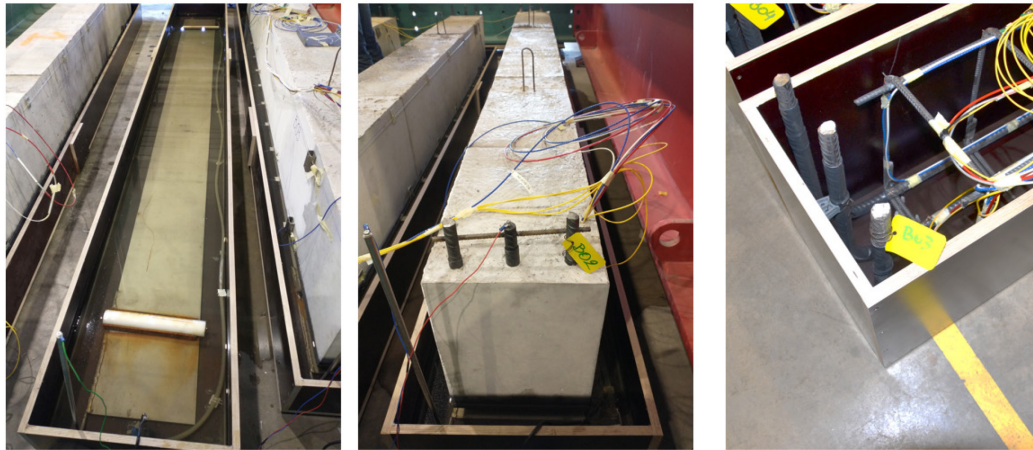


Figure 72. Accelerated corrosion setup. (left and middle) The blue/green cable connects the stainless steel plate to the negative pole of a DC power source. The red cable connects the longitudinal rebars to the positive pole of the DC power source. (left) Visual of PVC rolls and stainless steel plate. (right) Heat shrink tubes at the anchorage of the longitudinal rebars to prevent corrosion in this part of the rebar.

A constant current was imposed between the reinforcement and the stainless steel plate. This current was gradually increased during the accelerated corrosion test. The evolution of the predicted theoretical mass loss (calculated by means of Faraday's law) can be found in Figure 73. The real mass loss will most probably be lower than this theoretical prediction due to decreasing salt concentration, etc.



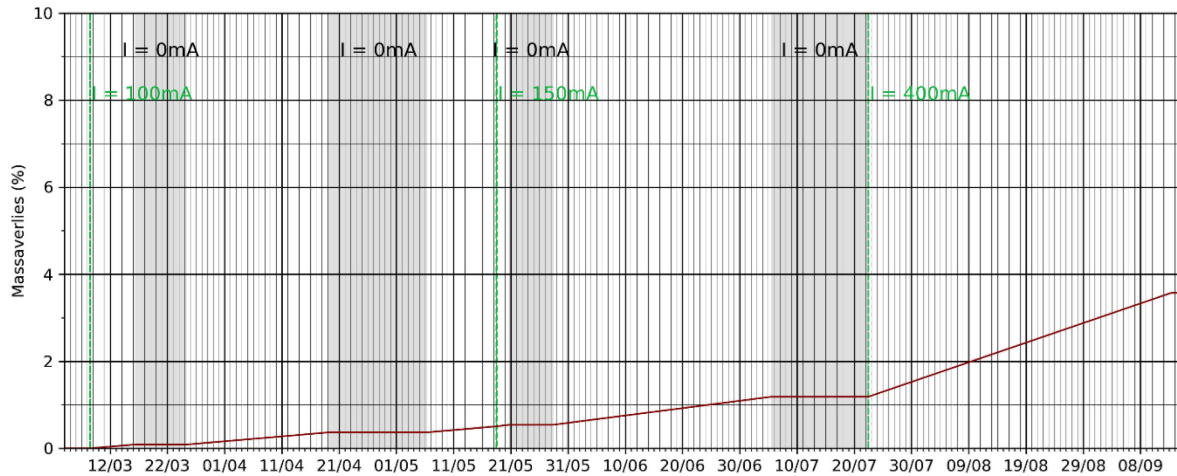


Figure 73. Predicted theoretical mass loss of the reinforcement during the corrosion experiment.

The 3 beams differ in pre-treatment (illustrated in Figure 74). Beam B01 was placed in the salt bath without pre-loading. Beams B02 and B03 were first subjected to a preloading of 250 kN. The purpose of this preloading was to evaluate the impact of bending cracks on the corrosion process and whether this would be detected with the fiber optics. The preloading of 250 kN corresponds to an introduction of cracks with a crack width of 0.13 to 0.21 mm (see Figure 74). This crack width range is well below the durability requirement of 0.30 mm. Note that after this preloading, the cracks close again. Consequently, a permanent load was placed on beam B03 to reopen the cracks. Because of practical constraints and safety considerations, only a limited permanent load of 25 kN could be placed on the beam. At the start of the corrosion process, the crack width of beam B03 was measured experimentally and was found to be approximately 0.04 mm.

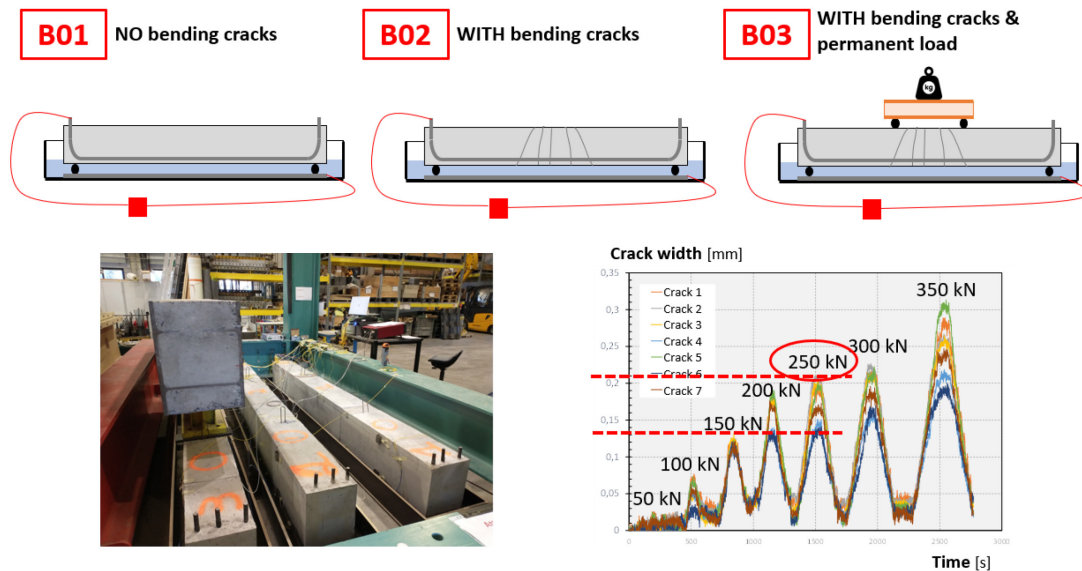


Figure 74. A schematic overview and pictures of the experimental setup for the accelerated corrosion experiments. (right bottom) pre-cracking load and range of crack widths (see reference beam experiment in Section 4.3.1).

The optical fiber sensor cables attached to the concrete outer surface of the 3 specimens were partially detached during the corrosion test. The mounting blocks were only glued to the concrete surface. During the accelerated corrosion experiment, the growth of corrosion products as well as deposition of salts revealed very harmful for this fixation principle, as some of the mounting blocks loosened during the test. Consequently, for long-term monitoring campaigns, an additional mechanical fixation is found to be necessary if external optical fibers are foreseen.

The internal sensing cables survived the accelerated corrosion test without any problems. Therefore, only these results will be elaborated in the next paragraphs. The semi-extensometer FBG setup proved to be the most performant. During the accelerated corrosion test, these sensors provided very interesting results. In Figure 75, the results of these FBGs are shown as a function of time, grouped per beam. The strains on the compression side (top side of the beam) are quite similar for the 3 beams. However, a clear difference can be observed between the results of the 3 beams on the tensile side (bottom of the beam, exposed to the corrosion conditions) and this already from the start of the accelerated corrosion test. In the tensile zone, beam B01 shows the lowest and beam B03 the highest tensile strains. Beam B02 is located somewhere in between these two. Zooming in on the start of the accelerated corrosion test, it can be seen that the results of beams B01 and B02 increase more or less equally until the end of October, after which the tensile strains of beam B02 start to increase more pronounced. Beam B03 already shows higher tensile strains from the start of the accelerated corrosion test.

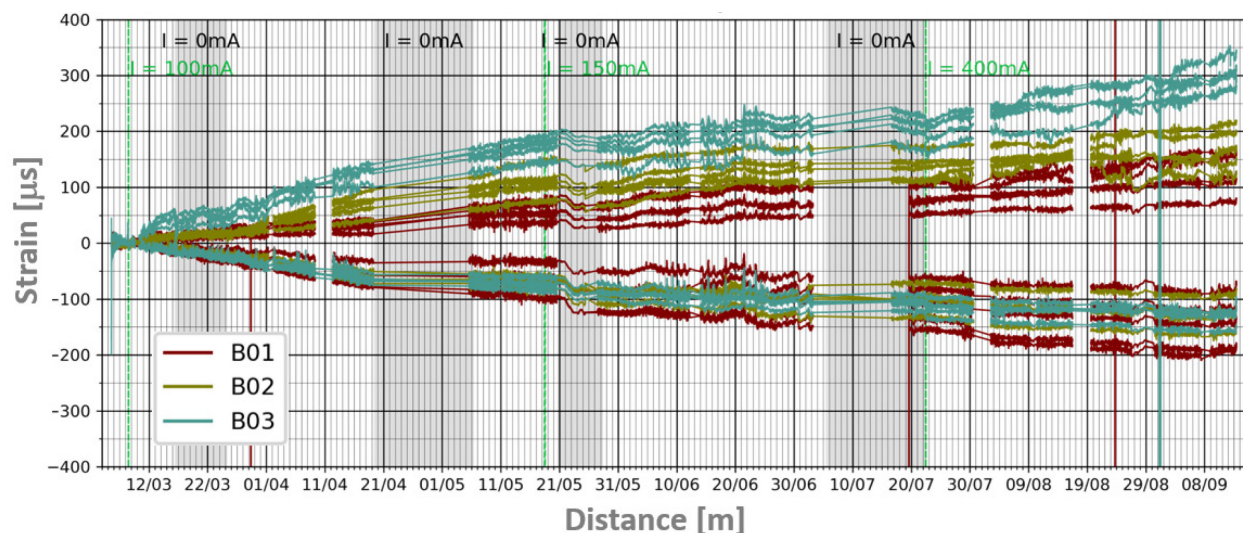


Figure 75. Results of FBGs installed in the centre of the beam with a semi-extensometer setup and this for the 3 beams exposed to the accelerated corrosion experiment.

Generally, the results of beams B01, B02 and B03 agree with the expectations, i.e., beams B02 and B03 will potentially corrode more/faster due to the presence of (open/closed) cracks. However, the measured tensile strains are much higher than expected. A finite element model was constructed in DIANA to determine the expected strains for the calculated theoretical mass loss (taking into account creep effects

and degradation of the concrete). This FEM modelling yielded significantly lower tensile strains than those measured during the test. It is therefore possible that other phenomena influence the measurements, e.g., lateral growth of corrosion products and growth of splitting cracks, moisture absorption by the optical fibers, chemical deterioration of the glass fiber, etc. More research is needed to clarify this. Despite these unknowns, it can nonetheless be concluded that optical fibers are useful in the context of corrosion monitoring.

The same general trend was observed with the BOFDA sensing cables. However, the differences observed between the inter-beam results are much less pronounced (certainly between B01 and B02).

At the end of the accelerated corrosion experiments, horizontal core drillings were carried out at the level of the point loads. In Figure 76 some pictures of one of these core drillings are shown. This core drilling was carried out at the level of the lower longitudinal reinforcements. It clearly shows the extensive network of splitting cracks and the deposition of corrosion products in these cracks. The optical fiber sensing cables are also visible. Based on this core, it becomes clear that the internal FBG sensors, which were provided in an extensometer setup, are located just at the level of a large splitting crack. This splitting crack connects the 3 rebars and is characterized by a large crack width. This might partially confirm the hypothesis made earlier, namely, that the optical fibers are also influence by other phenomena besides mass loss.



Figure 76. Pictures of a horizontal core drilling executed in beam B02 at the level of one of the point loads at the height of the lower longitudinal rebars.

---

During the accelerated corrosion process, the beams were also subjected to forced excitation dynamic tests during which the dynamic strains were measured with internal and external multiplexed FBG sensors. The aim was to monitor the modal characteristics that were identified from these dynamic tests, in order to investigate the influence of corrosion on natural frequencies and strain mode shapes. However, the modal characteristics that were obtained from these tests could not be used for damage detection purposes for beams B01 and B03 because it was found that they were also influenced by several other external factors.

The most important external factor influencing the monitored modal characteristic consisted of changes in the static boundary conditions of these beams. The beams had to be removed multiple times from the baths in which they were placed, while the water level in the baths was also fluctuating during the corrosion process. This led to an inconsistency of the external boundary conditions among the different tests. Boundary conditions define the stiffness of the beams and consequently, their modal characteristics. Since the boundary conditions were changed and corrosion damage was introduced at the same time, it was not possible to distinguish between both effects. This issue is less of a concern for full-size civil structures, as there the changes in the boundary conditions can be monitored separately.

Another factor that increased the uncertainty on the measured dynamic strains and consequently on the identified modal characteristics was the relatively low resolution of the acquisition unit employed during these tests, compared to the one that was used for acquiring the dynamic strains of B04. A very high accuracy and precision is required for low-amplitude dynamic strain measurements. Consequently, the relatively low resolution of the acquisition unit resulted in a relatively low accuracy of the identified the strain mode shapes of the beam. As a result, the ability to identify damage related changes on the strain mode shapes was also lower.

Even though the results of these tests could not be used for the reasons that they were initially planned for, they serve as valuable lessons for the planning of new experiments. Thanks to the acquired experience from B01 and B03, the tests on beam B02 were performed in a manner that permitted the investigation of the influence of corrosion on modal characteristics. The results indicate that strain mode shapes were not influenced by the induced corrosion, while natural frequencies were. Regarding strain mode shapes, the findings are in line with the expectations; the FBG sensors were measuring the longitudinal strains of the beam, meaning that they were parallel to the corrosion cracks and hence, could not detect them.

Regarding natural frequencies, they posed an increase with increasing level of corrosion, which is not in line with the expectations. In principle, corrosion should result in reduced stiffness and hence, to reduced natural frequencies. However, it has been reported in literature [34] that for low levels of corrosion, the bonding between reinforcement rebars and concrete can increase and this can result in increased stiffness and consequently, higher natural frequencies. Since the exact level of corrosion of B03 is not known, an increase of stiffness as a result of low levels of corrosion could be the explanation for the observed behaviour.

## 5 Monitoring cases

### 5.1 Innovative systems

#### 5.1.1 Innovative grout anchor and piling system (Smet-F&C)

In the framework of the development of an innovative execution technique for foundation elements (grout anchors and foundation piles), Smet-F&C applied in-field fiber optic monitoring. The innovative execution technique consists of a post-injection grouting, i.e. a few hours after the execution of the element grout is injected through dedicated injection tubes. This results in higher bearing capacities of the foundation element. The aim of the in-field monitoring is (1) to assess the performance of the post-injection process and (2) to quantify the increased bearing capacity during static load tests.

The use of distributed fiber optic sensing has proven to be highly effective in this case, as a very detailed insight of the mechanical behaviour is obtained. It also offers a valuable tool to assess the mobilization of the soil resistance and the estimation of the remaining anchor/pile capacity and can thus be applied to perform long-term health monitoring of such elements under operational conditions. Moreover, the measurements allowed a further optimization of the execution technique. This wouldn't have been possible with traditional sensing techniques. In the framework of two MSc Theses at KU Leuven, analytical and numerical models were developed and calibrated with the monitoring data [35, 36].

Similar tests have been conducted in the past in Austria [37, 38].

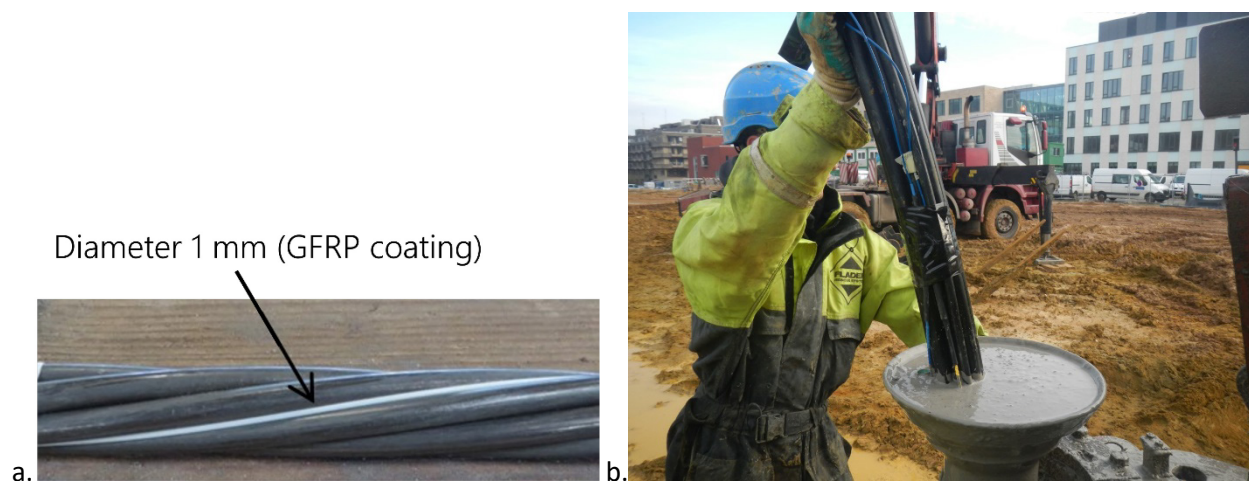


Figure 77. (a) Fiber integrated into a steel tendon. (b) Fibers attached to the outer surface of the anchor tendons during their installation in the borehole.

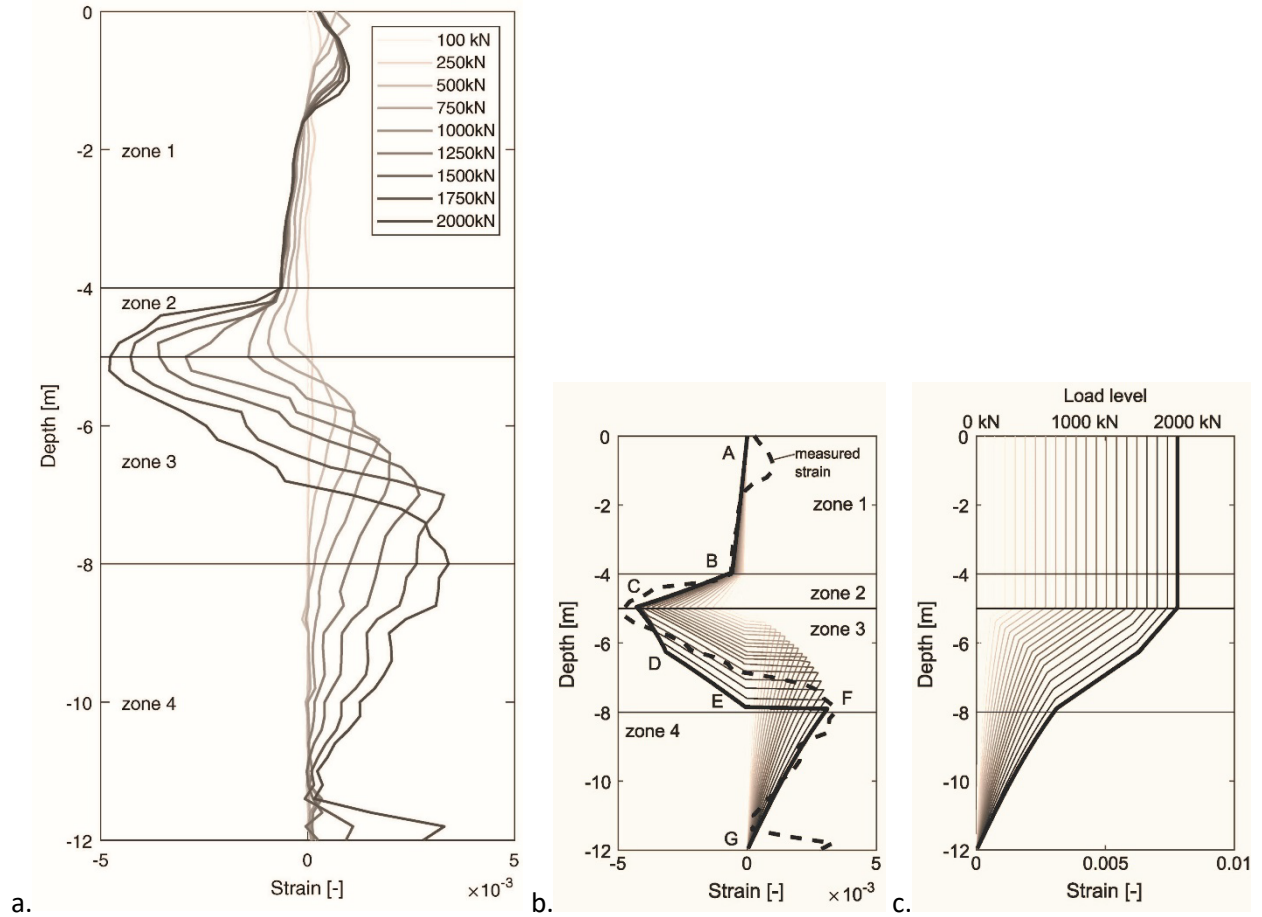


Figure 78. (a) Axial strains in the grout anchor during a static load test measured by a fiber in the grout body with the BOFDA technology. Zones 3 and 4 correspond to the tendon bond length. Numerical simulations of the axial strains of (b) the grout body and (c) the steel tendons. For the last load step at 2000 kN, the strain measured in the grout body is shown as well (b). Image source: [36].

### 5.1.2 Reinforce research project

The aspect of minimum reinforcement for slab-shaped elements made of concrete (floors and walls) is often a bone of contention between contractors and engineers on jobsites. This minimum reinforcement aims to accommodate restrained deformations mainly due to shrinkage and temperature variations. Insufficient minimum reinforcement inevitably leads to undesirable cracking. Excessive minimum reinforcement, in turn, has a clearly negative economic impact.

Given the need for guidelines on this minimum reinforcement issue, Buildwise, together with KU Leuven (Campus Denayer) and UHasselt, launched a prenormative study REINFORCE on the topic. In order to gain more insight into the actual deformation behaviour of walls (in particular basement walls) under real restraining conditions, several very diverse concrete elements were monitored on jobsites by means of optical fiber sensing cables. Pictures of some monitored elements in this context can be found in Figure 79. An illustration of the typical monitoring setup is shown in Figure 80. The walls were instrumented at 3 levels and 2 depths with both temperature and strain optical sensing fibers.



Figure 79. Two of the monitored basements walls. (left) Basement with a double formwork with pins to connect the two sides. (right) Basement cast in front of a Berliner wall with a traditional formwork closing off the other side.



Figure 80. Illustration of the typical monitoring setup used in the REINFORCE project. With optical fiber sensing cables at 3 levels and 2 depths in the wall (indicated with the yellow arrows).

Optical fibers were embedded in the concrete as this allows monitoring of concrete deformation already at very early age, typically 6 to 8 hours after casting of the concrete. In certain wall structures, high temperatures can build up during the hydration process. This is clearly demonstrated by a monitoring campaign with OF sensing cables of a massive basement wall constructed in front of a Berliner wall (see Figure 81). Classical measuring techniques such as Demec measurements can only be started after at least 24 hours, as they can only be applied/glued to the concrete surface after demoulding. For basement walls poured against earth retaining structures (such as Berliner walls, soil mix walls, etc.), optical fibers can also be used to monitor the rear side of the wall, which is not possible with the aforementioned conventional measuring method.

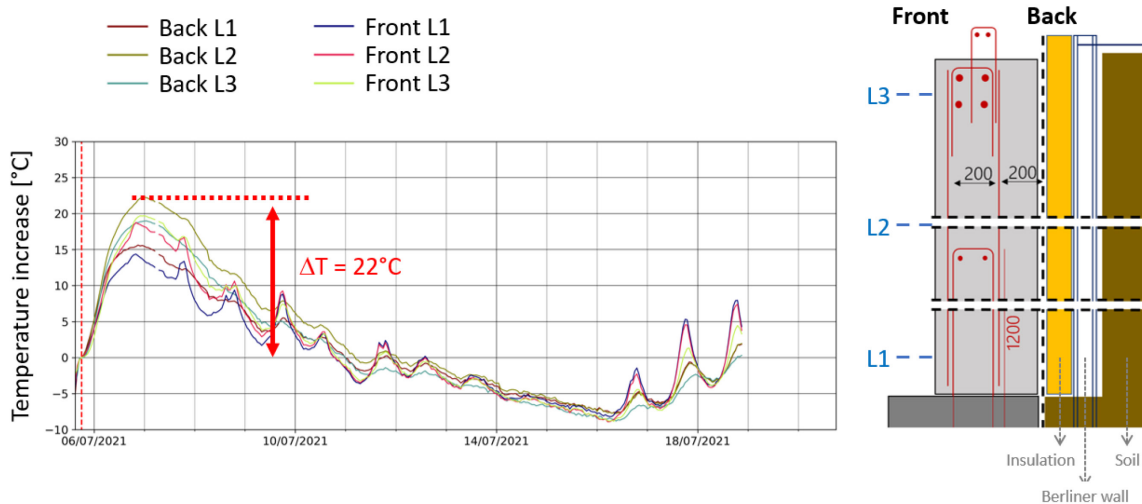


Figure 81. Evolution of the temperature monitored with temperature sensing cables (BOFDA DAQ unit) within a basement wall of which the assembly is illustrated at the right of the figure.



For this study, the BOFDA technology was selected. Since it is difficult to predict where restraints will occur in the structure nor where cracks (if any) will appear over time, distributed sensing technologies are the most adequate monitoring system as it allows for large-scale monitoring with a high sensor density (i.e., number of measurement points per unit length). This combined with a non-labour-intensive installation and only limited cabling, resulted in a minimal disruption of the contractor's jobsite activities. During the test campaigns conducted in the framework of the REINFORCE project, the BOFDA measurement technique proved to be very valuable. It showed for instance that the formwork ties, used in double-sided formwork, can present an additional source of restraint in certain wall constructions (in particular thin concrete walls). This phenomenon can be clearly seen in the monitoring data presented in Figure 82.

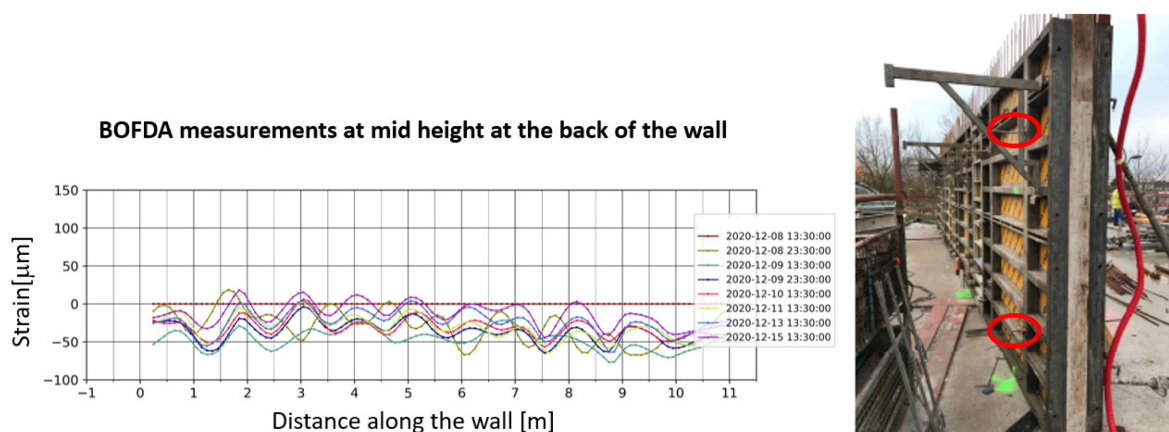


Figure 82. Strain profile observed along a thin concrete wall cast with a double sided formwork system.

The strain averaging, inherent to the BOFDA technology (“spatial resolution”), also showed very useful in allowing for crack detection and localisation. This can be seen in Figure 83, where some results are presented of a monitoring campaign in which cracks were observed. As already mentioned in Section 4.3.3, the crack width could also be estimate, which is very valuable as this allowed to evaluate the crack width at the back of the wall which was against the earth retaining wall and thus inaccessible for traditional crack width measurement techniques.

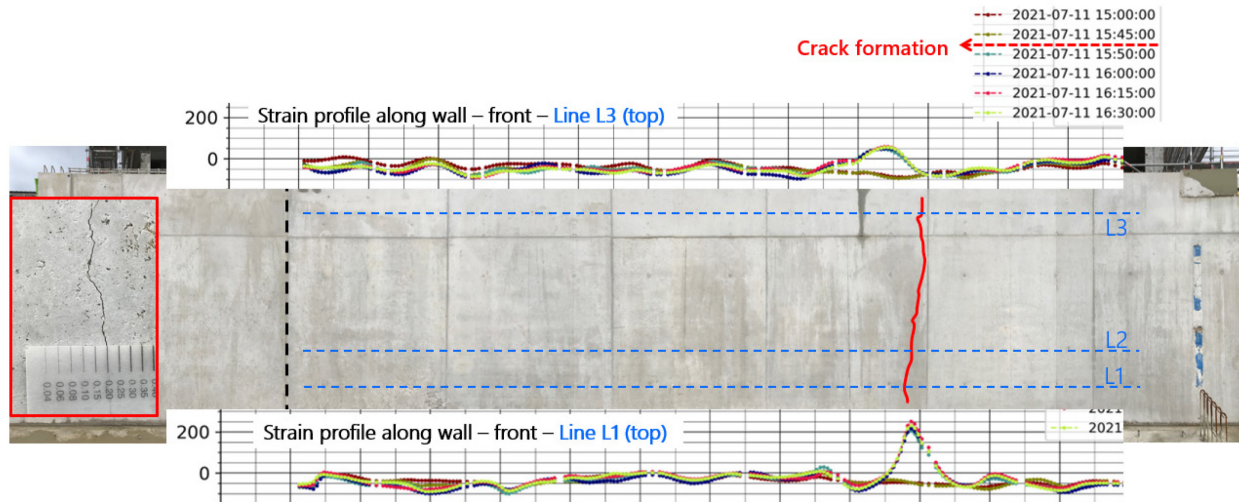


Figure 83. Crack formation observed in the strain profile of one of the monitored walls in the REINFORCE project.

The BOFDA sensing technology also offered very detailed global insights. For instance, a good estimation of the global length change at different levels could be reconstructed (see also Figure 84), allowing for global restraints to be estimated quite accurately.

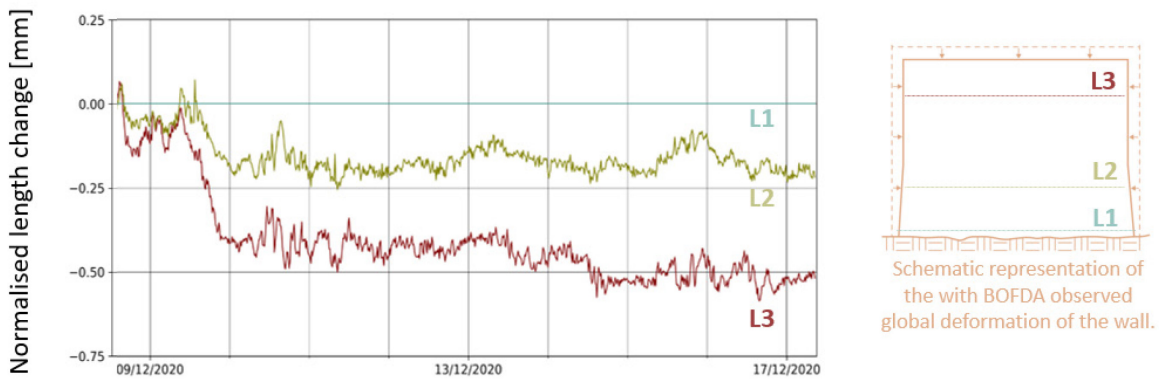


Figure 84. Global length change profile of one of the monitored walls in the REINFORCE project.

### 5.1.3 Innovative basement wall system (Prefaxis)

Prefaxis developed an innovative single-sided precast concrete twin wall system for the construction of basement walls against earth retaining structures. This innovation allows for a quick and efficient erection of basement walls, without a complex formwork or shoring system. See Figure 85 for an example of a construction site where this innovation has been used.



Figure 85. Single-sided precast concrete twin wall system developed by Prefaxis, for realising basement walls against an earth retaining structure.

For the further finetuning of their product, Prefaxis wanted to get a better insight into the restraint deformations of their basement wall construction. The wall consists of a single-sided precast concrete thin wall and a cast-in-place concrete core (ready mixed concrete poured on site between the precast panel and the earth retaining structure, see also Figure 86). The finished wall often serves as an impermeable wall. To this extent, specific measures are taken to limit the occurrence of inconvenient cracking due to restraint shrinkage and temperature deformations.



Figure 86. Cast-in-place concrete core poured on site between the precast panel and in this case a Berliner wall.

Above mentioned measures are based on years of practical experience with traditional basement walls constructed by means of double-sided formwork. Due to the specific composition of the innovative basement wall concept (with a relatively stiff precast concrete panel at the front with built-in lattice girders) and the possible interactions with the earth retaining structure behind the wall (secant pile wall, Berliner wall, soil mix wall, etc.), Prefaxis expected that the restraints experienced by the cast-in-place concrete core could substantially deviate from those observed for traditional concrete basement walls. To get a better idea of this, a monitoring campaign using optical fiber technology was proposed by Buildwise in consultation with Prefaxis. A first layer of optical fiber sensing cables was mounted at 3 levels on the precast concrete shell. This was done by means of support rods which were attached to the lattice girders at the rear of the precast concrete shell. A second layer was attached to the reinforcement mesh at the rear of the cast-in-place concrete core, just in front of the soil retaining structure (see Figure 87).



Figure 87. (left) First layer of optical fiber sensing cables attached with support rods to the precast concrete shell. (right) View of the optical fibers installed on the reinforcement mesh at the rear of the concrete core, before closing the wall with the precast concrete shell.

Prefaxis's suspicion with regard to the altered restraint was confirmed by the monitoring. A clearly different deformation profile was observed (see Figure 88 compared to Figure 84). While in traditional walls the base of the wall is mainly restraint, in this wall type restraint is observed over the full height of the wall. Reinforcement should therefore be provided over the full height of the wall in the cast-in-place core and not only at the base of the wall.

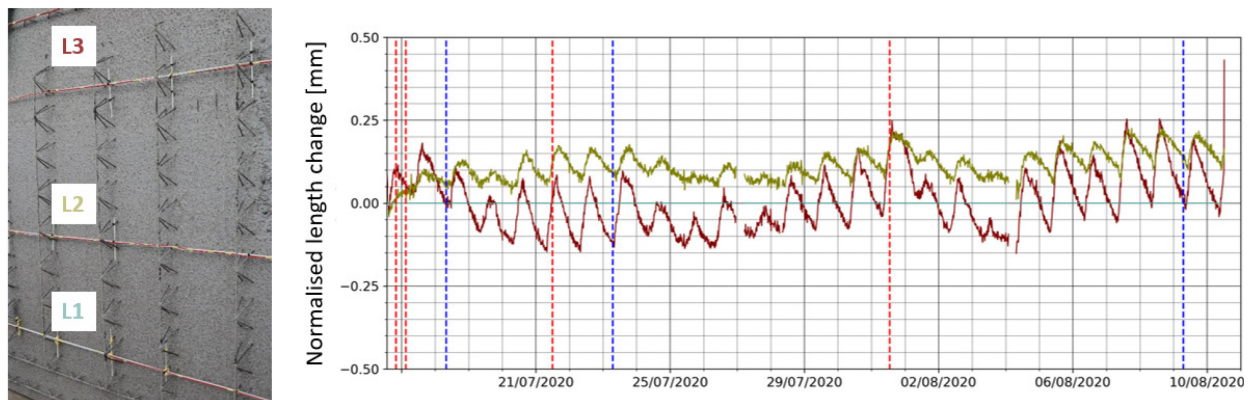


Figure 88. Global length change profile of one of the monitored Uniwalls.

## 5.2 Proof testing

### 5.2.1 Instrumented static pile load tests

In literature, many applications of instrumented static (and dynamic) load tests on foundation piles (and other geotechnical elements) have been published [21, 39-42]. As fiber optic sensors are very compact, they can rather easily be integrated in geotechnical structures, after or even during their execution.

The very high sensor density of fiber optic sensing offers a lot information about the behaviour of the structure, leading to better insights. When performing a static load test to determine the ultimate bearing capacity of the foundation pile, the strains measured along the pile length during subsequent load steps (Figure 89) can be converted to load distribution in the pile. This allows determining the soil characteristics and pile design factors. Moreover, local anomalies can be detected. E.g., in Figure 89, the higher strains at the bottom of the pile could indicate concrete segregation. A deviating pile diameters can be detected in a similar way.

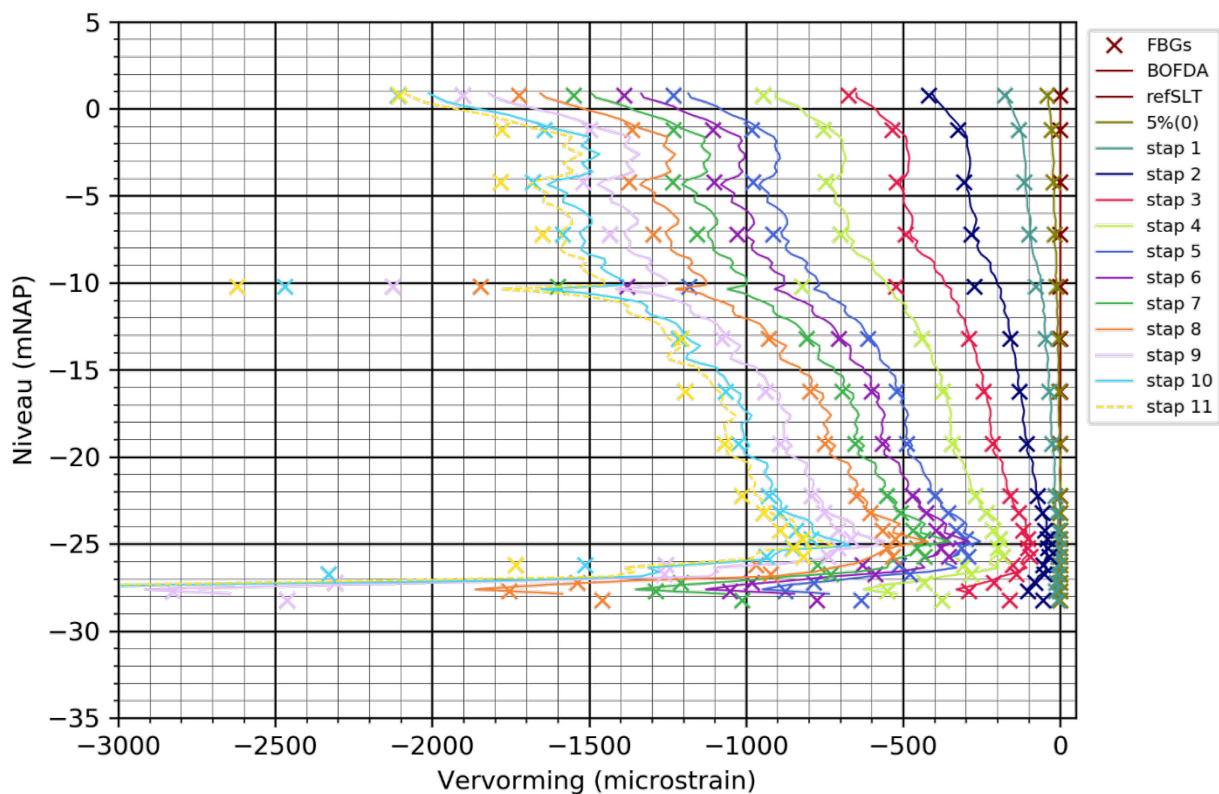


Figure 89. Example of the strain distribution in function of depth for several load steps during a static load test on a foundation pile performed by Buildwise. The crosses are FBG sensors, the continuous line are BOFDA sensor lines.

### 5.2.2 Composite bridge, Bruges (Vlaamse Waterweg and MOW-EBS, Buildwise and KU Leuven)

The upstream Canada bridge is one of two nearly identical footbridges crossing the Afleidingsvaart canal in Bruges, Belgium (Figure 90). The bridge has a continuous 3-span deck which is slightly curved in the vertical plane. It sits directly on two intermediate concrete piers and on two concrete abutments at its ends. The deck has a width of 3.83 m and a total length of 41.5 m, while the spans have lengths of respectively 15.7 m, 8.0 m and 17.8 m. The deck is composed of Fiber-Reinforced Polymer (FRP) material and was manufactured in one continuous piece by vacuum infusion. The cross-section of the deck has a constant height of 0.6 m and consists of 17 hollow boxes, filled with PU-foam.



Figure 90. The upstream Canada footbridge, as seen from its north side. Photo reproduced with permission from [43].

Buildwise equipped the bridge with 120 FBG sensors inscribed in eight optical fibers with Glass Fiber-Reinforced Polymer (GFRP) coating and 1 mm outer diameter. These fibers are embedded in the FRP deck and are used to measure the local static and dynamic strains of the bridge in their immediate vicinity. Out of 120 FBGs, 64 are distributed across the length of the bridge, 31 at the top and 33 at the bottom, as illustrated in Figure 91. These sensors are located at the vertical plane of symmetry of the cross-section of the deck and are embedded in the top and bottom plates (Figure 92). The other FBGs are measuring the longitudinal local strains at the locations where the bending moment around the transversal axis has a maximum amplitude (Figure 91). They are distributed within the cross-section, as illustrated in Figure 92. The reader is referred to [43] for a more detailed description of the FBG monitoring system. Additional BOFDA strain and temperature sensing cables are integrated in the bridge as well.

The novelty of this work lays on the fact that the FBGs were embedded in the FRP deck during manufacturing, which means that the structure can be monitored from the very beginning of its service life and also that the sensors will always be protected against the environment and other external factors.

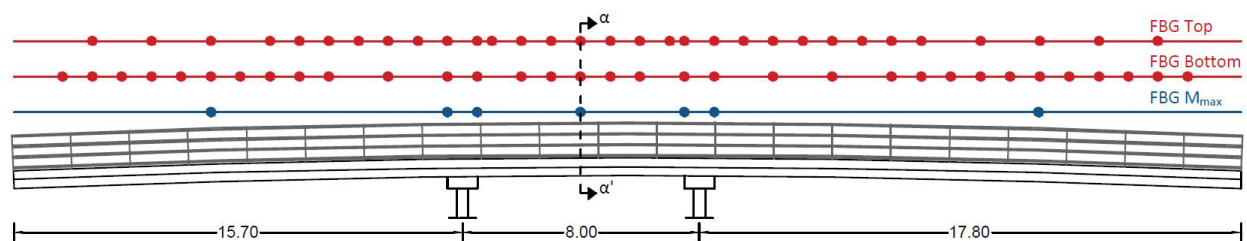


Figure 91. Front view of the FBG strain monitoring system of the upstream Canada footbridge. The locations of the FBGs at the top (FBG Top) and bottom (FBG Bottom) plate as well as at the theoretical locations of maximum bending moment about the longitudinal axis (FBG  $M_{max}$ ) are indicated. Dimensions in [m]. Photo reproduced with permission from [43].

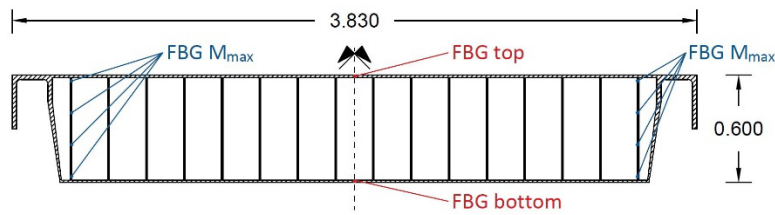


Figure 92. Typical cross-section of the deck of the upstream Canada footbridge. The locations of the FBGs at the top (FBG Top) and bottom (FBG Bottom) plate as well as at the theoretical locations of maximum bending moment about the longitudinal axis (FBG  $M_{max}$ ) are indicated. Dimensions in [m]. Photo reproduced with permission from [43].

The bridge is not permanently monitored but strain measurements can be conducted at any time by simply connecting the embedded fibers to an acquisition system. All sensor cables are collected in 2 small boxes below the bridge deck at both extremities. If a sensor cable breaks at a certain position, all sensors can still be read via the other cable end.

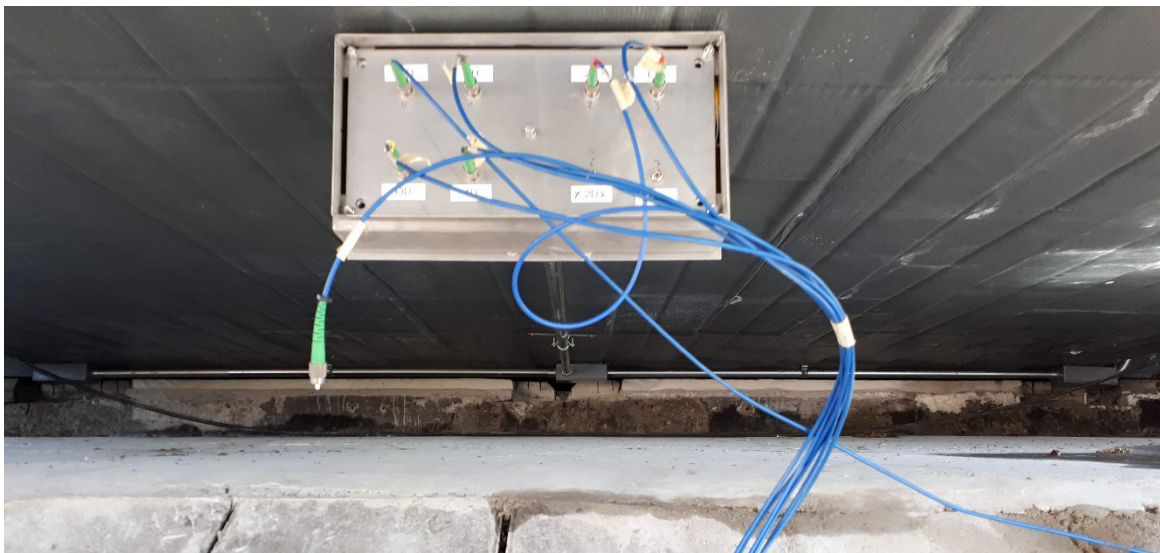


Figure 93. All sensor cables are collected in a small box at both extremities of the bridge from which they can easily be connected to the DAQ unit.

During the first 2 years after the installation of the bridge, several static load tests have been conducted by Buildwise in the framework of a PIO project financed by the Flemish Government. In Figure 94, an example of the measured strains during a static load test with the load in the middle of the right span is shown. The deformations measured with the FBG sensors correspond well with those measured by the BOFDA strain sensing cable. The monitoring lead to a better insight in the mechanical behaviour of the bridge. During the static load tests, some deviating strain values were detected at the supports and the influence of temperature on the behaviour of the bridge was remarkable. As the monitoring of the sensors was launched before production (i.e., before injecting the resin), interesting information about the manufacturing process was obtained as well.



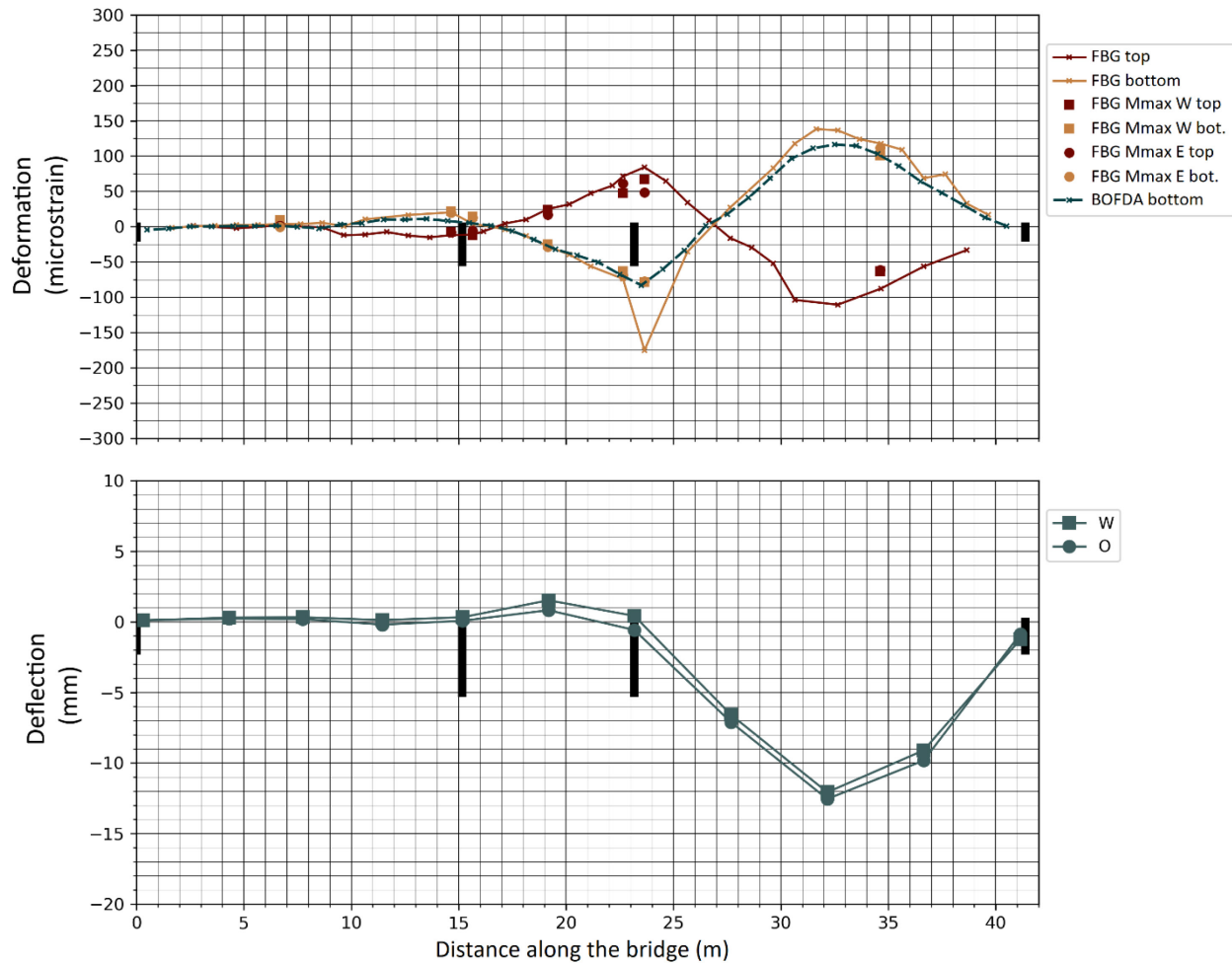


Figure 94. Measured deformations and deflections along the length of the bridge deck during a static load test (load in the middle of the right span). (Above) Deformations measured by the FBG sensors (FBG Top and FBG Bottom (solid lines) and FBG  $M_{max}$  (squares and circles)) and by the BOFDA strain sensing cable (located near FBG Bottom). (Below) Vertical deflection measured with a total station.

During 2020-2022, periodic vibration monitoring has been performed by KU Leuven on the upstream Canada footbridge. For this purpose, the bridge was subjected to strain-based experimental modal analyses (EMA), which were performed on two instances, in order to identify its modal characteristics, i.e., natural frequencies and strain mode shapes that describe the structure's condition at the moment of testing.

The first strain-based EMA was performed on 12 June 2020 and the second on 20 April 2021. Both EMAs were performed under similar temperature conditions, to ensure that the influence of temperature on the modal characteristics would be limited. Based on the comparison of the modal characteristics between the two EMAs, no change in the structural condition of the bridge was identified.

The influence of relevant damage scenarios for FRP bridges, such as detachment between the different deck components, was also investigated through numerical simulations in ANSYS. Strain mode shapes have been proved highly sensitive to local damage, contrary to natural frequencies [43], even when a

---

realistic identification uncertainty is accounted for. The reader is referred to [43] for detailed results, insights and simulation results.

The knowledge of the temperature dependency of a structure's modal characteristics is necessary for correctly identifying damage, since both temperature and damage can influence these characteristics. From 4 May 2022 to 14 June 2022, the bridge was continuously monitored and the measured operational and ambient dynamic strains were used to identify its natural frequencies and strain mode shapes. Consequently, the evolution of natural frequencies and strain mode shapes over time, as well as the influence of temperature and loading could be studied.

No influence of temperature on natural frequencies and strain mode shapes could be identified, for a temperature range of 30°C [5°C-35°C]. The findings are surprising with respect to natural frequencies, which typically are influenced by temperature, but not with respect to strain mode shapes, which are usually insensitive to temperature [25]. A possible reason for this insensitivity of natural frequencies could be the low resolution of the employed acquisition system, which resulted in higher modal characteristics identification uncertainty. Higher uncertainty can mask the effects of temperature but also damage on modal characteristics. These findings underlined the importance of high-resolution acquisition units in vibration-based monitoring.

### 5.2.3 Oosterweel test pit, Antwerp (Lantis)

In order to improve the mobility situation in and around Antwerp, Lantis conceived the plan to close the ring road by building the Oosterweel link. To assess the technical feasibility of the plans, Lantis carried out several large-scale test campaigns (see also the case in Section 5.4.2 about “Temperature monitoring of diaphragm walls, Merksem (Lantis)”). Based on the information thus required, it was possible to design and execute the Oosterweel link in a more efficient and more economical way.

One of the test campaigns involved the construction of a 25 m deep test pit (Figure 95a). [44, 45] present the test campaign and give more information about the objective and the results. Several optical fiber FBG sensors were installed in the test pit: (1) on the sheet piles in reservation tubes, after their installation and prior to excavation (see Figure 52a), (2) on the 5 strut levels of the test pit (see Figure 50a) and (3) in a 50m deep borehole into the Boom clay (see Figure 52b). In Figure 95b, the bending moment in the sheet pile wall is shown during a certain excavation phase (calculated based on the FBG strain measurements on the sheet piles).

The test campaign allowed to define a proof of concept, a cost effective design, calibrated soil parameters and a reduction on risks during design and execution.

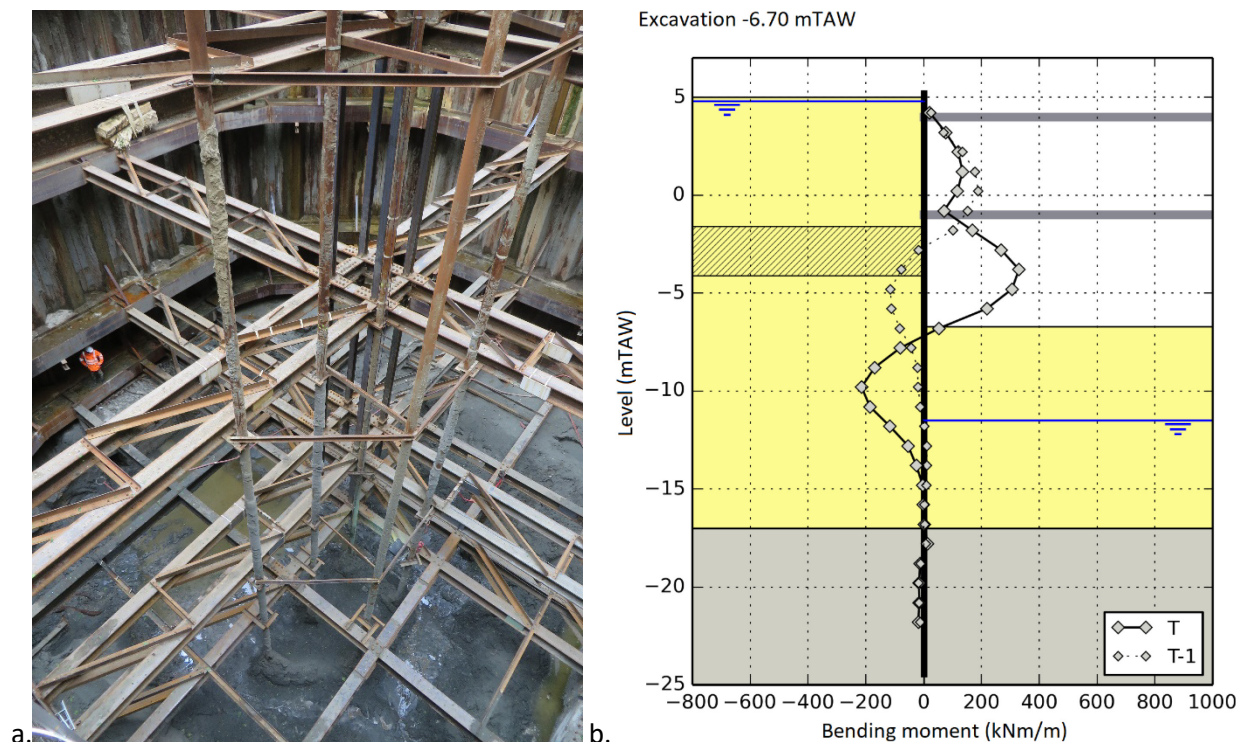


Figure 95. (a) A picture of the Oosterweel test pit during execution. (b) Bending moment in the sheet pile calculated based on the FBG sensors on the sheet piles.

### 5.3 Long term monitoring

#### 5.3.1 Geotextile monitoring of a dike, Nieuwpoort (Maritime and Coastal Services, Flemish Government and Com&Sens)

The slopes of dikes (e.g., near harbours and harbour channels) are constantly subjected to wave action and tides. This sometimes causes hidden damage under the concrete cover slab due to erosion. The Maritime and Coastal Services of the Flemish Government decided to test an innovative monitoring technique to detect such damage in an early stage.

In the framework of the renovation of a dike slope in the harbour channel of Nieuwpoort, Belgium, Com&Sens instrumented the geotextiles below the concrete slab with fiber optic FBG sensors (Figure 96a and b). The idea is that when cavities occur, the fastest way to detect them is to measure the deformation of the geotextile which is located below the concrete slab. A total of 140 FBG sensors were installed to cover a surface of 280 x 18 square metre. These sensors are monitored every 20 minutes, in order to capture the influence of tides. Figure 97 illustrates a graphical view of the resulting monitoring data. In a next stage, once a sufficiently long data history has been acquired to define a reference frame, the data will be further analysed.



Figure 96. (a) The finished dike slope in the harbour channel of Nieuwpoort, Belgium. (b) The geotextile during instrumentation with fiber optic FBG sensors.

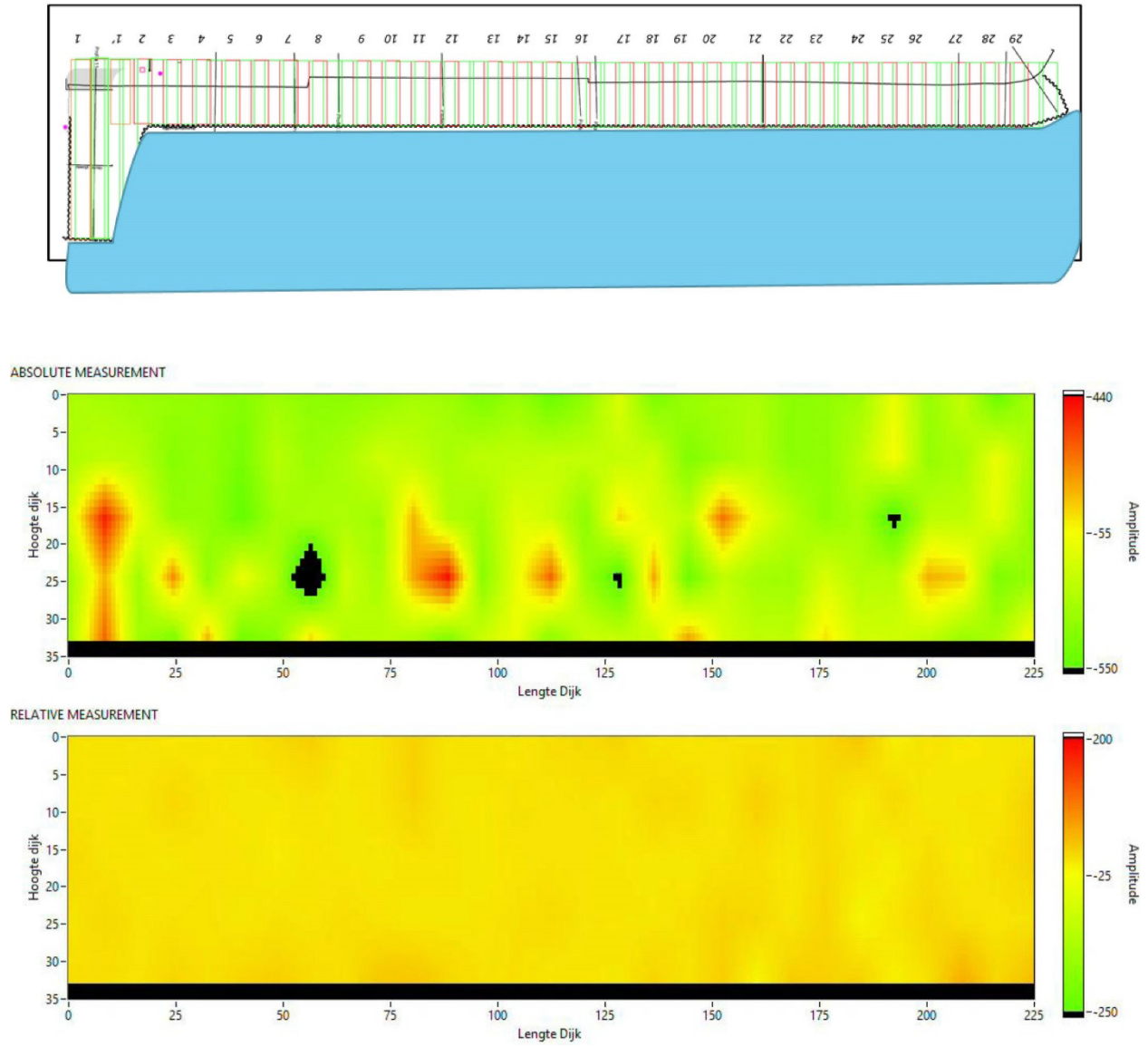


Figure 97. Example of the strain measurements on the monitored section.

### 5.3.2 Steel bowstring bridge KW51, Leuven (Infrabel and KU Leuven)

The KW51 is a 117 m long railway bridge that crosses the Leuven-Mechelen canal close to the city of Leuven, Belgium. The bridge is part of the 100 km railway Line 36 that runs from Brussels to Liege and is used exclusively by passenger trainsets. KW51 is a steel single-span tied arch bridge with a two-track deck that is suspended from the arch with thirty-two inclined braces (Figure 98). The orthotropic deck has a width of 14.15 m and consists of two main girders stiffened by thirty-three transverse beams. The bridge is supported on four neoprene bearings at its ends, which directly sit on two concrete abutments.



Figure 98. The KW51 bridge, as seen from its north side. Photo reproduced with permission from [25].

The monitoring of the dynamic strains of the KW51 bridge was initiated on 14 February 2019 and was concluded on 5 March 2021, spanning a period of more than two years. Dynamic long-gauge strains or macrostrains of the bridge have been monitored with four chains of FBG sensors, inscribed in optical fibers with a glass-fiber reinforced polymer (GFRP) coating for high strength and protection. The fibers are located at the top surface of the bottom flange of the main girders (Figures 99 and 100). Each fiber contains 20 FBG sensors. The fibers are attached to the flanges of the girders via a custom clamping system [25], to measure axial dynamic strains. The FBG sensors measure the average strain or macrostrain between two clamping blocks over a distance (gauge length) of about 2.5 m. The reader is referred to [25] for a more detailed description of the FBG monitoring system.

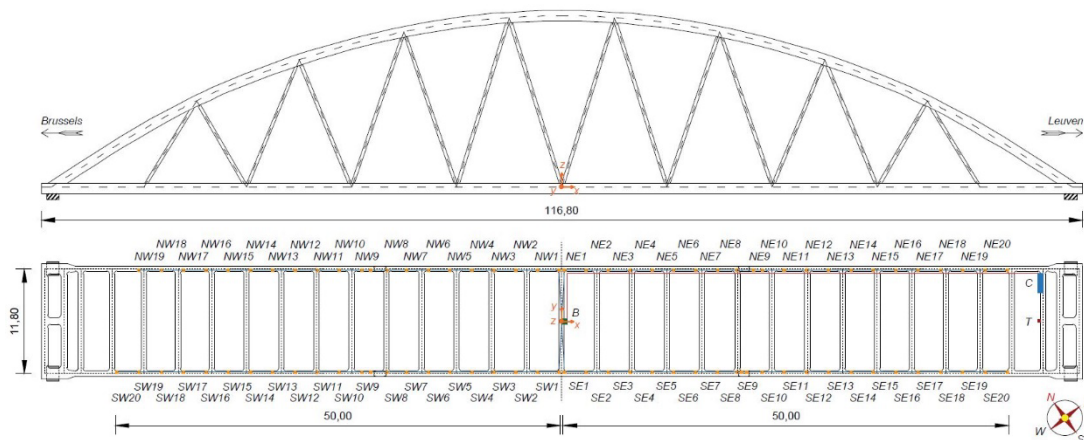


Figure 99. Overview of the FBG strain monitoring system. Top: south view of the KW51 bridge. Bottom: Schematic representation of the attachment of the optical fibers (top view). The small cubes represent the clamping blocks and the rectangles the FBGs in between the clamping blocks. All FBGs are labelled; NE stands for northeast, NW for northwest, SE for southeast and SW for southwest (dimensions in m). Photo reproduced with permission from [25].

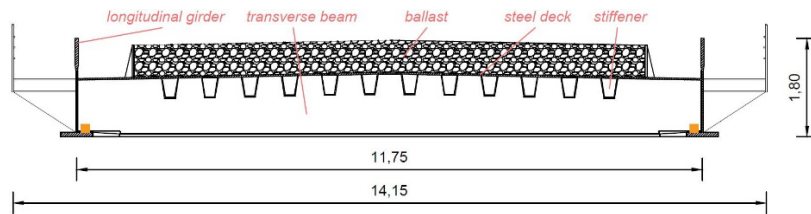


Figure 100. Typical cross-section of the deck of the KW51 bridge (dimensions in [m]). The small cubes represent the clamping blocks that are used to attach the FBG fibers. Photo reproduced with permission from [25].

Every hour, the fiber-optic strain monitoring system captured 900 s of dynamic strain data under ambient and operational excitation from all FBGs installed on the bridge at a sampling rate of 1,000 Hz. Each set of ambient strain data is used for automated Operational Modal Analyses (OMA), to identify the modal characteristics of the bridge, i.e., natural frequencies and strain modes shapes, which represent the state of the bridge at the corresponding time. In total, more than 10,000 operational excitation tests were conducted during the monitoring period.

The monitoring of the KW51 bridge with a dense grid of FBG sensors was a state-of-the-art experiment that was performed within the framework of a PhD thesis for research purposes [29]. The novelty of the experiment lays to the fact that this was the first time that the detailed strain mode shapes of a full-scale civil structure were continuously identified with high accuracy and precision under ambient and operational conditions, which is a requirement for vibration-based structural health monitoring.

Furthermore, the influence of temperature on the identified strain mode shapes was investigated. A temperature insensitive modal characteristic would be valuable for vibration-based monitoring (VBM), as it could be directly used for damage detection without requiring data normalization to remove the influence of temperature. In the present experiment, strain mode shapes were found insensitive to temperature changes higher than 0°C, while a small but uniform influence was identified for a few modes during frost due to the freezing of the porphyry ballast [33]. Nevertheless, this influence was smaller than the influence that temperature has on natural frequencies, giving strain mode shapes an extra advantage for the practical VBM. Furthermore, numerical simulations demonstrated the ability of strain mode shapes to detect and localize small-scale damage, contrary to the natural frequencies that remained almost unchanged [33].

### 5.3.3 Steel railway bridge, Ronse (Infrabel, TUC Rail and KU Leuven)

The Nieuwebrugstraat bridge was a 13.5 m long railway bridge located at the town of Ronse, Belgium. The bridge consisted of four identical spans that were parallel to each other (Figure 101). Each span consisted of two main I-shaped girders, connected by ten I-shaped transverse beams. Steel plates connected the girders and the transverse beams to form the bridge deck. A concrete slab with an average thickness of 10 cm covered the steel plates. Gravel ballast laid on top of the concrete slab with a thickness of about 40 cm. The span width was approximately 2.8 m. The bridge rested on four steel supports, which directly sat on two concrete abutments (Figure 101). The bridge was replaced by a new structure in April 2022.



Figure 101. The Nieuwebrugstraat bridge, as seen underneath (left) and from the top (right).

One span of the Nieuwebrugstraat bridge was monitored from 1 May 2021 to 31 March 2022. The monitored span was not in service and was adjacent to the only operational span (Figure 101). The monitored span can be seen in Figure 101, restricted with steel fences. The dynamic macrostrains of the span were monitored with four optical fibers, each equipped with 20 FBG sensors. The fibers were located at the top surface of the top flange of the main girders (Figure 102). The fibers were attached to the flanges via a custom clamping system [25], to measure axial dynamic strains. The FBG sensors measured the average strain or macrostrain between two clamping blocks over a distance of 25 cm. The reader is referred to [46] for a more detailed description of the FBG monitoring system.

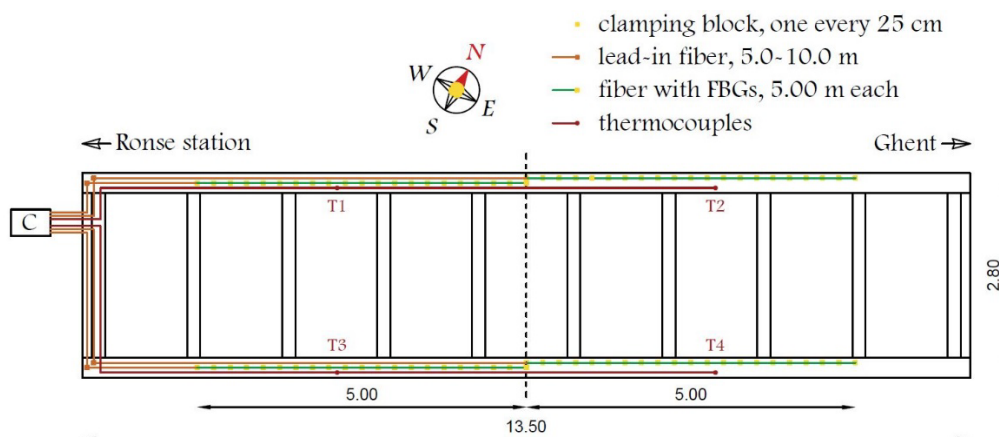


Figure 102. Overview of the FBG strain monitoring system and the attachment of the optical fibers (top view). The small cubes represent the clamping blocks. An FBG exists in between two clamping blocks. C denotes the cabinet that contains the laptop and the acquisition system. T1-T4 denotes the thermocouples used to measure the bridge's temperature. Dimensions in [m].



Every hour, the fiber-optic strain monitoring system captured 1200 s of dynamic strain data under ambient excitation from all FBGs installed on the bridge at a sampling rate of 1000 Hz. Each set of ambient strain data was used for automated Operational Modal Analyses (OMA), to identify the modal characteristics of the bridge, i.e., natural frequencies and strain modes shapes, which represent the state of the bridge at the corresponding time. In total, more than 7000 operational excitation tests were conducted.

The monitoring of the Nieuwebrugstraat bridge with a dense grid of FBG sensors was another state-of-the-art experiment that is performed within the framework of the Vlaio COOCK project “Monitoring of structures and systems with fiber optic sensors”. The novelty of the experiment lays to the fact that this was the first time that the detailed strain mode shapes of a full-scale civil structure will be used to detect and localize minor local damage, which was induced in the bridge in the form of chainsaw cuts (Figure 103) that approximately simulate fatigue cracks. Detecting damage in an early stage when it is not yet posing hazard for the integrity of the structure is of major importance for both safety and economic reasons.



*Figure 103. Chainsaw cut at the middle of the monitored span of the Nieuwebrugstraat bridge. The optical fiber that monitors this part of the bridge can be seen, attached to two clamping blocks. An FBG sensor exists in between the two clamping blocks.*

The influence of temperature on the identified strain mode shapes is investigated first and, similarly to the KW51 bridge [25, 33], it is found that these are insensitive to temperature changes. Then, the influence of the induced damage (Figure 103) on the strain mode shapes is investigated. Clear local amplitude changes at the locations of the cuts can be observed (Figure 104), underlying the ability of strain mode shapes to detect and localize this type of small-scale damage [46]. Modal characteristics that are more influenced from light damage than they are from temperature are of great practical use for vibration-based monitoring of structures.

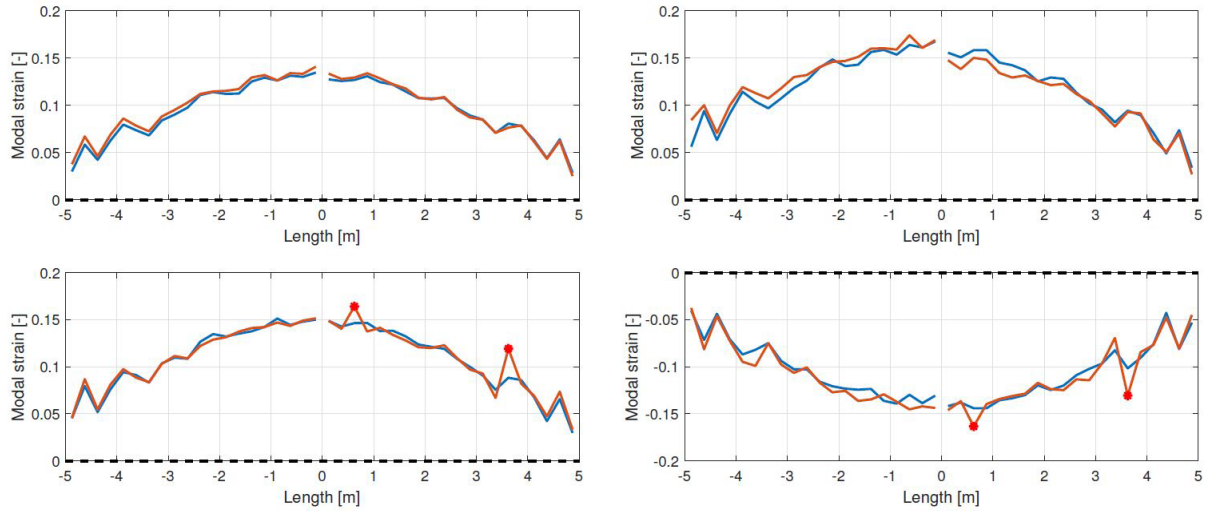


Figure 104. Strain mode shapes of mode 1 - first vertical bending mode (left) and mode 2 - first torsion mode (right) as obtained for an OMA before (blue) and an OMA after (orange) the introduction of the cuts on the south girder. The locations of the cuts, where modal strain amplitude changes are observed, are denoted with red stars. The top and bottom subplots contain the strain mode shapes at the north and south girder of the bridge, respectively.

#### 5.3.4 Vierendeel railway bridge Mechelen (TUC Rail, Infrabel and KU Leuven)

The Vierendeel bridge over the Leuvensesteenweg is a 93 m long railway bridge (Figure 105) close to the railway station of the city of Mechelen, Belgium. The bridge is part of the 47 km railway Line 25 that runs from Brussels to Antwerp and is used exclusively by passenger trainsets. The bridge is a steel single-span Vierendeel arch structure with a two-track deck, which is suspended from the arch with sixteen columns. The deck has a width of 10.6 m and consists of two main girders, stiffened with transverse beams. The bridge is supported on four steel supports at its ends, which directly sit on two concrete abutments. Under static loading, the steel supports on one end behave as hinges while on the other end as rollers.



Figure 105. The Vierendeel bridge over the Leuvensesteenweg, as seen from its west side (left) and one of the north columns (right).

The monitoring of the dynamic strains of the Vierendeel bridge was initiated on 1 September 2022. Dynamic long-gauge strains or macrostrains of the bridge are monitored with sixteen chains of FBG sensors (one chain per column), inscribed in optical fibers with polyamide coating for high strength and protection. The fibers are located at the bottom tapered zone of the columns (Figures 105 and 106), and each fiber contains 4 FBG sensors. The fibers are attached to the columns via a custom clamping system [25], to measure axial dynamic strains (Figure 107). The FBG sensors measure the average strain or macrostrain between two clamping blocks over a distance (gauge length) of about 0.85 m (Figure 106). An example of the FBG sensors installation is given in Figure 107.

The temperature of the bridge is also measured with four temperature sensors (thermocouples), attached on columns N3, N6, S3 and S6. Furthermore, two accelerometers are attached on columns S2 and S4, to measure the vertical acceleration of the bridge at these locations. The complete setup is illustrated in Figure 108.

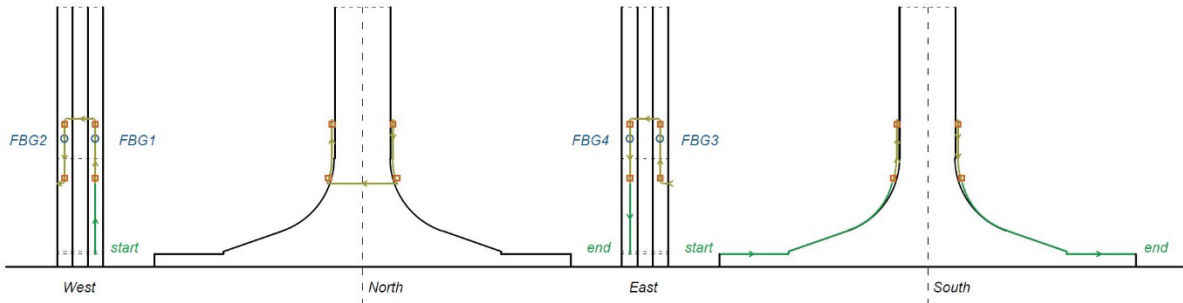


Figure 106. Schematic representation of the attachment of an FBG fiber on a typical column of the Viereindeel bridge. All four sides of the column are shown. The arrows indicate the route from the start to the end of the fiber. The fiber is represented with green (lead-in/start and lead-out/end parts) and yellow (fiber part with inscribed FBGs). The orange cubes represent the clamping blocks and the blue circles the FBG sensors. The vertical distance between two clamping blocks is 85 cm and an FBG sensor exists in between to measure the average (long-gauge) strain.



Figure 107. Installation of the optic fibers: (left) clamping blocks for connecting a glass fiber to a column of the bridge; (right) thermal insulation covering fiber and clamping blocks.

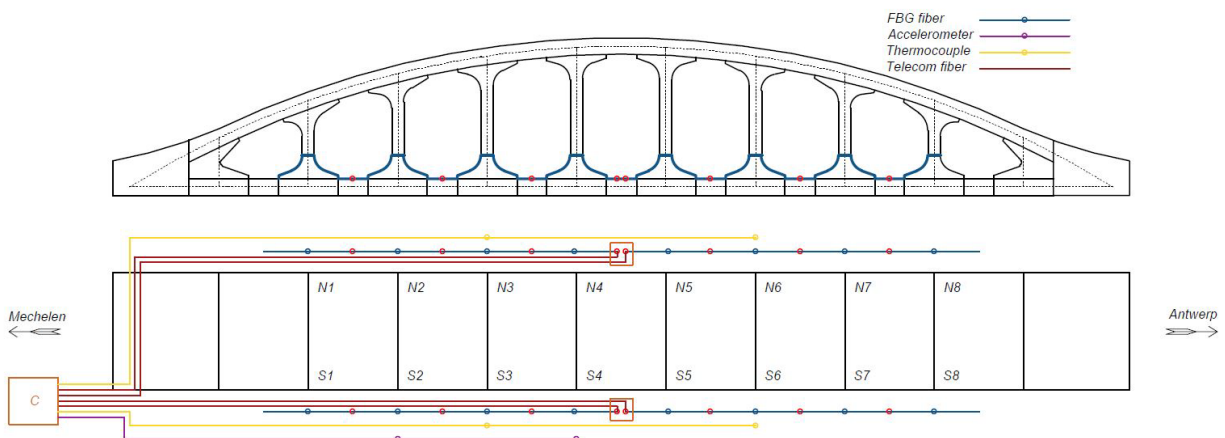


Figure 108. Monitoring system of the Viereindeel bridge. Top: side view; bottom: top view of the bridge deck. Blue lines and circles: FBG fibers and FBG sensors, respectively (each circle corresponds to the four sensors attached to each column); Yellow lines and circles: temperature cables and sensors, respectively; magenta lines and circles: coax-cables and accelerometers, respectively; red lines and circles: telecom fibers and connectors between the fibers, respectively. C denotes the cabinet where the acquisition systems and the PC that is required to operate them are placed, next to the bridge.

---

Every hour, the fiber-optic strain monitoring system captures 1200 s of dynamic strain data under ambient and operational excitation from all FBGs installed on the bridge at a sampling rate of 1000 Hz. Each set of ambient strain data is used for automated Operational Modal Analyses (OMA), to identify the modal characteristics of the bridge, i.e., natural frequencies and strain modes shapes, which represent the state of the bridge at the corresponding time. During each test, the accelerations on columns S2 and S4 (Figure 108) are also measured at a sampling rate of 1000 Hz, as well as the temperature of columns N3, N6, S3 and S6 at a sampling rate of 1 Hz.

The monitoring of the Vierendeel bridge with a dense grid of FBG sensors is performed under the request of TUC Rail and aims to monitor these locations of the columns where high stress concentration occurs during train passages and hence, are prone to fatigue damage. The novelty of the experiment lays to the fact that this is the first time that modal strain-based monitoring is employed on a civil structure under the request of a stakeholder and not for purely research purposes. It is a proof of the growing interest for this monitoring method that has demonstrated its potential through the monitoring of the KW51 bridge [25], the Canada footbridge [43] and the Ronse bridge [46].

Next to the monitoring of the fatigue prone areas, the influence of temperature on the identified strain mode shapes and natural frequencies is also investigated. Temperature can influence modal characteristics and this influence can be higher than the influence of damage. Hence, to accurately detect damage and avoid false alarms, the temperature influence needs to be known. In the present case, the strain mode shapes have been found insensitive to temperature changes between 0°C and 35°C, while natural frequencies pose a negative correlation with temperature, i.e., the higher the temperature, the lower the natural frequency. This means that any changes to strain mode shapes can be directly attributed to damage, while changes in natural frequencies might be also related to temperature and thus, data normalization is required first, to remove the influence of temperature.

### 5.3.5 Ground anchor monitoring, Streefkerk, NL (Rijkswaterstaat and Franki Foundations)

In the framework of dike reinforcement works in the Netherlands (KIS project), ground anchors were installed to reinforce the new quay wall of the yacht harbour of Streefkerk. The anchors are installed below the existing dike (see Figure 109). As part of the dike reinforcement works, the existing dike was raised. Important settlements were expected in the upper soft clay layers (16m of clay followed by a 27m thick Pleistocene sand layer), resulting in additional loads on the anchors. A research project was set up by Rijkswaterstaat to study the effect of the dike reinforcement works on the anchor behaviour.

2 anchors with a length of about 35 m were instrumented with Fiber Bragg Grating (FBG) arrays and 2 additional anchor load cells. The FBG arrays were glued onto a steel tendon of the anchors during anchor manufacturing (see Figure 110). The anchors were installed by Franki Foundations.

After installation, the FBG sensors were measured continuously during the suitability tests. The strain measurements on the steel tendons show clearly the constant strain over the anchor free length at the different load steps and the effect of the bonded length (see Figure 111). Subsequently, the anchors were monitored periodically during more than 2 years, about every 2 months or after specific milestones in the project, e.g., after every phase in the realisation of the embankment. In Figure 112, the load cell measurements are compared to the evolution of average strain over the free anchor length. Both measurements show the same trends (the load cells show larger seasonal fluctuations).

Thanks to the monitoring, a detailed insight in the evolution of the anchor loads was obtained. Not only due to excavation of the port, also during the realization of the embankment on top of the anchors. The monitoring allowed to verify the Plaxis numerical models and showed that further design optimization is probably possible. A high enough monitoring frequency allowed to understand the seasonal effect of water level and ambient temperature on the anchor loads. Figure 113 shows a view of the project site after the new quay wall was finished.

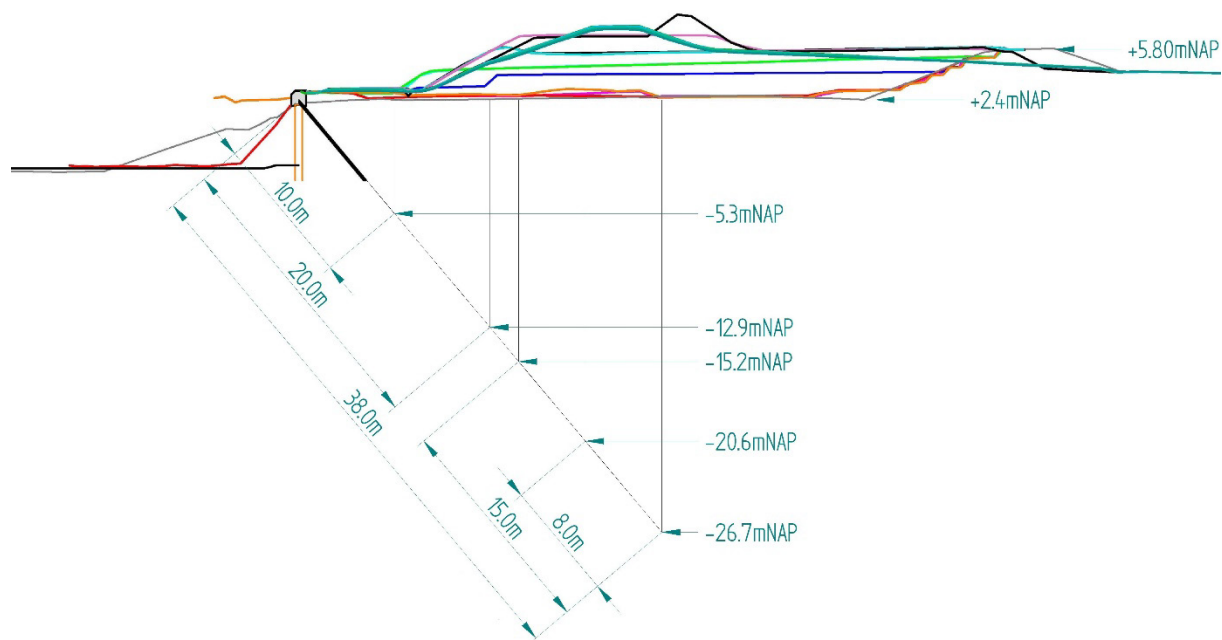


Figure 109. Cross section of the dike. The different dike profiles during the reinforcement works are indicated in different colours.

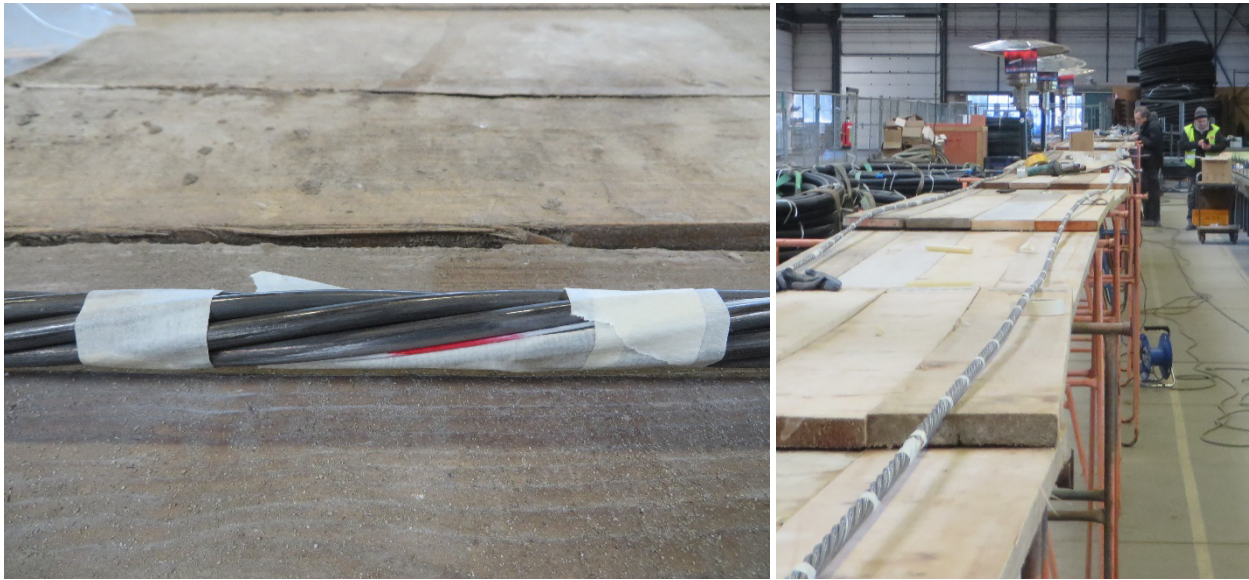


Figure 110. Instrumentation of the steel tendons with FBG sensors.

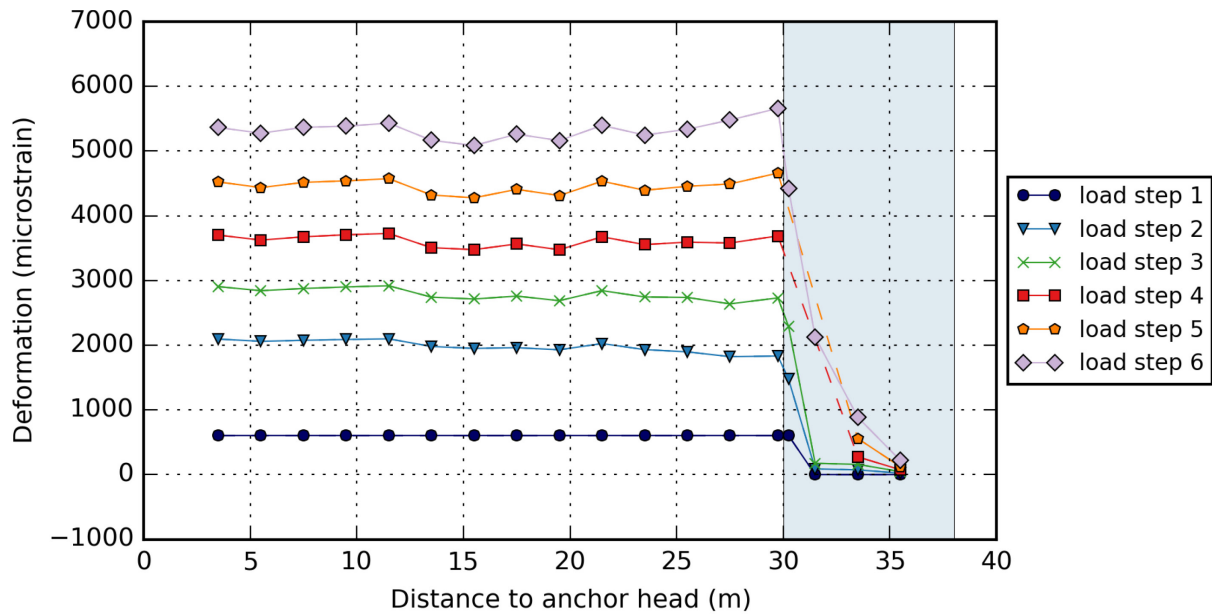


Figure 111. FBG measurements of an anchor during the suitability test. The transition between free and fixed anchor length is at about 30 m from the anchor head.

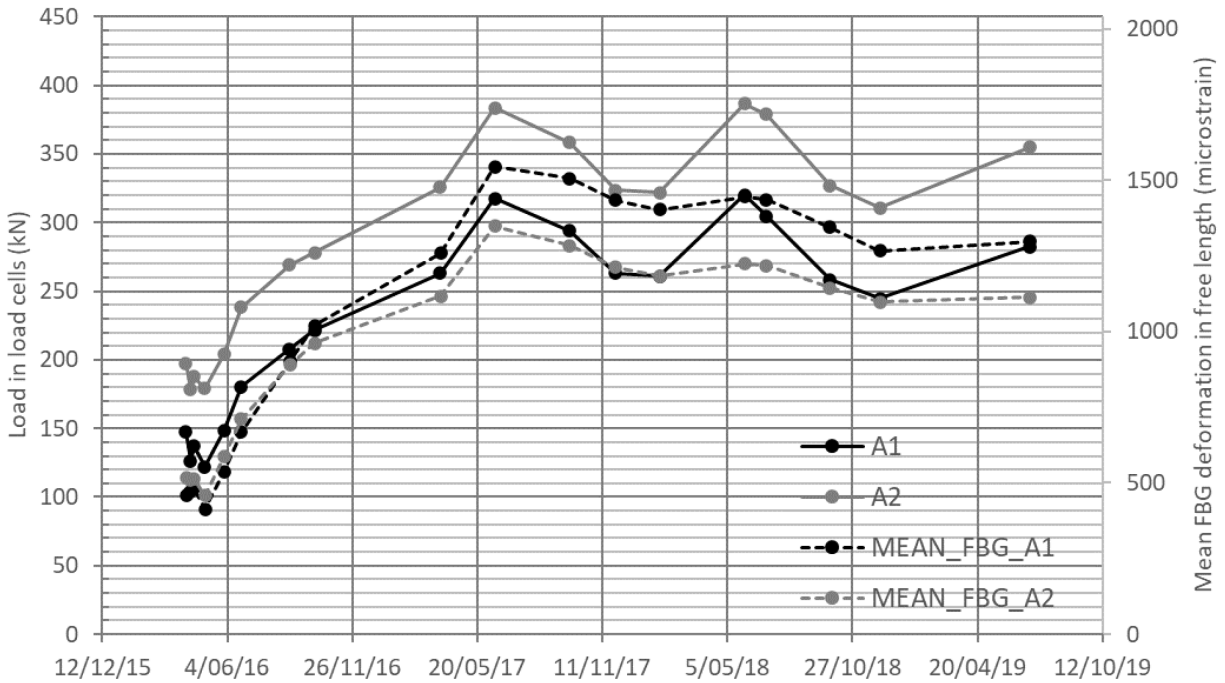


Figure 112. Evolution of the load measured by the load cells compared to the mean FBG strain measurements over the free anchor length.



Figure 113. View of the project location after finishing the dike reinforcement and the new quay wall. The black tubes extending from the anchor heads were used for water pressure measurements, which were converted into a vertical displacement profile.



### 5.3.6 Leakage detection of earth dams, levees, water reservoirs, etc. with DTS

In literature, several applications can be found of Distributed Temperature Sensing (DTS) leakage detection systems for earth dams, levees, water reservoirs, waste disposals, etc. [12, 47]. The idea is to detect leakages by anomalous temperatures.

In a passive way, the leakage causes a temperature deviation from the normal undisturbed temperature at that location/depth (illustrated in Figure 114). E.g., a DTS cable below an earth dam measures the soil temperature. A local leakage of water coming from the river will give rise to a higher/lower temperature.

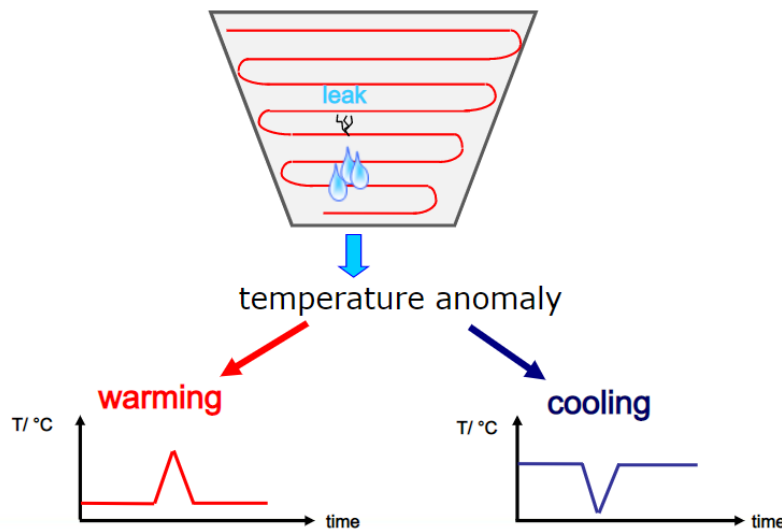


Figure 114. Passive method for leakage detection (image source: Smartec).

In an active way, heat can be injected by an external source (typically a heating wire, like the hybrid cable in Table 7, which combines optical fibers and copper wires in one single cable). Leakages will dissipate the injected energy faster and thus lead to a lower temperature rise (Figure 115).

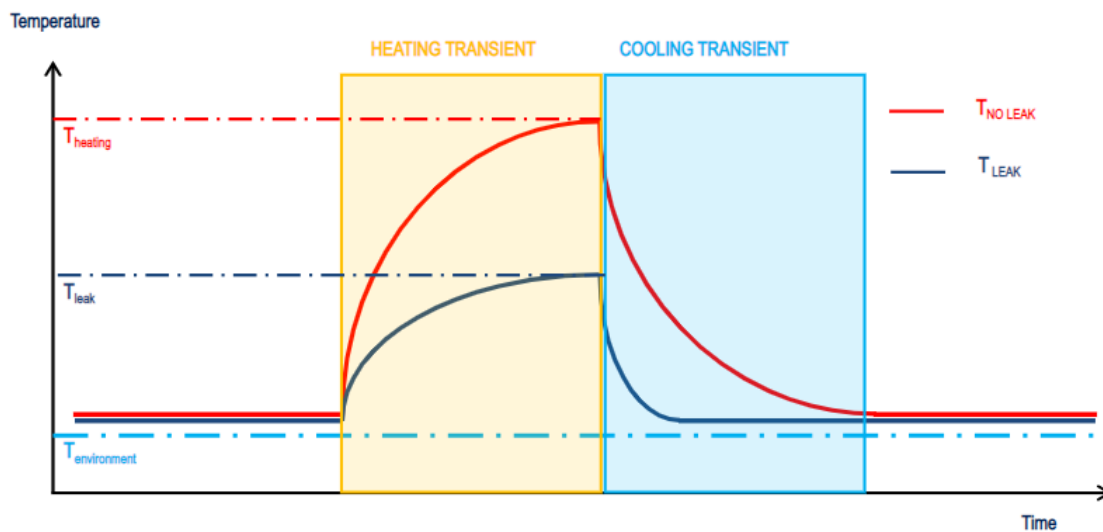


Figure 115. Active method for leakage detection by actively injecting heat (image source: Smartec).

### 5.3.7 Monitoring pipelines for leakages and intrusions with DAS (Fluves)

Pipeline leaks and intrusions produce sound, which can be detected and localized using Distributed Acoustic Sensing (DAS). Based on this principle, Fluves, in collaboration with Vigotec, developed DALI (Distributed Acoustics for Leakage and Intrusion), an all-in-one pipeline monitoring system for pipelines transporting any fluid including water, steam, gas, and chemicals. DALI makes it possible to detect and localize leaks and intrusions in pipelines permanently, enabling for prompt interventions and better asset management.

DALI works as follows (Figure 116):

1. A fiber optic cable housed in a durable microduct (which is also certified for use in drinking water), is installed in the pipeline. Fibers can also be used as a communication channel for sensors and valves.
2. Continuous measurements of all sounds over the entire fiber optic cable length in the pipeline are recorded by a DAS system, and handled by advanced signal processing and machine learning algorithms to detect events of interest such as leaks, excavators, and other intrusions.
3. Alerts are transmitted automatically via e-mail, SMS, or SCADA and are shown on an online dashboard. The results of long-term monitoring are provided to help asset managers plan their maintenance approach.

Monitoring pipelines with DALI enables large cost savings on maintenance and inspection in addition to preventing damage from the leak, since the lifetime of (ageing) pipelines can be extended by increased monitoring, while keeping the risk of leaks or other incidents low. As a result, the return on investment of a DALI system is often less than two years.

DALI has been successfully applied to monitor a six-kilometre section of a potable water pipeline that had an increased risk of leakage. The 1000 mm-diameter concrete-steel pipeline is operated by FARYS, a water utility, and has been continuously monitored with DALI since the spring of 2020. FARYS is automatically notified through e-mail whenever an incident is identified, and the location is displayed on a map on the dashboard. The results of long-term monitoring are provided in a unique way that supports Farys' maintenance approach.

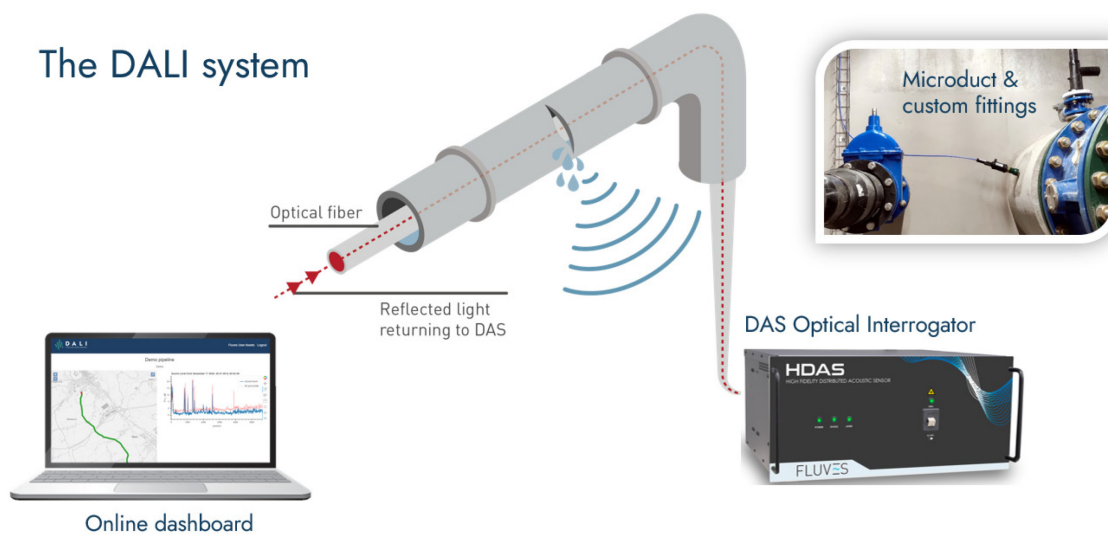


Figure 116. Schematic overview of the DALI pipeline integrity and leakage detection system (image source: Fluves).

### 5.3.8 Furnace insulation monitoring using DTS (Aperam)

Aperam, a leading stainless steel manufacturer, operates massive furnaces for the production of steel slabs. The thermal insulation on the furnace roof must remain in good condition to control production operating temperatures, limit energy costs, and avoid shutdowns. However, the roof is inaccessible to typical inspection tools like thermal cameras. In 2019, Fluves installed a heat-resistant fiber optic cable in a grid pattern that covered every square meter of the furnace roof. By connecting the cable to a Distributed Temperature Sensor (DTS), it was possible to swiftly delimit the regions where the furnace's thermal insulation needed to be replaced.

The DTS monitors the temperature during the furnace's operational heat cycles and identifies zones where the thermal insulation on these areas had failed based on abnormal temperature increases during these cycles. Raw DTS data is transformed into a user-friendly heat map of the furnace, which is then displayed through a web portal for Aperam's operational staff (Figure 117). Only a minor area of the furnace needed repair, thanks to confirmation of the monitoring system that most elements of the furnace were in good working order, resulting in a significant savings in maintenance expenses. The monitoring system allows to prioritize specific areas based on the thermal insulation's remaining lifespan. The expectations of Aperam of the monitoring solution were largely exceeded, resulting in a further expansion of the monitoring to two furnaces in 2022.

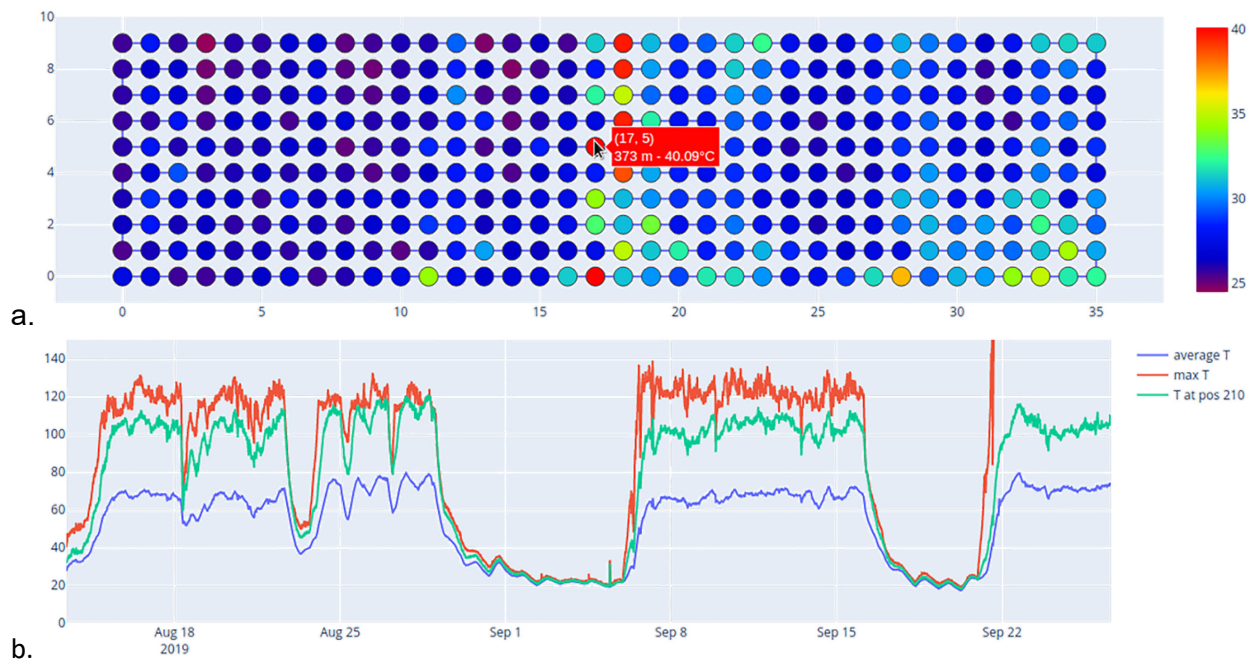


Figure 117. (a) DTS monitoring system visualized by a heat map of the furnace roof. (b) Example of the measured temperature evolution (average, maximum and at a specific position on the sensing fiber). Image source: Fluves.

### 5.3.9 Turbine vibration frequency and soil characterization on offshore wind farms using DAS (Marlinks)

The natural (N0, N1) and forced (1P, 3P, ...) vibration frequencies of offshore wind turbines offer crucial information on the health of the turbine foundation (grouting condition, scour depth, ...). These parameters are either not operationally monitored, or they are monitored with local accelerometers or vibration sensors that need to be installed and maintained on each individual turbine. An alternative and promising solution is to monitor the inter-array cables (the cables that connect each turbine with the offshore high-voltage substation (OHVS)), with Distributed Acoustic Sensing (DAS), making it possible to monitor all wind turbines in an entire wind farm with a single device, located in a secure location on the OHVS. Sensing the fiber embedded in the inter-array cables, which enter each turbine, makes it possible to determine the dominant vibration frequencies with very high accuracy (Figure 118).

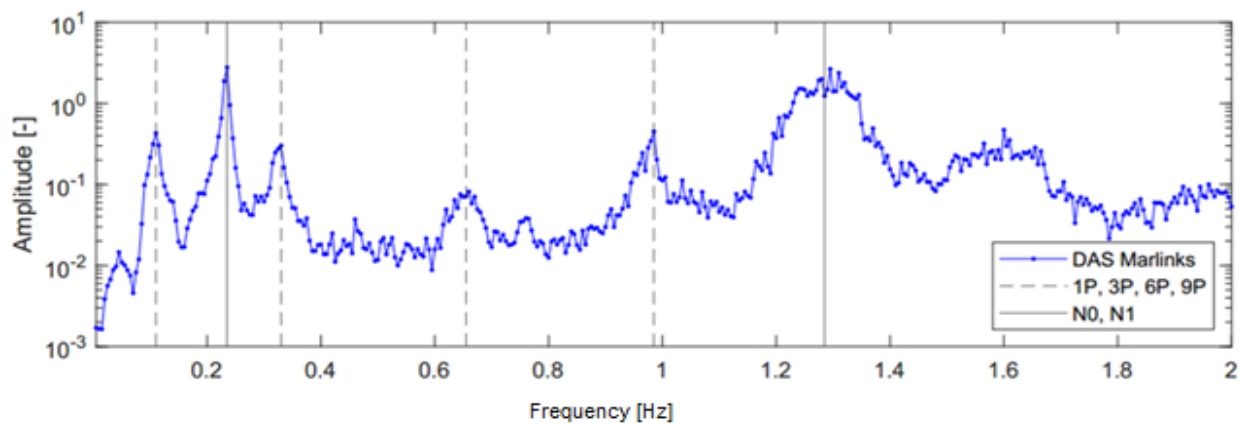


Figure 118. The frequency response of a wind turbine based on DAS measurements of a fiber optic cable inside an inter-array power cable (image source: Marlinks).

In addition, monitoring offshore cables using DAS has numerous other applications including vessel tracking, marine mammal monitoring, and even soil characterization. Using an inversion model of ambient Scholte (seismic) waves, the shear modulus of the soil under the cable has been successfully calculated based on DAS measurements as illustrated in Figure 119 [48].

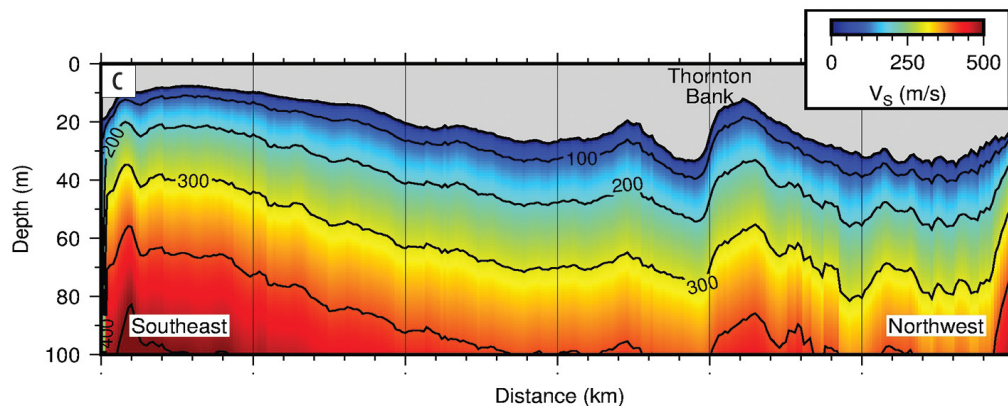


Figure 119. Soil shear velocity calculation based on DAS measurements. Image source: Williams, et al. (2021).

### 5.3.10 Monitoring the burial depth of submarine power cables with DTS (Marlinks)

Vulnerable power cables are a huge problem for the offshore wind industry. The transport of energy to the mainland needs to be solid but sometimes, these cables are damaged by external factors. The most effective way of protecting these cables is to bury them on the perfect range in the seabed. However, the sea bottom is a dynamic, rather than a static landscape. Therefore, it is crucial for a cable owner to continuously monitor the depth of burial (DoB) of the power cable.

As the current monitoring techniques are expensive and require the mobilization of survey vessels, Marlinks has developed a technique to continuously calculate the burial depth based on the temperature of the cable, which is measured with Distributed Temperature Sensing (DTS). The actual advantage is that this method allows a continuous monitoring (an update every two weeks), whereas classic survey methodologies only provide one 'snapshot' of the DoB. By using the thermal and geotechnical characteristics of the surroundings of the cable, combined with the measured DTS temperature, the method developed by Marlinks derives the DoB of the cable (Figure 120). The Marlinks model can reduce the costs as well as the risks involved as the assessment is based on the continuous DoB calculations.

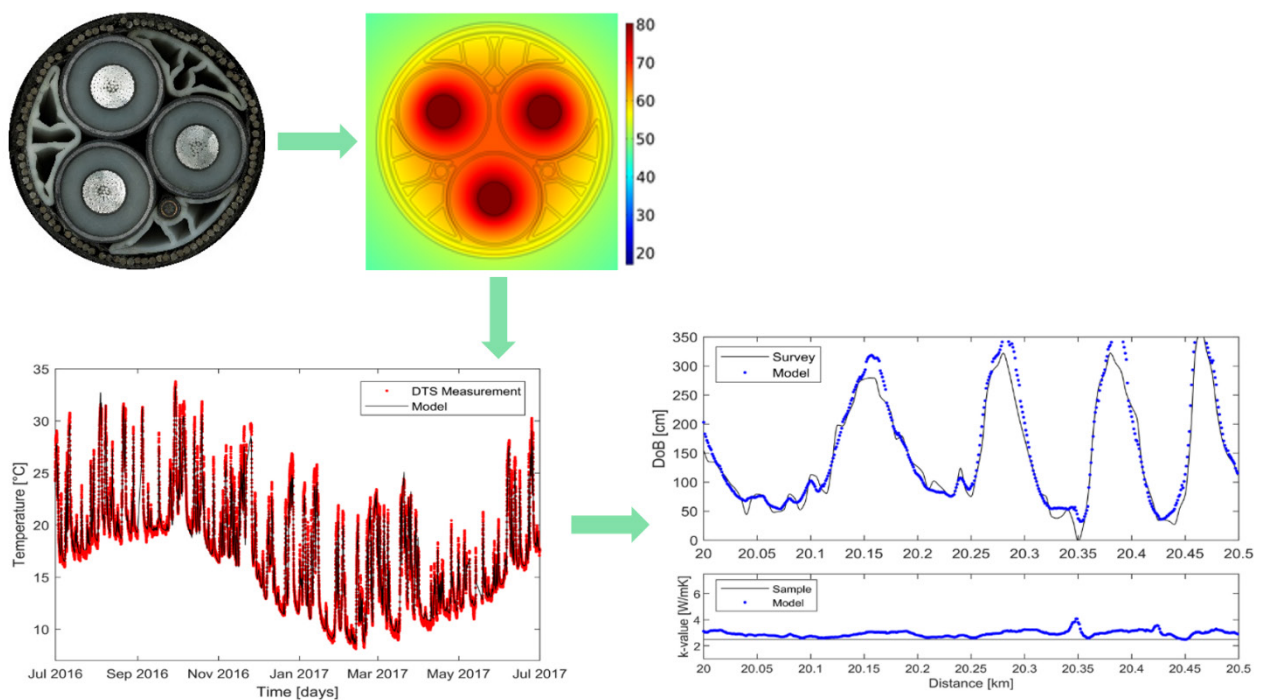


Figure 120 Depth of Burial (DoB) calculation of an offshore power cable based on DTS measurements compared to offshore survey results (image source: Marlinks).

### 5.3.11 DTS fire detection system in the Tangent tunnel, Mechelen (Flanders Road and Traffic Agency)

At the Tangent tunnel in Mechelen (Belgium), a distributed Linear Heat Detection system has been deployed. Two Distributed Temperature Sensing (DTS) systems have been set up, at the ends of the 1200 m long tunnel. A temperature sensing fiber optic cable has been installed above each lane. The monitoring data is automatically sent to the central tunnel management system of the Flanders Road and Traffic Agency.



Figure 121. (a) Above each lane, a temperature sensing cable is mounted on the tunnel ceiling. (b) One of the two installed DTS units, installed in a network cabinet.

## 5.4 Quality Control

### 5.4.1 Post-injections of grout anchors and foundation piles (Smet-F&C)

Foundation contractor Smet-F&C is continuously improving their execution techniques. To assess the performance of post grout injections of foundation piles and ground anchors, distributed strain sensing cables were integrated in the elements during execution (illustrated in Figures 122 and 123).



Figure 122. (a-c) Instrumentation of the reinforcement cage of a CFA foundation pile, before, during and after execution.



Figure 123. (a) Attaching the distributed strain sensing cables to the bottom of the steel tendons of a ground anchor. (b) During installation of the ground anchor in the borehole. Simultaneously, the fiber optic cables are integrated.

After installation, the fiber optic cables were connected to a BOFDA DAQ unit. The measurements show the effect of the post injections and allow to improve this process. The same strain sensing cables were later used to measure the deformations in the piles/anchors during a static load test.



#### 5.4.2 Temperature monitoring of diaphragm walls, Merksem (Lantis)

In order to improve the mobility situation in and around Antwerp, Lantis conceived the plan to close the ring road by building the Oosterweel link. To assess the technical feasibility of the plans, Lantis carried out several large-scale test campaigns (see also the case in Section 5.2.3 “Oosterweel test pit, Antwerp (Lantis)”). Based on the information thus required, it was possible to design and execute the Oosterweel link in a more efficient and more economical way.

One of the test campaigns involved the testing of the bearing capacity of 4 diaphragm wall panels in the Boom clay (about 39 m deep). These tests were conducted with Osterberg cells (“O cells”, lost hydraulic jacks) that were integrated in the reinforcement cage. The reinforcement cage (consisting of 3 separate parts) was fully equipped with optical fiber strain and temperature sensors (FBG, BOFDA and Raman). Figure 124a shows the sensor cables during the installation of the reinforcement cages in the excavated panel. Immediately after the installation of the reinforcement cages, connectors were spliced on the optical fiber cables to connect them to the DAQ unit.



Figure 124. (a) Sensor cables during the lowering of the reinforcement cage in the excavated panel. (b) Splicing of the sensor cables prior to concreting the diaphragm wall panel.

In Figure 125a, the temperature evolution in the diaphragm wall during concreting is shown. Due to the temperature difference between bentonite and concrete, the BOFDA temperature measurements allow to follow the concrete level and reconstruct the concreting process.

The temperature evolution in the diaphragm wall panel after concreting is shown in Figure 125b. When the soil layering and its thermal properties is taken into account, anomalies like cavities or concrete covering can be determined based on these temperature measurements (see also [22, 49] for similar applications).

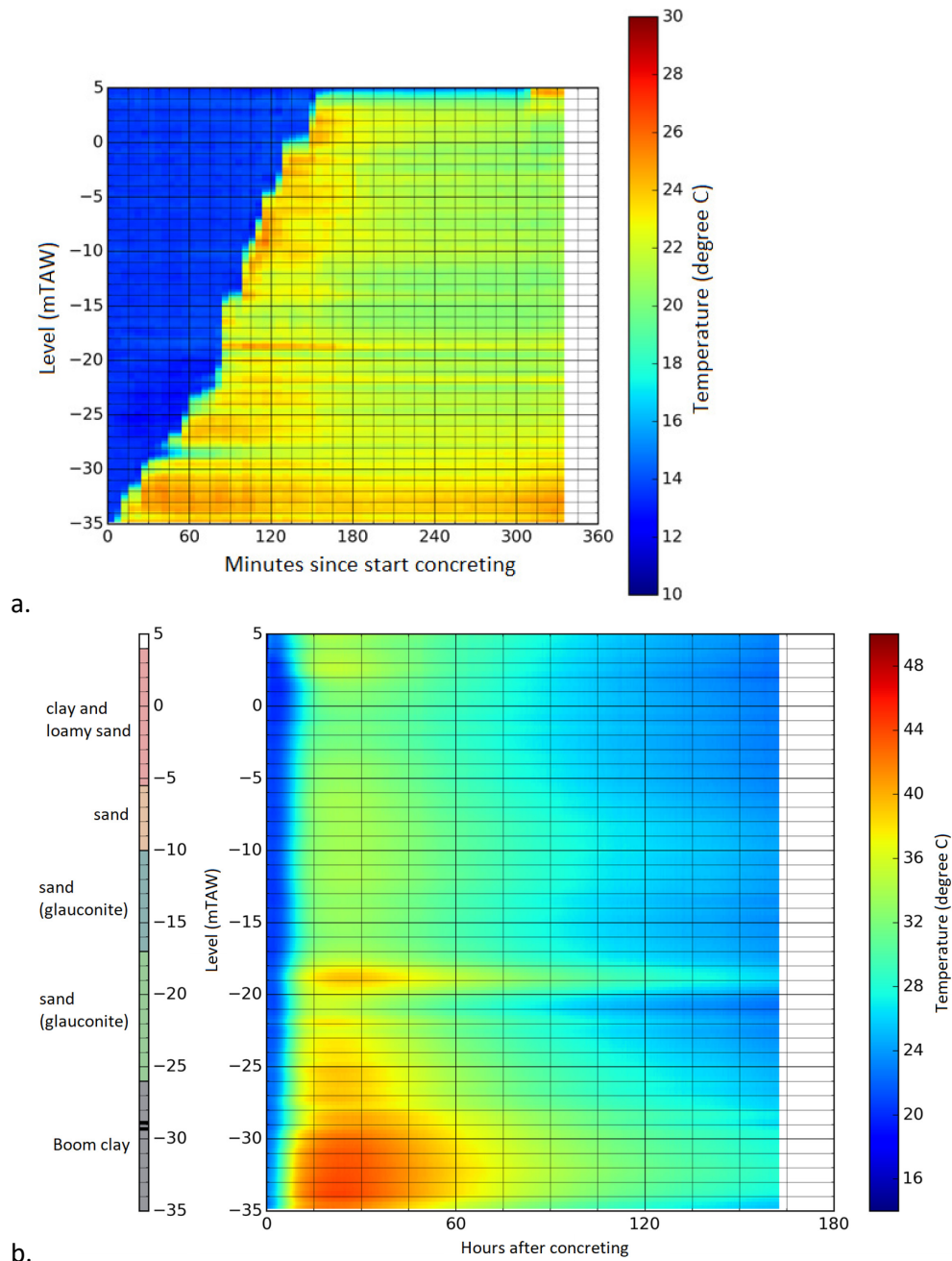


Figure 125. (a) Temperature evolution during diaphragm wall concreting (BOFDA measurement). (b) Temperature evolution after concreting.

### 5.4.3 Advanced thermal response tests (shallow geothermal energy)

In the field of shallow geothermal energy systems for heating and cooling of buildings, more specifically borehole heat exchangers (BHE), the thermal conductivity and thermal borehole resistance are important parameters for an optimal design of the BHE field.

Traditionally, these parameters are determined by performing a thermal response test (TRT) on a borehole heat exchanger. A device is connected to the BHE and injects during several days a constant power (a constant temperature difference between inlet and outlet is maintained at a constant flow rate). Inlet and outlet temperature are monitored during the test, resulting in an average value of the thermal conductivity of the soil and of the thermal borehole resistance for the BHE.

With Distributed Temperature Sensing (DTS) technology, the temperature can be monitored over the entire depth of the borehole (e.g., a temperature value every 0.5 m). This allows the determination of a detailed depth profile of the thermal conductivity and borehole resistance. Such advanced thermal response tests can be performed in different ways, e.g., distributed TRT (DTRT) and enhanced ETRT [50]. For a DTRT a traditional TRT device is used in combination with a DTS cable inside the heat exchangers. ETRTs make use of a hybrid cable, which combines temperature sensing fibers and copper heating wires.

Based on the thermal conductivity profile, the depth of the boreholes can be optimised. Peaks of the thermal conductivity may indicate important, local groundwater flow (see e.g. in Figure 126). The thermal borehole resistance parameter is not only an important parameter in the BHE field design as it is a measure of the thermal resistance between the heat carrier fluid in the pipes and the borehole wall, the depth profile may also indicate anomalies in the borehole diameter or borehole grouting (see e.g. in the upper metres of Figure 127).

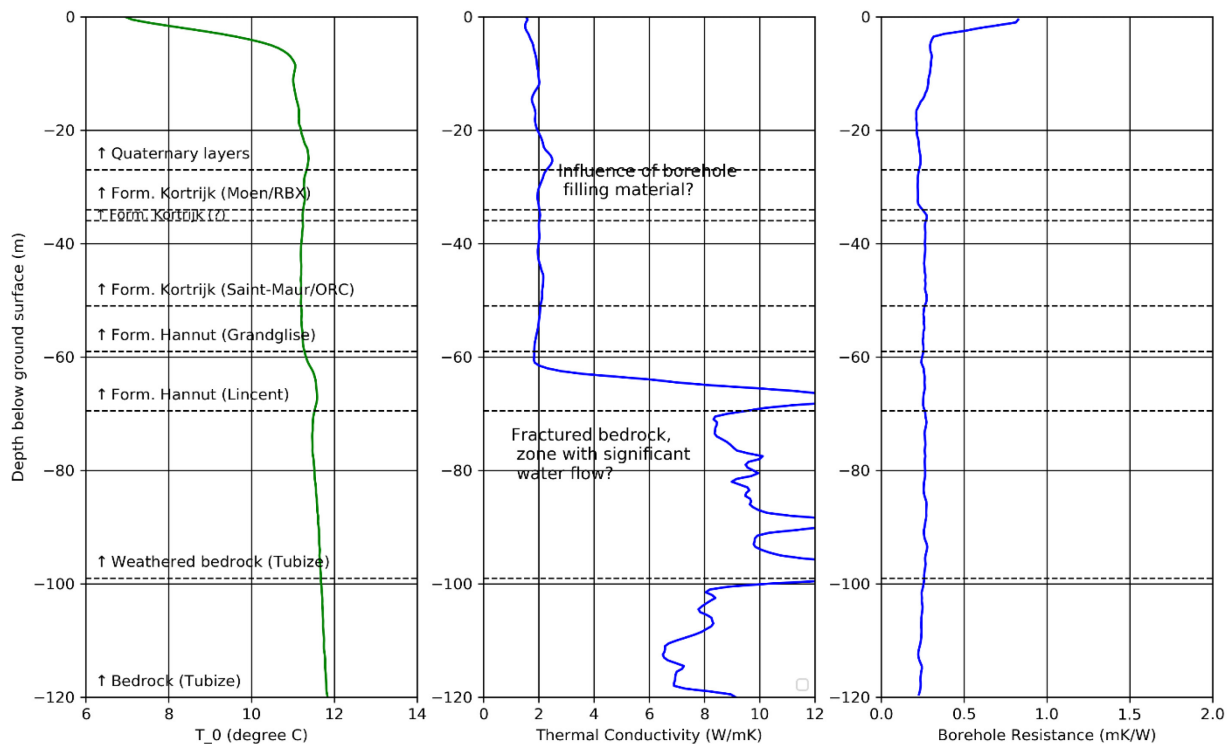


Figure 126. Undisturbed temperature profile ( $T_0$ ), thermal conductivity profile and borehole resistance based on the results of an ETRT performed by Buildwise.

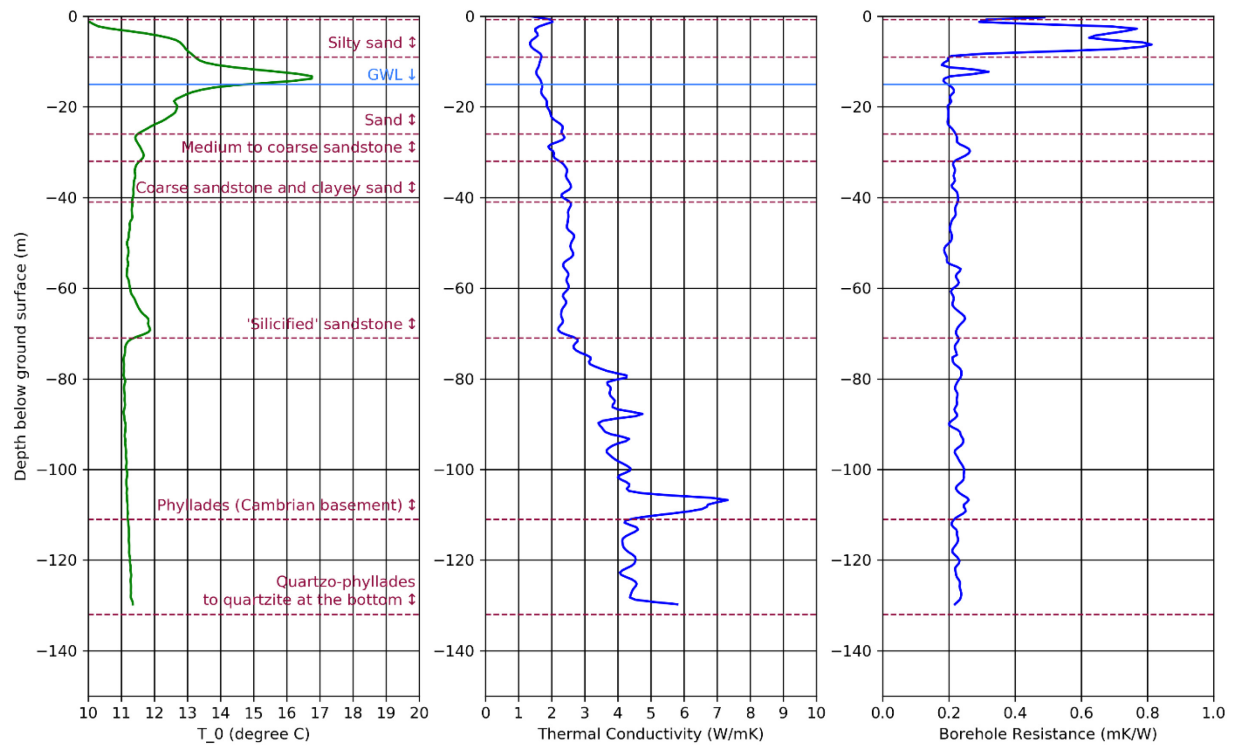


Figure 127. Undisturbed temperature profile ( $T_0$ ), thermal conductivity profile and borehole resistance based on the results of an ETRT performed by Buildwise.

---

## 6 References

- [1] A. Barrias, J. R. Casas, and S. Villalba, "A Review of Distributed Optical Fiber Sensors for Civil Engineering Applications," *Sensors*, vol. 16, 2016, p. 748, <https://doi.org/10.3390/s16050748>
- [2] M. F. Bado and J. R. Casas, "A Review of Recent Distributed Optical Fiber Sensors Applications for Civil Engineering Structural Health Monitoring," *Sensors*, vol. 21, 2021, p. 1818, <https://doi.org/10.3390/s21051818>
- [3] E. Udd and W. B. Spillman, *Fiber Optic Sensors: An Introduction for Engineers and Scientists: Second Edition*, 2011.
- [4] InformationGatekeepers. (2019, 06/12/2021). *Distributed and Single Point Fiber Optic Sensing Systems Forecast*. Available: [http://www.igigroup.com/st/pages/photonic\\_sensor\\_report.html](http://www.igigroup.com/st/pages/photonic_sensor_report.html)
- [5] M. C. Fenta, D. K. Potter, and J. Szanyi, "Fibre Optic Methods of Prospecting: A Comprehensive and Modern Branch of Geophysics," *Surveys in Geophysics*, vol. 42, 2021/05/01 2021, pp. 551-584, <https://doi.org/10.1007/s10712-021-09634-8>
- [6] C. M. Monsberger and W. Lienhart, "Distributed Fiber Optic Shape Sensing of Concrete Structures," *Sensors*, vol. 21, 2021, p. 6098, <https://doi.org/10.3390/s21186098>
- [7] W. R. Habel, I. Baumann, F. Berghmans, K. Borzycki, C. Chojetzki, K.-H. Haase, *et al.*, "Guideline for Use of Fibre Optic Sensors," COST Action 299 "FIDES" Optical Fibres for New Challenges Facing the Information Society, January 2009, 2009.
- [8] S. Ibrahim, J. O'Dowd, V. Bessler, D. Karabacak, and J. Singer, "Optimization of fiber Bragg grating parameters for sensing applications," presented at the SPIE Commercial + Scientific Sensing and Imaging, 2017.
- [9] fibrisTerre Systems GmbH, "Distributed fiber-optic Brillouin sensing," Technical Documentation, August 2015, 2015.
- [10] M. Minneman, E. Hoover, P. Boschert, J. Ensher, M. Crawford, D. Derrickson, *et al.*, "Very high sensor-density multiplexing using a wavelength-to-time domain reflectometry approach based on a rapidly swept akinetic laser," presented at the International Conference on Optical Fibre Sensors (OFS24), 2015.
- [11] D. Inaudi, "State of the Art in Fiber Optic Sensing Technology and EU Structural Health Monitoring Projects," presented at the Structural Health Monitoring and Intelligent Infrastructures, Tokyo, Japan, 2003.
- [12] L. Schenato, "A Review of Distributed Fibre Optic Sensors for Geo-Hydrological Applications," *Applied Sciences*, vol. 7, 2017, <https://doi.org/10.3390/app7090896>
- [13] K. Soga and L. Luo, "Distributed fiber optics sensors for civil engineering infrastructure sensing," *Journal of Structural Integrity and Maintenance*, vol. 3, 2018/01/02 2018, pp. 1-21, <https://doi.org/10.1080/24705314.2018.1426138>
- [14] K. Soga, "Fiber optic sensing technology," ed. Short Course on New Technologies for Geotechnical Infrastructure Sensing and Monitoring, Berkeley, 22-23 January 2021, 2021.
- [15] Z. Wang, B. Lu, Q. Ye, and H. Cai, "Recent Progress in Distributed Fiber Acoustic Sensing with  $\Phi$ -OTDR," *Sensors*, vol. 20, 2020, p. 6594, <https://doi.org/10.3390/s20226594>
- [16] J. Tejedor, J. Macias-Guarasa, H. F. Martins, J. Pastor-Graells, P. Corredera, and S. Martin-Lopez, "Machine Learning Methods for Pipeline Surveillance Systems Based on Distributed Acoustic Sensing: A Review," *Applied Sciences*, vol. 7, 2017, p. 841, <https://doi.org/10.3390/app7080841>
- [17] ViaLite. (2021, 15/12/2021). *APC vs PC Connectors*. Available: <https://www.vialite.com/resources/rf-over-fiber-guides/apc-vs-pc-connectors/>
- [18] J. Laferrière, G. Lietaert, R. Taws, and S. Wolszczak, "Reference Guide to Fiber Optic Testing," 2018.

- 
- [19] A. Bassil, X. Chapeleau, D. Leduc, and O. Abraham, "Concrete Crack Monitoring Using a Novel Strain Transfer Model for Distributed Fiber Optics Sensors," *Sensors*, vol. 20, 2020, p. 2220, <https://doi.org/10.3390/s20082220>
- [20] T. Howiacki, R. Sieńko, Ł. Bednarski, and K. Zuziak, "Crack Shape Coefficient: Comparison between Different DFOS Tools Embedded for Crack Monitoring in Concrete," *Sensors*, vol. 23, 2023, p. 566, <https://doi.org/10.3390/s23020566>
- [21] M. Bottiau and N. Huybrechts, "Recent advances in pile design, construction, monitoring and testing," presented at the XVII European Conference on Soil Mechanics and Geotechnical Engineering, Reykjavik, 2019.
- [22] Y. Rui, C. Kechavarzi, F. O'Leary, C. Barker, D. Nicholson, and K. Soga, "Integrity Testing of Pile Cover Using Distributed Fibre Optic Sensing," *Sensors*, vol. 17, 2017, p. 2949, <https://doi.org/10.3390/s17122949>
- [23] F. Magalhães, A. Cunha, and E. Caetano, "Vibration based structural health monitoring of an arch bridge: from automated OMA to damage detection," *Mechanical Systems and Signal Processing*, vol. 28, 2012, pp. 212-228, <https://doi.org/10.1016/j.ymssp.2011.06.011>
- [24] A. Vlamis-Stathopoulos, M. de Wit, and G. Hovhannessian, "Rion-Antirion Monitoring System," presented at the Proceedings of the 4th International Conference on Structural Health Monitoring of Intelligent Infrastructure, SHMII-4, 2009.
- [25] D. Anastasopoulos, G. De Roeck, and E. P. B. Reynders, "One-year operational modal analysis of a steel bridge from high-resolution macrostrain monitoring: influence of temperature vs. retrofitting," *Mechanical Systems and Signal Processing*, vol. 161, 2021, <https://doi.org/10.1016/j.ymssp.2021.107951>
- [26] K. Maes, L. Van Meerbeeck, E. P. B. Reynders, and G. Lombaert, "Validation of vibration-based structural health monitoring on retrofitted railway bridge KW51," *Mechanical Systems and Signal Processing*, vol. 165, 2022, p. 108380, <https://doi.org/10.1016/j.ymssp.2021.108380> ,
- [27] T. H. T. Chan, L. Yu, H. Y. Tam, Y. Q. Ni, S. Y. Liu, W. H. Chung, *et al.*, "Fiber Bragg grating sensors for structural health monitoring of Tsing Ma bridge: Background and experimental observation," *Engineering Structures*, vol. 28, 2006, pp. 648-659, <https://doi.org/10.1016/j.engstruct.2005.09.018> ,
- [28] W. Fan and P. Qiao, "Vibration-based damage identification methods: a review and comparative study," *Structural Health Monitoring*, vol. 10, 2010, pp. 83-111,
- [29] D. Anastasopoulos, "Structural health monitoring based on operational modal analysis from long-gauge dynamic strain measurements," PhD, Department of Civil Engineering, KU Leuven, Leuven, 2020.
- [30] E. Reynders, "System identification methods for (operational) modal analysis: review and comparison," *Archives of Computational Methods in Engineering*, vol. 19, 2012, pp. 51-124, <http://dx.doi.org/10.1007/s11831-012-9069-x> ,
- [31] D. Anastasopoulos, P. Moretti, T. Geernaert, B. De Pauw, U. Nawrot, G. De Roeck, *et al.*, "Identification of modal strains using sub-microstrain FBG data and a novel wavelength-shift detection algorithm," *Mechanical Systems and Signal Processing*, vol. 86A, 2017, pp. 58-74, <http://dx.doi.org/10.1016/j.ymssp.2016.09.038> ,
- [32] D. Anastasopoulos, G. De Roeck, and E. P. B. Reynders, "Influence of damage versus temperature on modal strains and neutral axis positions of beam-like structures," *Mechanical Systems and Signal Processing*, vol. 134, 2019, <https://doi.org/10.1016/j.ymssp.2019.106311>
- [33] D. Anastasopoulos, K. Maes, G. De Roeck, G. Lombaert, and E. P. B. Reynders, "Influence of frost and local stiffness variations on the strain mode shapes of a steel arch bridge," *Engineering Structures*, vol. 273, 15/12/2022 2022, <https://doi.org/10.1016/j.engstruct.2022.115097>

- 
- [34] E. Vandecruys, E. Vereecken, D. Anastasopoulos, E. Verstryngge, R. Caspeepe, E. Reynders, *et al.*, "A review and experimental study on challenges in vibration-based monitoring of corroding reinforced concrete beams.," *Structural Health Monitoring*, 2023, under review
- [35] T. De Ville, "Monitoring of grout anchors with fiber-optic strain sensors," MSc MSc Thesis, Department of Civil Engineering, KU Leuven, Leuven, 2021.
- [36] J. Smet, N. Huybrechts, G. Van Lysebetten, J. Verstraelen, and S. François, "Optical Fiber Strain Measurements and Numerical Modeling of Load Tests on Grouted Anchors," *Journal of Geotechnical and Geoenvironmental Engineering*, vol. 145, 2019, p. 04019103, [https://doi.org/10.1061/\(ASCE\)GT.1943-5606.0002167](https://doi.org/10.1061/(ASCE)GT.1943-5606.0002167)
- [37] D. Gächter, R. Kulmer, and V. Račanský, "Slope stabilization with multiple anchors monitored with glass fibre technique," presented at the DFI-EFFC International Conference on Deep Foundations and Ground Improvement: Urbanization and Infrastructure Development-Future Challenges, Rome, 2018.
- [38] C. Fabris, H. F. Schweiger, B. Pulko, H. Woschitz, and V. Račanský, "Numerical Simulation of a Ground Anchor Pullout Test Monitored with Fiber Optic Sensors," *Journal of Geotechnical and Geoenvironmental Engineering*, vol. 147, 2021, p. 04020163, [https://doi.org/doi:10.1061/\(ASCE\)GT.1943-5606.0002442](https://doi.org/doi:10.1061/(ASCE)GT.1943-5606.0002442)
- [39] B. L. Amatya, K. Soga, P. J. Bourne-Webb, T. Amis, and L. Laloui, "Thermo-mechanical behaviour of energy piles," *Géotechnique*, vol. 62, 2012, pp. 503-519, <https://doi.org/10.1680/geot.10.P.116>
- [40] L. Pelecanos, K. Soga, M. P. M. Chunge, Y. Ouyang, V. Kwan, C. Kechavarzi, *et al.*, "Distributed fibre-optic monitoring of an Osterberg-cell pile test in London," *Géotechnique Letters*, vol. 7, 2017, pp. 152-160, <https://doi.org/10.1680/jgele.16.00081>
- [41] P. J. Bourne-Webb, B. Amatya, K. Soga, T. Amis, C. Davidson, and P. Payne, "Energy pile test at Lambeth College, London: geotechnical and thermodynamic aspects of pile response to heat cycles," *Géotechnique*, vol. 59, 2009, pp. 237-248, <https://doi.org/10.1680/geot.2009.59.3.237>
- [42] Y. Ouyang, A. Bell, M. Elshafie, C. Kechavarzi, K. Soga, R. Fernie, *et al.*, "The history of UK experience in the use of fibre optic monitoring of geotechnically associated installations," in *Geotechnical Engineering for Infrastructure and Development*, ed, 2015, pp. 637-642.
- [43] D. Anastasopoulos, E. P. B. Reynders, S. François, G. De Roeck, G. Van Lysebetten, P. Van Itterbeeck, *et al.*, "Vibration-based monitoring of an FRP footbridge with embedded fiber-Bragg gratings: Influence of temperature vs. damage," *Composite Structures*, 2022, p. 115295, <https://dx.doi.org/10.1016/j.compstruct.2022.115295>
- [44] R. De Nijs, F. Kaalberg, G. Osselaer, and J. Couck, "Geotechnical monitoring of a trial pit excavation toward the Boom clay in Antwerp (Belgium)," presented at the Geotechnical Safety and Risk V, Rotterdam, 2015.
- [45] N. Huybrechts and G. Van Lysebetten, "Casestudy geotechniek: monitoring van de Oosterweelproefput (2015-04.04)," Buildwise, 2015.
- [46] D. Anastasopoulos, G. De Roeck, and E. Reynders, "Long-term dynamic strain monitoring of the Nieuwebrugstraat railway bridge: influence of damage vs. temperature," presented at the 10th European Workshop on Structural Health Monitoring, Palermo, Italy, 2022.
- [47] M. Nikles, B. Vogel, F. Briffod, S. Grosswig, F. Sauser, S. Luebbecke, *et al.*, *Leakage detection using fiber optics distributed temperature monitoring* vol. 5384: SPIE, 2004.
- [48] E. F. Williams, M. R. Fernández-Ruiz, R. Magalhaes, R. Vanthillo, Z. Zhan, M. González-Herráez, *et al.*, "Scholte wave inversion and passive source imaging with ocean-bottom DAS," *The Leading Edge*, vol. 40, 2021/08/01 2021, pp. 576-583, <https://doi.org/10.1190/tle40080576.1>
- [49] N. De Battista, C. Kechavarzi, H. Seo, K. Soga, and S. Pennington, "Distributed fibre optic sensors for measuring strain and temperature of cast-in-situ concrete test piles.," presented at the Transforming the Future of Infrastructure through Smarter Information, 2016.

- 
- [50] S. Wilke, K. Menberg, H. Steger, and P. Blum, "Advanced thermal response tests: A review," *Renewable and Sustainable Energy Reviews*, vol. 119, 2020/03/01/ 2020, p. 109575, <https://doi.org/10.1016/j.rser.2019.109575>